Force Transduction and Strain Dynamics through Actin Stress Fibres of the Cytoskeleton

Louise Guolla

Thesis submitted to the
Faculty of Graduate and Postdoctoral Studies
In partial fulfillment of the requirements
For the MSc degree in Physics

Department of Physics
Faculty of Science
University of Ottawa

A Sonnet on a Cell

The swirling fibres of a fibroblast cell
give strength and structure to its tethered girth.
The shape they take, to bend or break, do tell
a story to all those who prove their worth

The actin filaments, here glowing green
or grey, in pictures from the microscope,
are made with transfections of GFP,
and with fluoro-emission appear as rope.

Now with this tool; begin experiments
of poking with an AFM to see
if our results of fibrous move'ment
confound those models of tensegrity

No matter what, we will elucidate
exactly how the cells transduce their fate.

Table of Contents

List of Figures

Abbreviation Legend

General Abbreviations

AFM: Atomic Force Microscope
E: Young's Modulus of Elasticity
µM, µm: micro-Molar, micro-metre (10^{-6})
NA: Numerical Aperture
nN: Nano-Newton (10^{-9})
S.D.: Standard Deviation
S.E.M.: Standard Error of the Mean
SGR: Soft Glassy Rheology
UV: Ultra-violet

Biological Abbreviations

ATP/GTP: Adenosine (guanine) triphosphate
CSK: Cytoskeleton
DNA/RNA: (deoxy)-ribonucleic acid
ECM: Extracellular Matrix
EGFP: Enhanced Green Fluorescent Protein
FA(s): Focal Adhesion(s)
FLIP: Fluorescence Loss in Photobleaching
FRAP: Fluorescence Recovery after Photobleaching
GFP: Green Fluorescent Protein
LC: Light Chain (as in Myosin Light Chain)
MLCK: Myosin Light Chain Kinase
MLCPase: Myosin Light Chain Phosphatase
MT: Microtubule(s)
ROCK: Equivalent to Rho Kinase
SF: Stress fibre(s)

Chemical Abbreviations

dH_2O: distilled water
DMSO: Dimethyl Sulfoxide
DMEM: Dulbecco's Modified Eagle Medium
FBS: Fetal Bovine Serum
HEPES: 4-(2-hydroxyethyl)-1-piperazineethanesulfonic acid
LB: Luria-Bertani Medium
$MgCl_2$: Magnesium Chloride
NaCl: Sodium Chloride
PBS: Phosphate-buffered saline

Abstract

It is becoming clear that mechanical stimuli are critical in regulating cell biology; however, the short-term structural response of a cell to mechanical forces remains relatively poorly understood. We mechanically stimulated cells expressing actin-EGFP with controlled forces (0-20nN) in order to investigate the cell's structural response. Two clear force dependent responses were observed: a short-term local deformation of actin stress fibres and a long-term force-induced remodelling of stress fibres at cell edges, far from the point of contact. We were also able to quantify strain dynamics occurring along stress fibres. The cell exhibits complex heterogeneous negative and positive strain fluctuations along stress fibres, indicating localized dynamic contraction and expansion. A ~50% increase in myosin contractile activity is apparent following application of 20nN force. Directly visualizing force-propagation and stress fibre strain dynamics has revealed new information about the pathways involved in mechanotransduction which ultimately govern the downstream response of a cell.

Acknowledgements

When I first started my university career in Biochemistry, I never would have imagined myself following the path that I have. I initially began studying Physics because it interested me, but with no real intention of pursuing it in terms of research. I would have likely discovered the field of Biophysics too late were it not for the instrumental Nanobiophysics classes taught by Dr. Josee Coutu in my fourth year Macromolecules class. Dr. Coutu, who was not an expert in this field, pushed me to investigate further on my own the opportunities that biophysics offered, I would like to thank her for that.

Curious, but with no real idea what I was getting myself into, I approached my future supervisor, Dr. Andrew Pelling. I wish to thank him most profoundly for taking a chance on me, encouraging the Physics department to accept my candidacy, even without the proper prerequisites, and for providing me with the opportunity to excel in his laboratory. I would not have succeeded without the many hours of useful discussion, gentle (and not-so-gentle) reminders to get stuff done, and encouragement. Thank you. I would like to acknowledge also the financial support that I received from the National Sciences and Engineering Research Council (NSERC) and Ontario Graduate Scholarship programs; this work would not have been possible without it.

I wish to thank all members of the Pelling group, especially: Dr. Dominique Tremblay, Zeinab Al-Rekabi, Tina Haase, Joan Macadangdang, Pamela Wu, and J Wang. Tina: thank you especially for your help with the PLC-δ transfections and experiments and providing me with an excellent figure of the Sneddon model. J: thanks for being the best MCAT study partner ever; I couldn't have done it without you. To everyone else, and of course, the undergrads too, thanks for providing a fun work environment that I looked forward to seeing every day.

There are many other members of the CIN Labs and the physics department to which I owe my thanks. To Martin Bertrand, thank you especially for the help you provided in writing the script to analyze my strain data. You literally saved me months of work. To members of the Godin lab, especially Eric Beamish, and Jason Riordon, thank you for the company on the necessary coffee breaks, good times in the lunch room, and late nights at the lab. To all physics grad students and professors, past and present: thanks for the useful

discussions at departmental coffee, seminars, and in passing in the hall. The Physics Department at this university provided a highly stimulating environment that helped me to succeed; thank you.

Last, but certainly not least, thank you to my close friends and family who have helped me through probably one of the most difficult years of my life. To my Mom, thanks for sending me home with food when I needed it, giving me a hug whenever you saw me, and helping to keep my head on straight. To my Dad, thanks for being the practical mind behind everything I do, for always encouraging me, and believing in me, whatever I did. To Dan and Nick, you guys just rock, period. Thanks for making me laugh when I needed it. To Krista and Bobo- you've been the best long distance friends I've ever had; and, oddly enough, chatting with you has kept me more focussed on success than any other distraction ever could have. And, to all my friends from Ultimate and ORYC- thanks especially for helping to get myself away from work some days.

At times our own light goes out and is
rekindled by a spark from another person.
Each of us has cause to think with deep
gratitude of those who have lighted the flame
within us.

Albert Schweitzer (1875 - 1965), Nobel Laureate

Thank you to everyone mentioned above, and also to those who are not, who have helped to light my flame.

Contribution Statement

Conception:

The experimental ideas, methodologies and conception of the research plan were developed with my supervisor, Dr. Andrew Pelling.

Experiments and Analysis:

I performed all experiments and data analysis. The python script used to analyze all strain data in Chapter 5 was developed by Martin Bertrand, with my input. The transfections and experiments with PH-PLCδ-EGFP were performed in collaboration with Kristina Haase. Data interpretation and conclusions were developed through discussions with Dr. Pelling.

Thesis:

This thesis is my own work; I thank Dr. Pelling for his editorial assistance.

List of Publications and Presentations

Publications:

The work published in this thesis is currently accepted pending minor revision under the following title:

Guolla, L., Bertrand, M., Haase, K. & Pelling, A.E. *Force Transduction and Strain Dynamics in Actin Stress Fibres in Response to Local Nanonewton Forces*. Journal of Cell Science. (2011).

Silberberg, Y.R., Guolla, L. & Pelling, A.E. "Investigating Mammalian Cell Nanomechanics with Simultaneous Optical and Atomic Force Microscopy." Dufrene, Y.F. ed. *Life at the Nanoscale: Atomic Force Microscopy of Live Cells*. Singapore: Pan Stanford Publishing, pp.375-401 (2011).

Presentations:

Guolla, L. *Force Transduction and Strain Dynamics through Stress Fibres of the Actin Cytoskeleton*. Quantitative Biomedicine CREATE Lunchtime Talks, July 28, 2011. University of Ottawa, Ottawa, ON.

Guolla, L. *La transmission de la force et la propagation de déformation parmi les filaments d'actine en réponse aux forces locales.* Biophysics Colloquium (ACFAS Conference) May 9, 2011. Sherbrooke, QU.

Guolla, L. *Force Transmission and Strain Propagation through F-Actin Filaments in Response to Local Nanonewton Forces*. OCIP Symposium April 29, 2011. Ottawa, ON.

Chapter One:

Introduction

1.1 Structural Biology of the Cell

The cell, as the basic unit of life, was first coined as a term by Robert Hooke in the book *Micrographia,* published in 1665. Far from the simple "water balloon-esque" image pictured in many high school text books, and which is modelled in many mechanical representations of the cell (see Chapter 2.4), the cell is a highly complex structure containing numerous membrane bound organelles, each with their specific function, a nucleus (in eukaryotes) acting as a type of cellular brain, a multitude of proteins and enzymes floating and being transported throughout the cytoplasm, and even a type of polymeric skeleton known as the cytoskeleton. To understand the implications of a large part of the cellular mechanics presented in this thesis, a brief overview of the key components of cellular structure must first be presented. All of the information which follows in this section has been well characterized; the reader is referred to *Molecular Biology of the Cell* (Alberts 2002) or any other textbook on cell and molecular biology for further details unless otherwise indicated.

1.1.1 Cellular Components

The cell can take on many shapes and sizes, depending on its exact function, though there are a number of highly conserved structures which exist in all cases. Firstly, the cell is surrounded by a phospholipid bilayer membrane which separates the cellular cytoplasm (which is mainly water containing numerous cations, proteins, macromolecules and organelles) from the external environment. This membrane is generally described by a 'fluid mosaic' model; there are numerous intermembrane proteins, receptors, channels, and other molecules which are found bound within the membrane, but which are free to move around the surface of the cell. It is considered selectively permeable; this means that small ions and water molecules may passively diffuse through the membrane, but large molecules must be actively transported through specified channels in the membrane.

There are numerous membrane-bound organelles within the cell, most of which are described in Figure 1.1A. Two of the most important structures of the cell however, are the

mitochondria and the nucleus. The nucleus is a membrane-bound area of the cell in which is contained all of the genetic material of the cell in the form of chromosomes made of DNA. In this area of the cell, the DNA is copied (in preparation for cell division, or mitosis), and transcribed into messenger RNA (mRNA) which goes on to be translated (turned into proteins); this process is known as the Central Dogma of the cell. The nucleus is considered the most rigid section of the cell as it is protected by a dense meshwork of protein (nuclear lamina, addressed in section 1.1.2), and the DNA itself is quite dense. Mitochondria are the energy-producers of the cell. In these organelles, cellular respiration occurs. This is a process which uses glucose and oxygen to fuel the production of ATP (adenosine triphosphate). ATP is the main energy currency of the cell; hydrolysis of the high energy bond between oxygen and phosphate (changes ATP to ADP) provides the energy for nearly every cellular process. Oftentimes, GTP (guanine triphosphate) is used in a similar manner. Surrounding all of these organelles, providing structure and support to the cell, is a dense meshwork of polymeric proteins which are known as the cytoskeleton.

1.1.2 The Cytoskeleton

Similar to the human skeleton, the cytoskeleton provides structure and support to its body. The cytoskeleton however is highly dynamic, rather than being rigid and relatively static as is our own skeleton. It is constantly rearranging and rebuilding itself in response to signals from within the cell and the external environment. The cytoskeleton consists of three distinct biopolymers: actin filaments (microfilaments), intermediate filaments, and microtubules.

Actin filaments are found primarily in a cross-linked matrix immediately below the cell membrane and bundled together in stress fibres stretching from one end of the cell to another. They also provide a direct link for the cell with the external environment through their attachment to focal adhesion (FA) complexes; these complexes are collections of a variety of proteins, such as zyxin (Rottner, Krause et al. 2001), which assemble together at the basal surface of the cell. One of the key components of FAs are integrins, the transmembrane proteins which connect the interior of the cell with the extracellular matrix (ECM), which is a gel-like network of collagen and polysaccharides providing an external

scaffolding to the cell. Actin itself is found in two forms: as a globular protein (G-actin) alone, and assembled into a so-called polar, helical filament approximately 5-9nm in diameter (F-actin) with a plus and minus end. The binding of G-actin into filaments is ATP dependent; generally they are added to the plus-end of the filament, while more dissociate from the minus-end. In stable filaments, the addition and loss occur at relatively constant rates. This results in a gradual turnover of the individual G-actin monomers, a process known as treadmilling. These thin filaments can form into two- and three-dimensional cross-linked networks with the help of numerous actin-binding proteins, or into long linear bundles known as stress fibres, which will be discussed in more detail, along with actomyosin contractility in section 1.1.3.

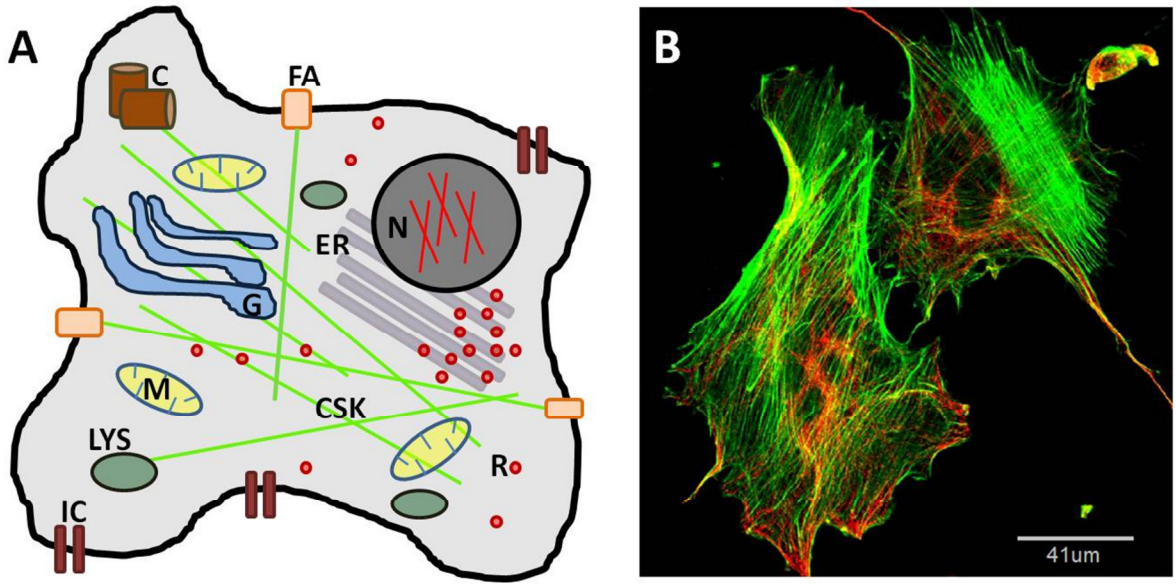

Figure 1.1: Mammalian Cell and the Cytoskeleton. The major components of the cell can be seen in (**A**). Within the surrounding plasma membrane (black line) are ion channels (IC) and focal adhesion complexes (FA), which are the link between cytoskeletal fibres and the extracellular matrix (not shown). The nucleus (N) is shown in dark grey with chromosomes shown as red X's. Mitochondria (M), the energy producers of the cell are shown in yellow. The Golgi apparatus (G) packages cellular components into lysosomes (LYS) and other compartments for distribution within and outside of the cell. The endoplasmic reticulum (ER) packages and distributes proteins made by the ribosomes (R). It is found in two types: smooth ER and rough ER which is so called because of the associated ribosomes. The centriole (C) is the origin of the mitotic spindle during mitosis. Throughout it all can be seen the cytoskeleton (CSK). A real image of a 3T3 fibroblast cell with the actin (green) and microtubule cytoskeleton (red) stained is shown in (**B**). This image is a maximum intensity Z projection of a stack of images taken with a Nikon A1R laser scanning confocal microscope; scale bar 41µm.

Microtubules are composed of tubulin; tubulin is found in two forms, α-tubulin and β-tubulin. These two subunits associate into heterodimers in complex with GTP (an energy molecule similar in function to ATP); these dimers polymerize end to end to form protofilaments. Thirteen protofilaments associate together in a parallel manner to form a hollow tube, giving microtubules their name. Microtubules are also considered a polar filament with a distinct plus and minus end; they are approximately 25nm in diameter. In the cell, in addition to providing support, microtubules act as a type of transportation highway, and are also heavily involved in cell division, forming the mitotic spindle which separates the chromosomes during mitosis. Microtubules exhibit a property known as dynamic instability; this means that, following hydrolysis of the enclosed GTP molecules to GDP, the association of each protofilament with each other is much reduced, and may rapidly depolymerize depending on signals within the cell. In motile cells, microtubules also form the basis for cilia and flagella, which propel the cell through its environment.

Intermediate filaments comprise a family of biopolymers which are classified in four main types. These sub-categories include proteins which are nuclear (lamins), vimentin-like, epithelial (keratins), and axonal (neurofilaments). Named for their diameter (~10nm) which lies between that of actin filaments and microtubules, intermediate filaments are similarly composed of smaller subunits which associate together to form a rope-like bundle. Intermediate filaments have highly varied roles within the cell, but serve mainly as structural and mechanical support (i.e. nuclear lamins around the nucleus). Intermediate filaments are considered highly deformable; they may undergo significant stress without breaking, and will return to their original form following stress removal.

The cytoskeleton can be thought of as being composed of three distinct polymeric networks, but it is important to recognize that the interconnections between each of these networks with themselves, other networks, organelles and the external environment cannot be ignored. There exist extensive actin-binding and microtubule-binding proteins, whose cross-linking significantly alters the composition of each individual network, precluding treatment as isolated polymers. Other cytoskeleton associated proteins which cannot be ignored are the motor proteins. Microtubules are often found in complex with kinesins and

dyneins which are transporter molecules; binding one end to a microtubule and the other to that which is being transported, these molecules 'walk' along the microtubule, bringing necessary materials to where they are needed within the cell. Actin is often found in complex with proteins of the myosin family. Myosin V acts like kinesins and dyneins, walking along actin filaments and transporting molecules in a similar manner. Myosin II however binds both of its ends to individual actin filaments and the pulling force exerted is the origin of contractility found within the cell.

1.1.3 Actin-Myosin Stress Fibre Complexes

The focus of the experiments within this thesis lies primarily in the actin stress fibre component of the cytoskeleton. Actin stress fibres are not, in fact, composed solely of actin filaments (Pellegrin and Mellor 2007); they are composed of short (~1-2μm) bundles of 10-30 actin filaments on average forming a wider fibre of about 300nm in diameter, though there exists significant variation (Cramer, Siebert et al. 1997). As can be seen in Figure 1.2, these bundles are connected together by alternating bands of the actin-binding protein, α-actinin and non-muscle myosin (myosin II), so called because of its presence in non-muscle cells; other actin-binding proteins like filamin are also sometimes present. Myosin II contains two actin-binding domains which are capable of 'walking' along actin fibres towards the plus-end following hydrolysis of ATP. This structure is not unlike that of a sarcomere, which provides the contraction power found in muscle cells (Peterson, Rajfur et al. 2004; Pellegrin and Mellor 2007). In order to generate a contractile force, adjacent parallel bundles of actin must therefore have opposite polarity for myosin II to pull the fibres towards each other.

There are three variations of stress fibres, depending on their location within the cell: transverse arcs, dorsal fibres and ventral fibres. Transverse arcs are transitory, short bundles of stress fibres which form behind the lamellipodia of motile cells. Dorsal stress fibres are attached to FAs at one end and extend upwards towards the dorsal side of the cell, eventually incorporating into the actin meshwork which is found below the membrane there. Ventral stress fibres, which are primarily under investigation in this thesis, extend along the basal surface of the cell, connecting to FAs at either end. In motile cells, actin-myosin complexes

play an important role, as they provide the contractile forces necessary to pull the cell along the surface upon which it is crawling (Wessells, Spooner et al. 1971; Pellegrin and Mellor 2007). In non-motile cells however, this contractile force still exists, especially within ventral stress fibres; the contractile force supported through this fibre transmits through the FA complexes to the ECM and exerts a traction force on the substrate. There have been some conflicting results published as to the polarity of the actin filaments found in each type of stress fibre (Peterson, Rajfur et al. 2004; Hotulainen and Lappalainen 2006; Pellegrin and Mellor 2007). This has been attributed to the different mechanisms of formation of dorsal versus ventral stress fibres in different cell types (Pellegrin and Mellor 2007).

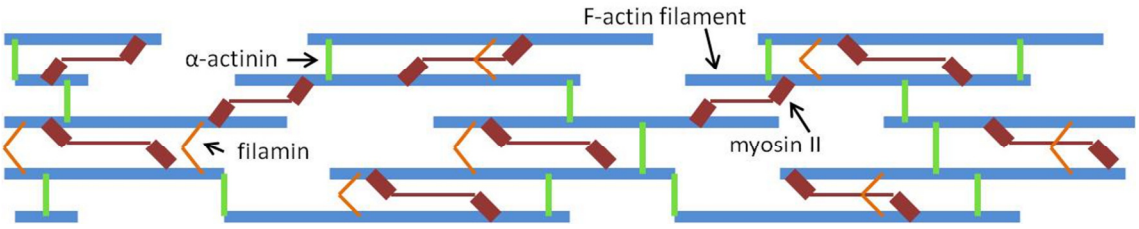

Figure 1.2: Sarcomeric-like structure of Actin-Myosin stress fibres. Actin stress fibres have a striated appearance which is due to the periodic cross-linking by α-actinin (green bands) and myosin II (red barbell like). Bundles of F-actin filaments are collected together by these proteins in a parallel fashion, often with adjacent filaments having opposite polarity. Myosin II causes contraction of the stress fibre by walking along the actin filaments towards the plus-end; this causes the actin filaments to come closer together, even intercalating and displacing actinin at times (Pellegrin and Mellor 2007). Other actin-binding proteins such as filamin (orange chevrons) can also be present.

1.1.4 Anti-Cytoskeletal Drugs

A number of chemicals have been discovered that have a specific action on the cytoskeleton and its associated proteins. Many of these have been used in experiments to selectively activate or inhibit aspects of the cytoskeleton in an effort to determine the specific role each cytoskeletal protein plays in mechanotransduction, among other processes. A number of the most popular are summarized in Table 1.1. Two of the drugs listed in this table (nocodazole and Y27632) are used in this thesis; the effect of these drugs on morphology and cortical elasticity can be found in Chapter 4.

Table 1.1: Anti-Cytoskeletal Drugs.

Drug Name	Cytoskeleton Component Affected	Method of Inhibition or Promotion	References
Nocodazole, Colcemid/Colchicine	Microtubules (MT)	Inhibits polymerization, leading to eventual MT dissolution	Rieder and Palazzo 1992; Pelling, Dawson et al. 2007
Cytochalasin B, D	Actin	Inhibit polymerization, leading to dissolution of filaments	Lin, Tobin et al. 1980
Y27632	Actin stress fibres	Inhibits Rho Kinase, inhibits stress fibres and contraction	Ishizaki, Uehata et al. 2000; Narumiya, Ishizaki et al. 2000
Blebbistatin	Myosin II	Lowers actin-myosin affinity, eliminates contraction	Straight, Cheung et al. 2003
Jasplakinolide	Actin	Stabilizes actin filaments by preventing depolymerization	Bubb, Senderowicz et al. 1994
Lysophosphatidic Acid	Actin stress fibres, contraction	Activates Rho Kinase; upregulates contraction	Zhang, Magnusson et al. 1997
Calyculin A	Actin stress fibres, contraction	Inhibits myosin light chain phosphatase, upregulates contraction	Hosoya, Mitsui et al. 1993; Peterson, Rajfur et al. 2004
Paclitaxel (Taxol)	Microtubules	Stabilizes microtubules	Zhang, Magnusson et al. 1997; Fu, Li et al. 2009

1.2 Mechanotransduction through the Cytoskeleton

Cells in the human body experience forces from their surrounding environment on a constant basis. Some key examples are the fluid shear force of blood flowing past epithelial cells in blood vessels, or the stretching of the extracellular matrix as a muscle contracts,

pulling on the cells to which it is attached. Oftentimes, these mechanical signals cause reactions on the molecular and biochemical levels of the cell (Sato, Levesque et al. 1987; Kuchan and Frangos 1993; Bachrach, Valhmu et al. 1995; Buschmann, Gluzband et al. 1995; Huicong 1995; Liu 1998; Jen, Jhiang et al. 2000). This is known as mechanosensitivity; the ability for a cell or cellular components to sense a mechanical signal. Mechanotransduction, however, is the ability for a mechanical stimulus to be transmitted into a useful chemical or biochemical signal; this is a concept being rigorously studied in the field of biophysics (Jaalouk and Lammerding 2009; Wang, Tytell et al. 2009). In cells, it is known that the surrounding mechanical environment and its signals play a significant role in determining stem cell fate, regulating genes, and has a role in disease processes such as cancer metastasis, among others (Engler, Sen et al. 2006; Hinz 2006; Chiquet, Tunc-Civelek et al. 2007; Bader and Knight 2008; Lopez, Mouw et al. 2008). Though the exact process of mechanotransduction and its pathways have yet to be elucidated, there is increasing evidence that one major key to understanding mechanotransduction lies within the dynamics of the cytoskeleton during a mechanical stimulus (Wang, Tytell et al. 2009; Fletcher and Mullins 2010)

As early as the seventeenth century, some of the first microscopes were being used by Antony van Leeuwenhoek to study the motion of cells themselves, and the particles within them in an attempt to understand viscosity, and fluid flow within cells, among other things (Pelling and Horton 2008). Technology not being advanced enough to allow good quantitative measurements at this time, it was not until the early twentieth century that many physical properties began to be described in publications (Pelling and Horton 2008). About thirty years ago, extensive experiments were performed to determine the mechanical properties of a variety of cell types. The most commonly used techniques at the time were micropipette aspiration (Evans 1973; Chien, Sung et al. 1978; Sato, Levesque et al. 1987; Sato, Levesque et al. 1987; Evans and Yeung 1989; Mohandas and Evans 1989; Discher, Boal et al. 1998), rudimentary 'cell poking' and other micromanipulation with glass needles (Petersen, McConnaughey et al. 1982; Albrecht-Buehler 1987), and application of a shear, twisting force using magnetic fields and ferromagnetic beads (Valberg and Albertini 1985; Valberg and Feldman 1987; Bizal, Butler et al. 1991; Wang, Butler et al. 1993; Wang and Ingber 1994). Many of these initial experiments led to an understanding of which

components of the cell contributed significantly to maintaining these properties, namely, the cytoskeleton.

Early micropipette aspiration experiments were performed on red blood cells (Rand 1964; Rand and Burton 1964; Evans 1973; Chien, Sung et al. 1978), as they were observed to be some of the simplest cells and some of the most readily available. Red blood cells have no nucleus, nor do they have many complex organelles. As well, they have a very particular cytoskeleton: a cortical ring of a protein called spectrin which allows the cell to maintain its characteristic disk shape (Discher, Mohandas et al. 1994). As red blood cells are constantly compressed and deformed as they flow through capillaries to exchange oxygen with the surrounding tissue, there was a strong push to understand how the cell responds to such a mechanical stimulus. Micropipette aspiration, which is characterized by the sucking of a part or all of a cell into a thin glass tube using a pressure differential, was easily performed on these cells, and simulated flow into a capillary quite well. By analyzing the radii and distance travelled within the micropipette, it was a straightforward matter to extract the cortical tension of the membrane and underlying cytoskeleton as well as the viscosity of the cell from the experimental measurements (Evans and Yeung 1989). Similar experiments performed on neutrophils revealed a value of 30pN/μm for the cortical tension, and a viscosity on the order of 100 Pa·s (Evans and Yeung 1989; Hochmuth 2000). Further experiments were performed on stiffer cell types such as chondrocytes and endothelial cells; these cells did not flow into the micropipettes in the same manner as did the softer cells, instead they behaved as solids. This allowed for the extraction of a value of Young's Modulus of Elasticity (E =stress/strain) on the order of 0.5kPa (Hochmuth 2000).

Experiments performed with micropipette aspiration led to a number of cell models based on a continuum mechanics treatment of the cell (see Chapter 2.4). However, valid as these models are for simple cells such as red blood cells, they fail to take into account the complexities (such as the cytoskeleton) that exist in nearly every other cell type in the human body. Further, these experiments provide values of viscosity and cortical elasticity along with other properties of the 'whole cell'. As the cell is highly inhomogeneous, it is unwise to assume that values which apply to the whole cell would apply uniformly throughout the different areas of a cell in real life.

In the late 1980s, experiments employing localized applications of force began to emerge, and with them the first implications of the role of the cytoskeleton in mechanotransduction. One such experiment was performed in which protruded extensions of fibroblast cells (containing actin stress fibres) retracted following detachment from the surface by glass microneedles (Albrecht-Buehler 1987). It was concluded that this retraction must be due to either the movement or depolymerisation of actin filaments, as neither cytochalasin B (see Table 1.1) nor colcemid had any effect on the observed retraction. Supporting this result, micropipette aspiration experiments determined that after the application of a shear stress, epithelial cells had stiffer mechanical properties and retained their elongated shape (as seen through staining for F-actin) following detachment from the culture surface as compared to cells which had not experienced a mechanical stimulus (Sato, Levesque et al. 1987).

More recently, laser ablation experiments, in which actin stress fibres are severed using femtosecond laser pulses, suggest that these earlier observed trends are largely due to actin retraction, and not depolymerisation (Kumar, Maxwell et al. 2006; Stachowiak and O'Shaughnessy 2009). Further recent experiments demonstrate that retracting stress fibres form pseudo FA sites along the basal membrane as they slide along it (Colombelli, Besser et al. 2009). Studies have also demonstrated that zyxin, a FA protein, acts as a mechanical 'tension sensor'. Zyxin appears to localize at points of increased tension along the actin cytoskeleton and at adhesion sites, both new and old, and disappears immediately following a loss of tension (Nix, Fradelizi et al. 2001; Rottner, Krause et al. 2001; Hirata, Tatsumi et al. 2008; Hirata, Tatsumi et al. 2008; Colombelli, Besser et al. 2009). This recoil response of severed actin fibres has been attributed to the action of actin-myosin contraction and an existing pre-stress or tension along the fibre (Colombelli, Besser et al. 2009; Stachowiak and O'Shaughnessy 2009); the exact cause has not yet been precisely determined.

In the early 1990s, a series of experiments using a magnetic twisting device indicated that applied force was transmitted through integrin receptors found at FA points, which are directly connected to the cytoskeleton (Wang, Butler et al. 1993; Wang and Ingber 1994; Ingber 1997). In these experiments, ferromagnetic beads were allowed to adhere to the surface of a cell for a period of 10-15 minutes. Following this, the magnetic moments of the

beads were aligned using a strong pulse of magnetic field; a perpendicular, weaker field was then applied to apply a shear twisting force to the surface of the cell via the magnetic beads. Resistance as provided by the bead's connection to the cell prevented the bead from fully aligning with the applied magnetic field; the remnant magnetic field was measured using a magnetometer and from this, the angular strain was determined (Wang, Butler et al. 1993). These experiments led to a prediction of a model of 'tensegrity' (Ingber, Dike et al. 1994; Ingber 1997), which will be fully discussed in Chapter 2.4, and by taking the ratio of angular strain to applied stress, an expression of cell stiffness was calculated (Wang, Butler et al. 1993). This allowed for the comparison of results with the effect of several anti-cytoskeletal drugs, leading to the implication of all three cytoskeleton polymers are involved in the transmission of force (Wang, Butler et al. 1993; Wang and Ingber 1994).

As FAs are the direct link that the cytoskeleton has to the extracellular environment, many further investigations into their properties have been carried out (Burridge, Fath et al. 1988; Weisberg, Sattler et al. 1997; Mierke 2009). Experiments involving direct micromanipulation of cells expressing actin tagged with green fluorescent protein (GFP) with glass needles demonstrated a local response to the transmission of force through FA complexes (Heidemann, Kaech et al. 1999). Moreover, experiments involving locally applied forces to cell membranes have demonstrated that increased force on FA complexes and stress fibres leads to an increased calcium ion influx near those FAs (Ko and McCulloch 2000; Charras and Horton 2002; Charras, Williams et al. 2004; Formigli, Meacci et al. 2007). This supports the theory that mechanosensitive ion channels can also be activated by increased tension in the cytoskeleton (Hayakawa, Tatsumi et al. 2008), and gives further evidence that FA complexes and the cytoskeleton are intimately involved in mechanotransduction.

1.3 Simultaneous Optical and Atomic Force Microscopy studying Mechanotransduction

The Atomic Force Microscope (AFM) was first invented in 1986 (Binnig, Quate et al. 1986) as a descendent of the Scanning Tunnelling Microscope (STM) (Binnig 1982). A full technical description of these instruments and their usages follows in Chapter 2.1. Originally

intended for use in measuring topography of non-conducting or semi-conducting surfaces at atomic resolution (Binnig, Quate et al. 1986), the ability of the AFM to apply a known, controlled force to specific locations on a cell was quickly employed in the field of cell biology and biophysics (Radmacher, Tillamnn et al. 1992). By the early 1990s, the AFM was being used to confirm and expand upon the cellular rheological measurements made in previous years (Henderson, Haydon et al. 1992; Radmacher, Tillamnn et al. 1992; Hoh and Schoenenberger 1994) and, in the last decade, AFM has emerged as a primary tool for investigating the mechanical signalling pathways within cells (Czajkowsky, Iwamoto et al. 2000; Lehenkari, Charras et al. 2000; Costa, Sim et al. 2006; Haupt, Pelling et al. 2006; Radmacher 2007; Trache and Lim 2009).

An important advancement of the use of AFM to study biological samples was its integration with optical and fluorescent microscopes (Charras, Lehenkari et al. 2001; Charras and Horton 2002; Haupt, Pelling et al. 2006). In the late 1990s, the popularization of fluorescent tags, particularly with the use of fluorescent proteins and dyes, became useful for direct visualization of the effect of an applied force on the inner structures of the cell (Heidemann, Kaech et al. 1999). The combination of employing AFM with simultaneous fluorescence and laser scanning confocal microscopy (LSCM; a complete and in depth technical description of this follows in Chapter 2.2) has further allowed for direct correlation between local mechanical properties measured with the AFM and specific subcellular structures and dynamics (Lehenkari, Charras et al. 2000; Silberberg, Pelling et al. 2008; Pelling, Veraitch et al. 2009).

As an example of the specific usefulness of simultaneous AFM/LSCM, let us consider a series of experiments performed by Charras *et al.* (Charras, Lehenkari et al. 2001; Charras and Horton 2002). In these experiements, the AFM was used to apply a local force to the surface of osteoblasts while the dynamics of intracellular calcium concentration were observed with confocal microscopy; calcium levels were measured through the use of a calcium activated fluorescent dye whose intensity is correlated to the calcium concentration. It was observed directly that intracellular calcium levels increase in response to force application, facilitating the opening of stress activated channels, and this calcium further propagates to adjacent cells through gap junctions (Charras, Lehenkari et al. 2001). The use

of cytoskeleton-specific drugs, such as nocodazole and cytochalasin B, revealed a secondary response pathway during the relaxation of cells following the removal of force which was dependant on the presence of microtubules (Charras and Horton 2002). While this response was not dependant on the F-actin cytoskeleton, similar experiments performed on C2C12 myoblasts revealed that calcium dynamics were in fact dependant on the F-actin network (Formigli, Meacci et al. 2005; Formigli, Meacci et al. 2007; Sbrana, Sassoli et al. 2008).

Experiments such as these and others (Wu, Kuhn et al. 1998; Rotsch and Radmacher 2000; Charras and Horton 2002; Kasas, Wang et al. 2005; Pelling, Dawson et al. 2007) which reveal conflicting results in the nature of the cellular and cytoskeletal response to force emphasize the importance of considering the specifics of each experiment. It is now clear that the relative roles which particular elements of the cytoskeleton play in governing the mechanical properties of the cell are extremely cell type and time dependent, and vary depending on the specific process which the cell is undergoing (i.e. mitosis (Matzke, Jacobson et al. 2001; Kunda, Pelling et al. 2008)).

While the long-term (up to an hour or more) downstream effects of physical forces on cell behaviour have been intensively studied (Henderson, Haydon et al. 1992; Heidemann, Kaech et al. 1999; Radmacher 2002; Radmacher 2007; Trache and Lim 2009), much less has been done to study the immediate (seconds to minutes) response of a cell to force. In particular, integrated AFM/Spinning Disk Confocal Microscopy (see Section 2.2.4) experiments have been performed previously on cells transfected for actin-GFP (Trache and Lim 2009). However, Trache and Lim, while demonstrating the reorganization of actin stress fibres in response to a locally applied force, fail to indicate the magnitude of the force applied, as well as perform imaging over extremely long time scales (6-10 images in ~80 minutes). In contrast, in this thesis, we present data which demonstrate the very short term (~4 minutes), force-dependent response of cells, generally apparent as structural deformation. This short-term response remains poorly understood, even though it would appear to be highly influential in the long-term cytoskeletal reorganization and gene regulation observed in cells (Chiquet, Tunc-Civelek et al. 2007; Trache and Lim 2009). The data presented in this thesis is unique in its elucidation of the rapid response of cells to a locally applied force. Simultaneous imaging of the actin cytoskeleton with LSCM while an

AFM is used to apply a force directly over the cell nucleus allows us to quantify for the first time the force dependence of the structural remodelling of actin stress fibres in response to force as well as strain dynamics along the length of these fibres. Importantly, contrary to popular belief, both the displacement of stress fibres and strain dynamics are not isotropic in nature, further confirming the complexity of cellular mechanotransduction.

1.4 References

Alberts, B., A. Johnson, J. Lewis, M. Raff, K. Roberts, P. Walter (2002). The Cytoskeleton. Molecular Biology of the Cell. New York, Garland Science.

Albrecht-Buehler, G. (1987). "Role of cortical tension in fibroblast shape and movement." Cell Motil Cytoskeleton **7**(1): 54-67.

Bachrach, N. M., W. B. Valhmu, et al. (1995). "Changes in proteoglycan synthesis of chondrocytes in articular cartilage are associated with the time-dependent changes in their mechanical environment." J Biomech **28**(12): 1561-9.

Bader, D. L. and M. M. Knight (2008). "Biomechanical analysis of structural deformation in living cells." Med Biol Eng Comput **46**(10): 951-63.

Binnig, G., H. Rohrer, Ch. Gerber, E. Weibel (1982). "Surface Studies by Scanning Tunneling Microscopy." Phys Rev Lett **49**(1): 57-61.

Binnig, G., C. F. Quate, et al. (1986). "Atomic force microscope." Phys Rev Lett **56**(9): 930-933.

Bizal, C. L., J. P. Butler, et al. (1991). "Viscoelastic and motile properties of hamster lung and peritoneal macrophages." J Leukoc Biol **50**(3): 240-51.

Bubb, M. R., A. M. Senderowicz, et al. (1994). "Jasplakinolide, a cytotoxic natural product, induces actin polymerization and competitively inhibits the binding of phalloidin to F-actin." J Biol Chem **269**(21): 14869-71.

Burridge, K., K. Fath, et al. (1988). "Focal adhesions: transmembrane junctions between the extracellular matrix and the cytoskeleton." Annu Rev Cell Biol **4**: 487-525.

Buschmann, M. D., Y. A. Gluzband, et al. (1995). "Mechanical compression modulates matrix biosynthesis in chondrocyte/agarose culture." J Cell Sci **108 (Pt 4)**: 1497-508.

Charras, G. T. and M. A. Horton (2002). "Determination of cellular strains by combined atomic force microscopy and finite element modeling." Biophys J **83**(2): 858-79.

Charras, G. T. and M. A. Horton (2002). "Single cell mechanotransduction and its modulation analyzed by atomic force microscope indentation." Biophys J **82**(6): 2970-81.

Charras, G. T., P. P. Lehenkari, et al. (2001). "Atomic force microscopy can be used to mechanically stimulate osteoblasts and evaluate cellular strain distributions." Ultramicroscopy **86**(1-2): 85-95.

Charras, G. T., B. A. Williams, et al. (2004). "Estimating the sensitivity of mechanosensitive ion channels to membrane strain and tension." Biophys J **87**(4): 2870-84.

Chien, S., K. L. Sung, et al. (1978). "Theoretical and experimental studies on viscoelastic properties of erythrocyte membrane." Biophys J **24**(2): 463-87.

Chiquet, M., V. Tunc-Civelek, et al. (2007). "Gene regulation by mechanotransduction in fibroblasts." Appl Physiol Nutr Metab **32**(5): 967-73.

Colombelli, J., A. Besser, et al. (2009). "Mechanosensing in actin stress fibers revealed by a close correlation between force and protein localization." J Cell Sci **122**(Pt 10): 1665-79.

Costa, K. D., A. J. Sim, et al. (2006). "Non-Hertzian approach to analyzing mechanical properties of endothelial cells probed by atomic force microscopy." J Biomech Eng **128**(2): 176-84.

Cramer, L. P., M. Siebert, et al. (1997). "Identification of novel graded polarity actin filament bundles in locomoting heart fibroblasts: implications for the generation of motile force." J Cell Biol **136**(6): 1287-305.

Czajkowsky, D. M., H. Iwamoto, et al. (2000). "Atomic force microscopy in structural biology: from the subcellular to the submolecular." J Electron Microsc (Tokyo) **49**(3): 395-406.

Discher, D. E., D. H. Boal, et al. (1998). "Simulations of the erythrocyte cytoskeleton at large deformation. II. Micropipette aspiration." Biophys J **75**(3): 1584-97.

Discher, D. E., N. Mohandas, et al. (1994). "Molecular maps of red cell deformation: hidden elasticity and in situ connectivity." Science **266**(5187): 1032-5.

Engler, A. J., S. Sen, et al. (2006). "Matrix elasticity directs stem cell lineage specification." Cell **126**(4): 677-89.

Evans, E. and A. Yeung (1989). "Apparent viscosity and cortical tension of blood granulocytes determined by micropipet aspiration." Biophys J **56**(1): 151-60.

Evans, E. A. (1973). "New membrane concept applied to the analysis of fluid shear- and micropipette-deformed red blood cells." Biophys J **13**(9): 941-54.

Fletcher, D. A. and R. D. Mullins (2010). "Cell mechanics and the cytoskeleton." Nature **463**(7280): 485-92.

Formigli, L., E. Meacci, et al. (2005). "Sphingosine 1-phosphate induces cytoskeletal reorganization in C2C12 myoblasts: physiological relevance for stress fibres in the modulation of ion current through stretch-activated channels." J Cell Sci **118**(Pt 6): 1161-71.

Formigli, L., E. Meacci, et al. (2007). "Cytoskeleton/stretch-activated ion channel interaction regulates myogenic differentiation of skeletal myoblasts." J Cell Physiol **211**(2): 296-306.

Fu, Y., S. Li, et al. (2009). "Medicinal chemistry of paclitaxel and its analogues." Curr Med Chem **16**(30): 3966-85.

Haupt, B. J., A. E. Pelling, et al. (2006). "Integrated confocal and scanning probe microscopy for biomedical research." ScientificWorldJournal **6**: 1609-18.

Hayakawa, K., H. Tatsumi, et al. (2008). "Actin stress fibers transmit and focus force to activate mechanosensitive channels." J Cell Sci **121**(Pt 4): 496-503.

Heidemann, S. R., S. Kaech, et al. (1999). "Direct observations of the mechanical behaviors of the cytoskeleton in living fibroblasts." J Cell Biol **145**(1): 109-22.

Henderson, E., P. G. Haydon, et al. (1992). "Actin filament dynamics in living glial cells imaged by atomic force microscopy." Science **257**(5078): 1944-6.

Hinz, B. (2006). "Masters and servants of the force: the role of matrix adhesions in myofibroblast force perception and transmission." Eur J Cell Biol **85**(3-4): 175-81.

Hirata, H., H. Tatsumi, et al. (2008). "Mechanical forces facilitate actin polymerization at focal adhesions in a zyxin-dependent manner." J Cell Sci **121**(Pt 17): 2795-804.

Hirata, H., H. Tatsumi, et al. (2008). "Zyxin emerges as a key player in the mechanotransduction at cell adhesive structures." Commun Integr Biol **1**(2): 192-195.
Hochmuth, R. M. (2000). "Micropipette aspiration of living cells." J Biomech **33**(1): 15-22.
Hoh, J. H. and C. A. Schoenenberger (1994). "Surface morphology and mechanical properties of MDCK monolayers by atomic force microscopy." J Cell Sci **107 (Pt 5)**: 1105-14.
Hosoya, N., M. Mitsui, et al. (1993). "Changes in the cytoskeletal structure of cultured smooth muscle cells induced by calyculin-A." J Cell Sci **105 (Pt 4)**: 883-90.
Hotulainen, P. and P. Lappalainen (2006). "Stress fibers are generated by two distinct actin assembly mechanisms in motile cells." J Cell Biol **173**(3): 383-94.
Huicong, W., W. Ip, R. Boissy, E.S. Grood (1995). "Cell Orientation response to cyclically deformed substrates: experimental validation of a cell model." J Biomech **28**(12): 545-564.
Ingber, D. E. (1997). "Integrins, tensegrity, and mechanotransduction." Gravit Space Biol Bull **10**(2): 49-55.
Ingber, D. E. (1997). "Tensegrity: the architectural basis of cellular mechanotransduction." Annu Rev Physiol **59**: 575-99.
Ingber, D. E., L. Dike, et al. (1994). "Cellular tensegrity: exploring how mechanical changes in the cytoskeleton regulate cell growth, migration, and tissue pattern during morphogenesis." Int Rev Cytol **150**: 173-224.
Ishizaki, T., M. Uehata, et al. (2000). "Pharmacological properties of Y-27632, a specific inhibitor of rho-associated kinases." Mol Pharmacol **57**(5): 976-83.
Jaalouk, D. E. and J. Lammerding (2009). "Mechanotransduction gone awry." Nat Rev Mol Cell Biol **10**(1): 63-73.
Jen, C. J., S. J. Jhiang, et al. (2000). "Invited review: effects of flow on vascular endothelial intracellular calcium signaling of rat aortas ex vivo." J Appl Physiol **89**(4): 1657-62; discussion 1656.
Kasas, S., X. Wang, et al. (2005). "Superficial and deep changes of cellular mechanical properties following cytoskeleton disassembly." Cell Motil Cytoskeleton **62**(2): 124-32.
Ko, K. S. and C. A. McCulloch (2000). "Partners in protection: interdependence of cytoskeleton and plasma membrane in adaptations to applied forces." J Membr Biol **174**(2): 85-95.
Kuchan, M. J. and J. A. Frangos (1993). "Shear stress regulates endothelin-1 release via protein kinase C and cGMP in cultured endothelial cells." Am J Physiol **264**(1 Pt 2): H150-6.
Kumar, S., I. Z. Maxwell, et al. (2006). "Viscoelastic retraction of single living stress fibers and its impact on cell shape, cytoskeletal organization, and extracellular matrix mechanics." Biophys J **90**(10): 3762-73.
Kunda, P., A. E. Pelling, et al. (2008). "Moesin controls cortical rigidity, cell rounding, and spindle morphogenesis during mitosis." Curr Biol **18**(2): 91-101.
Lehenkari, P. P., G. T. Charras, et al. (2000). "Adapting atomic force microscopy for cell biology." Ultramicroscopy **82**(1-4): 289-95.
Lin, D. C., K. D. Tobin, et al. (1980). "Cytochalasins inhibit nuclei-induced actin polymerization by blocking filament elongation." J Cell Biol **84**(2): 455-60.
Liu, S. Q. (1998). "Influence of tensile strain on smooth muscle cell orientation in rat blood vessels." J Biomech Eng **120**(3): 313-20.

Lopez, J. I., J. K. Mouw, et al. (2008). "Biomechanical regulation of cell orientation and fate." Oncogene **27**(55): 6981-93.
Matzke, R., K. Jacobson, et al. (2001). "Direct, high-resolution measurement of furrow stiffening during division of adherent cells." Nat Cell Biol **3**(6): 607-10.
Mierke, C. T. (2009). "The role of vinculin in the regulation of the mechanical properties of cells." Cell Biochem Biophys **53**(3): 115-26.
Mohandas, N. and E. Evans (1989). "Rheological and adherence properties of sickle cells. Potential contribution to hematologic manifestations of the disease." Ann N Y Acad Sci **565**: 327-37.
Narumiya, S., T. Ishizaki, et al. (2000). "Use and properties of ROCK-specific inhibitor Y-27632." Methods Enzymol **325**: 273-84.
Nix, D. A., J. Fradelizi, et al. (2001). "Targeting of zyxin to sites of actin membrane interaction and to the nucleus." J Biol Chem **276**(37): 34759-67.
Pellegrin, S. and H. Mellor (2007). "Actin stress fibres." J Cell Sci **120**(Pt 20): 3491-9.
Pelling, A. E., D. W. Dawson, et al. (2007). "Distinct contributions of microtubule subtypes to cell membrane shape and stability." Nanomedicine **3**(1): 43-52.
Pelling, A. E. and M. A. Horton (2008). "An historical perspective on cell mechanics." Pflugers Arch **456**(1): 3-12.
Pelling, A. E., F. S. Veraitch, et al. (2009). "Mechanical dynamics of single cells during early apoptosis." Cell Motil Cytoskeleton **66**(7): 409-22.
Petersen, N. O., W. B. McConnaughey, et al. (1982). "Dependence of locally measured cellular deformability on position on the cell, temperature, and cytochalasin B." Proc Natl Acad Sci U S A **79**(17): 5327-31.
Peterson, L. J., Z. Rajfur, et al. (2004). "Simultaneous stretching and contraction of stress fibers in vivo." Mol Biol Cell **15**(7): 3497-508.
Radmacher, M. (2002). "Measuring the elastic properties of living cells by the atomic force microscope." Methods Cell Biol **68**: 67-90.
Radmacher, M. (2007). "Studying the mechanics of cellular processes by atomic force microscopy." Methods Cell Biol **83**: 347-72.
Radmacher, M., R. W. Tillamnn, et al. (1992). "From molecules to cells: imaging soft samples with the atomic force microscope." Science **257**(5078): 1900-5.
Rand, R. P. (1964). "Mechanical Properties of the Red Cell Membrane. Ii. Viscoelastic Breakdown of the Membrane." Biophys J **4**: 303-16.
Rand, R. P. and A. C. Burton (1964). "Mechanical Properties of the Red Cell Membrane. I. Membrane Stiffness and Intracellular Pressure." Biophys J **4**: 115-35.
Rieder, C. L. and R. E. Palazzo (1992). "Colcemid and the mitotic cycle." J Cell Sci **102 (Pt 3)**: 387-92.
Rotsch, C. and M. Radmacher (2000). "Drug-induced changes of cytoskeletal structure and mechanics in fibroblasts: an atomic force microscopy study." Biophys J **78**(1): 520-35.
Rottner, K., M. Krause, et al. (2001). "Zyxin is not colocalized with vasodilator-stimulated phosphoprotein (VASP) at lamellipodial tips and exhibits different dynamics to vinculin, paxillin, and VASP in focal adhesions." Mol Biol Cell **12**(10): 3103-13.
Sato, M., M. J. Levesque, et al. (1987). "An application of the micropipette technique to the measurement of the mechanical properties of cultured bovine aortic endothelial cells." J Biomech Eng **109**(1): 27-34.

Sato, M., M. J. Levesque, et al. (1987). "Micropipette aspiration of cultured bovine aortic endothelial cells exposed to shear stress." Arteriosclerosis **7**(3): 276-86.

Sbrana, F., C. Sassoli, et al. (2008). "Role for stress fiber contraction in surface tension development and stretch-activated channel regulation in C2C12 myoblasts." Am J Physiol Cell Physiol **295**(1): C160-72.

Silberberg, Y. R., A. E. Pelling, et al. (2008). "Mitochondrial displacements in response to nanomechanical forces." J Mol Recognit **21**(1): 30-6.

Stachowiak, M. R. and B. O'Shaughnessy (2009). "Recoil after severing reveals stress fiber contraction mechanisms." Biophys J **97**(2): 462-71.

Straight, A. F., A. Cheung, et al. (2003). "Dissecting temporal and spatial control of cytokinesis with a myosin II Inhibitor." Science **299**(5613): 1743-7.

Trache, A. and S. M. Lim (2009). "Integrated microscopy for real-time imaging of mechanotransduction studies in live cells." J Biomed Opt **14**(3): 034024.

Valberg, P. A. and D. F. Albertini (1985). "Cytoplasmic motions, rheology, and structure probed by a novel magnetic particle method." J Cell Biol **101**(1): 130-40.

Valberg, P. A. and H. A. Feldman (1987). "Magnetic particle motions within living cells. Measurement of cytoplasmic viscosity and motile activity." Biophys J **52**(4): 551-61.

Wang, N., J. P. Butler, et al. (1993). "Mechanotransduction across the cell surface and through the cytoskeleton." Science **260**(5111): 1124-7.

Wang, N. and D. E. Ingber (1994). "Control of cytoskeletal mechanics by extracellular matrix, cell shape, and mechanical tension." Biophys J **66**(6): 2181-9.

Wang, N., J. D. Tytell, et al. (2009). "Mechanotransduction at a distance: mechanically coupling the extracellular matrix with the nucleus." Nat Rev Mol Cell Biol **10**(1): 75-82.

Weisberg, E., M. Sattler, et al. (1997). "Role of focal adhesion proteins in signal transduction and oncogenesis." Crit Rev Oncog **8**(4): 343-58.

Wessells, N. K., B. S. Spooner, et al. (1971). "Microfilaments in cellular and developmental processes." Science **171**(967): 135-43.

Wu, H. W., T. Kuhn, et al. (1998). "Mechanical properties of L929 cells measured by atomic force microscopy: effects of anticytoskeletal drugs and membrane crosslinking." Scanning **20**(5): 389-97.

Zhang, Q., M. K. Magnusson, et al. (1997). "Lysophosphatidic acid and microtubule-destabilizing agents stimulate fibronectin matrix assembly through Rho-dependent actin stress fiber formation and cell contraction." Mol Biol Cell **8**(8): 1415-25.

Chapter Two:

Theories and Use of Microscopy Techniques

In this thesis, I will report on the investigation of the effect of a locally applied force on the actin cytoskeleton of 3T3 Fibroblast cells. These cells were submitted to an applied force using an Atomic Force Microscope (AFM) while simultaneous imaging was performed using a Laser-Scanning Confocal Microscope (LSCM). To visualize the movements of the actin cytoskeleton and other proteins of interest, cells were transfected to transiently express proteins conjugated to fluorescent proteins, thus making them visible by confocal microscopy. The movements of actin in response to an applied force will help to elucidate the mechanotransduction pathways within the cell. The experiments described in this thesis make use of a variety of advanced microscopy and imaging techniques, each of which will be described in detail below.

2.1 Atomic Force Microscopy

The Atomic Force Microscope (AFM) was developed in 1986 as an extension of the Scanning Tunnelling Microscope (STM) (Binnig 1982; Binnig, Quate et al. 1986). The STM has been primarily used to measure topographies and surface properties of conductive materials at atomic resolution (Binnig 1982; Baro, Miranda et al. 1985; Binnig, Frank et al. 1985; Hansma, Elings et al. 1988). The STM measures topography by raster-scanning the surface with an extremely sharp tip to which a bias voltage has been applied. Raster-scanning is a technique in which single lines are scanned one at a time in a single direction before moving on to the next line. Due to the quantum mechanical effect of electron tunnelling through a vacuum, a tunnelling current can be measured as the sample is scanned, provided the sample is sufficiently conductive (Binnig 1982); changes in current can then be directly related to height changes between the sample and the tip in a highly sensitive manner. This current (I) exponentially decays with distance (Eq. [1]).

$$I \propto e^{-1.025\sqrt{\Phi}d} \quad [1]$$

An increase in barrier distance (d, measured in Å) of 2-5Å (typical atomic radius) will decrease the current by upwards of 3 magnitudes. This indicates that the current measured is largely coming from the single atom at the end of the STM tip. The energy barrier (Φ, eV) is dependent on the applied voltage, and the factor 1.025 is derived from $A =$

$\sqrt{2m}/\hbar$, where m is the mass of an electron, A is a constant equal to 1.025, and $\hbar$ is Planck's constant divided by 2π (Binnig 1982).

Once atomic resolution was achieved, it became highly attractive to image biological samples in this manner. Advances in the technique to allow for imaging in ambient temperature and pressure (Baro, Miranda et al. 1985; Hansma, Elings et al. 1988; Drake, Prater et al. 1989) allowed biological samples such as bacteriophages, DNA in complex with the enzyme recA, and lipid membranes to be imaged using an STM (Baro, Miranda et al. 1985; Smith, Bryant et al. 1987; Barris, Knipping et al. 1988); however, resolution was lacking. This was due to two main problems. Certain biological samples will conduct electrons, but it is a much weaker current than metallic samples, and not all regions are fully resolvable on the atomic scale (Baro, Miranda et al. 1985; Hansma, Elings et al. 1988). To adjust for this, images were created with biological samples coated in a thin conducting layer, or, as in Transmission Electron Microscopy (TEM), using masks of the metallic coating of the biological sample, with the sample itself removed (Hansma, Elings et al. 1988). However, coating a sample allows atomic resolution of only the metal coating, rather than the underlying sample. It also precludes any imaging of a biological sample in its natural environment; for true atomic resolution, too many modifications are necessary to truly image biological samples. The sharp tip required for STM can also be highly detrimental to soft biological samples which have not been further protected (Hansma, Elings et al. 1988). The AFM, in contrast, directly profiles the topography of a sample through physical contact between a sharp tip (described below) and the surface. This can be achieved on non-conducting surfaces eliminating the need to measure changes in tunnelling current to determine sample topography. Moreover, physical interaction forces between a sample and the tip can also be measured. The AFM may also be used in aqueous environments and in a range of temperatures; all of these qualities make it an ideal tool to study biological samples in their native environment (Radmacher, Tillamnn et al. 1992).

2.1.1 Schematic of Atomic Force Microscope

In principle, the AFM operates by measuring the deflection of a spring-like cantilever (to which a sharp, usually pyramidal, tip is attached) as it raster scans the surface (see Figure 2.1). Deflections of the cantilever are detected using a laser which reflects off its upper surface onto a quadrant photodiode, as pioneered by Meyer and Amer (Meyer 1990). In our set-up, the AFM makes use of a stationary stage while the scanning movement of the tip is controlled with a piezoelectric crystal. The cantilever of an AFM is effective in measuring forces because they follow Hooke's Law [2] for small displacements. Thus, with the spring constant (k) known, all deflection measurements (x) can be directly converted to force (F) values (Meyer 1990). This is used specifically in our experiments by setting the force we wish to apply, known as the setpoint value, and allowing the feedback loop to correct the piezo height in order to keep this force value constant.

$$F = k \cdot x \quad [2]$$

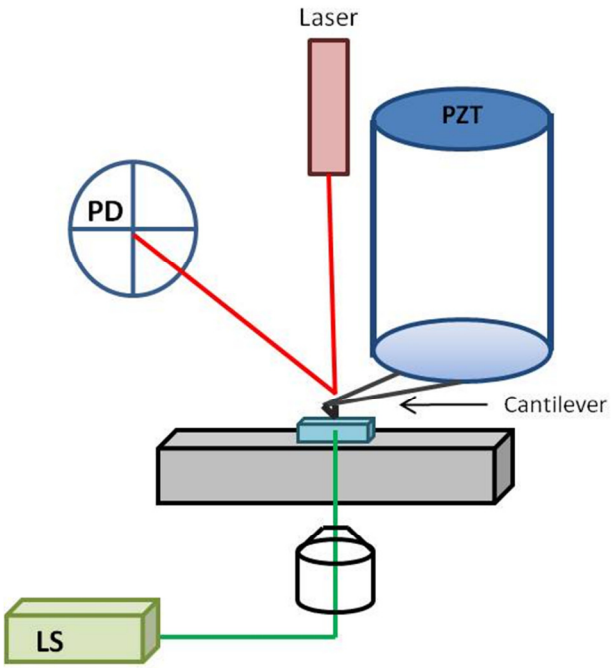

Figure 2.1: Schematic of an Atomic Force Microscope. Deflection of the cantilever is detected using a laser source reflecting off its back coating onto a quadrant photodiode (PD). Voltage changes are fed back to the piezo tube scanner (PZT) which expands or contracts to correct the tip height, returning the laser deflection back to zero. Samples may be imaged optically from below using a variety of light sources (LS) and objectives.

Piezoelectric materials, which were discovered and characterized over one hundred years ago by the Curie brothers (Curie 1880), are unique in their ability to create an electric field when strain is applied along an axis (direct piezoelectric effect) or to expand and contract in response to an applied electric field (converse piezoelectric effect) (Taylor 1985). In an AFM, the crystal employed expands and contracts in response to changes in voltage detected by the photodiode. This can be described by equation [3]; a change in thickness of the piezo crystal (Δt_{out}) is caused by an applied voltage (V_{IN}) multiplied by the piezoelectric charge constant, d_{ij}. This constant describes the amount of strain experienced by the crystal due to an applied electric field; the subscripts of this constant describe the axis of the crystal structure along which the electric field is being applied and the axis along which a response occurs (Taylor 1985; Ltd. 2002).

$$\Delta t_{out} = d_{ij} \cdot V_{IN} \quad [3]$$

In our experiments with the AFM, a feedback system is employed to quickly and accurately adjust the force applied on the sample and return it to the desired force value, corresponding to the setpoint voltage; in other modes of AFM, the setpoint may be coupled to amplitude or height instead of force. The error signal (difference between the detected voltage and the setpoint) is constantly minimized, resulting in continuous, and immediate adjustments (Reza Moheimani 2008). Often, a closed-loop feedback system is used. In this case, strain gauges are coupled to the piezo scanner and measure the actual change in the piezo height when there is a non-zero error signal. The strain gauge measurement is compared to the desired change in height and makes any corrections as necessary (for example due to hysteresis in piezo expansion). The speed and accuracy of the feedback adjustments can be controlled using gains. In our setup, the feedback loop is maintained by a Proportional- Integral (PI) control system (Figure 2.2). The P gain proportionately affects the drive signal to expand or contract the piezo, as it directly multiplies the error signal. However, in this case, the setpoint is often overshot due to hysteresis of the piezo. The I gain damps the response of the P gain by taking into account the changing discrepancy between the setpoint and current values. This has the overall effect of slowing the time taken to return to the setpoint, but largely eliminates the overshoot which occurs with a P gain used alone (Barr 2002). Ideally, the P and I gains should be maintained at as high a value as possible to

decrease the response time, but not so high that the piezo crystal begins to resonate. Thus, by using a feedback system, the force on the sample applied by the AFM tip can be maintained at a constant value throughout the course of an experiment.

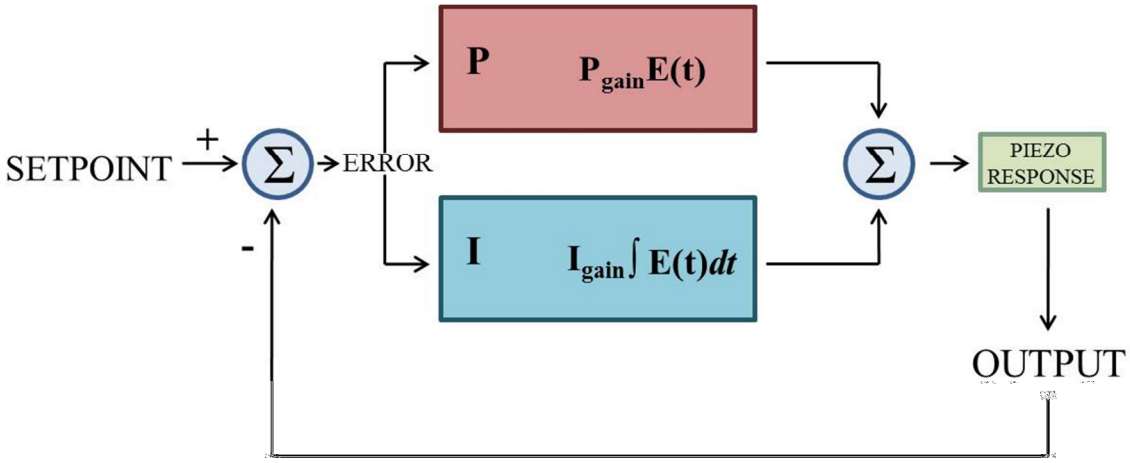

Figure 2.2: PI Feedback Control System. Here, it can be seen that the Error signal (E(t)) is derived from the difference between the output and setpoint values. This error signal is modulated by the Proportional and Integral gains (P_{gain} and I_{gain}). The sum of these two effects leads to a certain process, which, in the case of the AFM setup is expansion or contraction by the piezo. The output signal (i.e. force measured by the AFM after feedback has occurred) feeds back into the system, resulting in continuous adjustment until the error signal is zero.

2.1.2 Cantilever Calibration

Cantilevers are generally batch microfabricated from silicon or silicon-nitride (Zougagh and Rios 2009). As silicon-nitride is optically transparent, a reflective coating (such as gold or aluminum) is added to cantilevers which are made of this material in order for deflections to be properly detected.

As mentioned above, cantilevers can be treated as springs; thus, they can be used to measure the interaction forces and applied forces between the AFM tip and sample during experiments using equation [2]. For this equation to be used, the spring constant must be experimentally determined. Numerous methods have been developed for accurately determining the spring constant of cantilevers (Cleveland 1993; Sader 1995; Gibson 2001; Lévy 2002; Gibson, Weeks et al. 2003; Bonaccurso and Butt 2005; Golovko, Haschke et al. 2007). Spring constant values which are quoted by the manufacturer are determined

mathematically from the material properties of the cantilever. This mathematical method has been extensively characterized by Sader *et al.* (Sader 1995). The spring constant (k) for V-shaped cantilevers (as are used in this project) can be determined from either of the following two equations (Sader 1995; Sader 1995; Gibson, Weeks et al. 2003):

$$k = \frac{Et^3w}{2L^3}\left(\cos\theta\left[1 + \left(\frac{4w^3}{b^3}\right)(3\cos\theta - 2)\right]^{-1}\right) \quad [4]$$

$$k = n\rho At(2\pi \cdot 1.04\upsilon)^2 \quad [5]$$

Here, E is Young's Modulus, t is the thickness of the cantilever, w is the width of a cantilever arm, b is the total width of the cantilever base, L is the cantilever length, θ is the angle between cantilever arms, A is the surface area of the top face of the cantilever, ρ is the density, and υ is the resonant frequency in air. The multiplication by 1.04 is due to the effect of damping in air of V-shaped cantilevers, and n is a correction factor which depends on geometry and can be obtained from tables of values which have been previously calculated (Sader 1995). While these calculations take into account the change in Young's modulus, and thus the resonant frequency, of the cantilever due to the reflective coating, for layers less than about 100nm in thickness this change is not significant (Gibson, Weeks et al. 2003). Gibson *et al.* have published a simpler treatment of these equations, with an average density (ρ) of the cantilever of

$$\rho = \rho_1 + \frac{\rho_c t_c}{t} \quad [6]$$

Where ρ_1 is the density of the cantilever substrate (silicon or silicon nitride) and ρ_c and t_c are the density and thickness of the coating. Incorporating this expression into Eq. [5], and equating with Eq. [4], they provide one final, solvable equation in terms of only E, ρ_1 and t_c. For silicon cantilevers, Young's modulus and the density do not vary significantly, and the thickness of the coating generally falls between 10 and 50nm; a variance which will not adversely affect the accuracy of k as the value is so small (Gibson, Weeks et al. 2003). However, silicon nitride cantilevers have a much larger variation in E and ρ, and there is variation in geometrical parameters within cantilevers produced, even from the same batch. This increases the importance for determining spring constants experimentally.

Though many methods have been developed to accurately determine k, the thermal noise method (Hutter 1993; Lévy 2002) has been shown to be the most straightforward, once all sources of error have been accounted for. This method is the most commonly employed and was used to calibrate the cantilevers used in this thesis. The cantilever is modelled as a harmonic oscillator with one degree of freedom; this will fluctuate in response to thermal energy. The Hamiltonian (H) for such an oscillator is (Hutter 1993):

$$H = \frac{p^2}{2m} + \frac{1}{2} m {\omega_0}^2 x^2 \quad [7]$$

Where x is the displacement of the oscillator, m is its mass, p its momentum and ω_0 is the resonant frequency. According to the equipartition theorem (Hutter 1993), the average value of each quadratic term of this equation is equal to $\frac{1}{2}k_BT$, where k_B is the Boltzmann constant, and T the temperature:

$$\frac{1}{2} k_B T = \langle \frac{1}{2} m {\omega_0}^2 x^2 \rangle \quad [8]$$

Since the spring constant can be determined directly from the resonant frequency ($k = m\omega_0^2$), Eq. [8] can be rearranged to solve for k:

$$k = \frac{k_B T}{\langle x^2 \rangle} \quad [9]$$

Here, to eliminate sources of noise in the measurements, this average displacement is examined in the frequency domain, producing a power spectrum. In the frequency domain, it is easy to separate noise contributions from the peak corresponding to the resonant frequency. A Lorentzian curve is fit to the amplitude-frequency (A(f)) relationship (Eq. [10]) for the cantilever, modeled as a Simple Harmonic Oscillator. Here, A_{DC} is the D.C. Amplitude, η is the background noise, f_o is the resonant frequency of the cantilever, and Q the Quality factor.

$$A^2(f) = \eta^2 + A_{DC}^2 \left(\frac{f_o^4}{(f^2 - f_o^2)^2 + \frac{f_o^2 f^2}{Q^2}} \right) \quad [10]$$

The integral of the Lorentzian fit to the resonant frequency peak in the power spectrum, is equal to the mean square displacement of the cantilever in the time domain, $\langle x^2 \rangle$, allowing for a direct determination of the spring constant. Values obtained in this manner have been shown to correspond extremely well to values obtained mathematically (Hutter 1993; Lévy 2002).

2.1.3 Imaging Modes

The AFM may be operated in a number of imaging modes (Drake, Prater et al. 1989; Zhong 1993; Giessibl 1995; Giessibl 2003). While no topographical imaging was performed in this thesis, a description of the following techniques is included for completeness. There are three main modes in which the AFM can be used: Contact mode, Intermittent-Contact mode, and Non-Contact mode (Figure 2.3).

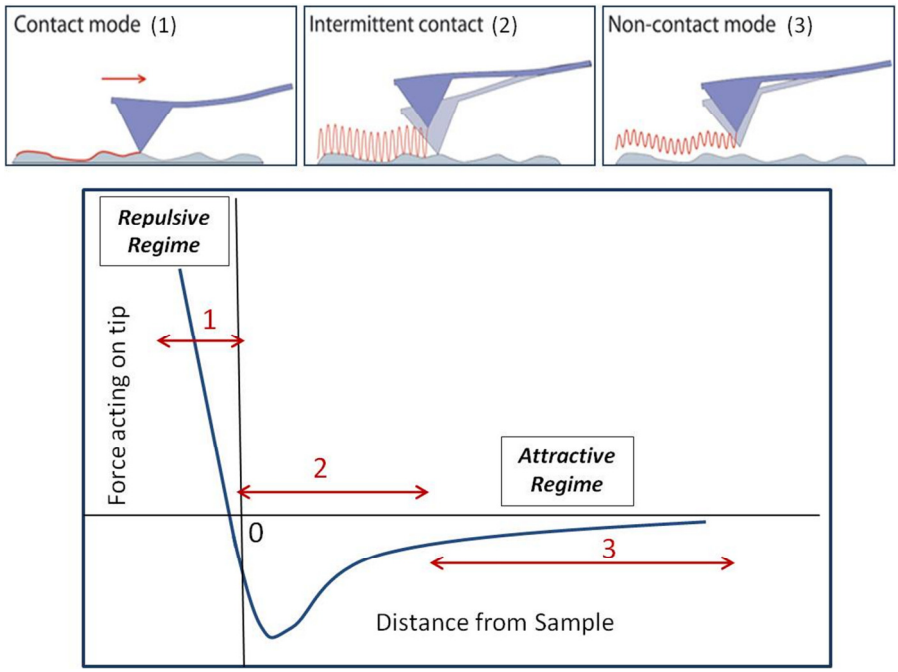

Figure 2.3: Imaging Modes of the AFM. Contact mode [1] is performed in the repulsive regime, where the tip is deflected away from the surface in response to topological features. Intermittent-Contact mode [2] is at the interface of attractive and repulsive regimes; oscillations can vary due to attractive forces or repulsive forces, depending on the height of the sample. Non-contact mode [3] lies fully in the attractive regime. In this case, long range forces, such as van der Waals forces, cause cantilever deflection and damp the oscillations. Top panels are reproduced with permission from the NanoWizard II user handbook produced by JPK Instruments (see Appendix B).

One major difference between these three imaging modes is the distance from the sample at which the tip is maintained. Contact mode ([1] in Fig. 2.3), where a stationary cantilever is in direct contact with the sample, exists in the repulsive regime. This means that the tip will be pushed away from the surface in response to changes in topography. The remaining two imaging modes are operated by driving the cantilever at or near its resonant frequency (Zhong 1993; Giessibl 1995). Intermittent Contact mode ([2] in Fig. 2.3) oscillates the tip at a distance just above the surface of the sample. This mode exists at the cross-roads of the attractive and repulsive regimes, and the tip will be both attracted to and repulsed from the surface as the topography changes. Non-contact mode ([3] in Fig 2.3) holds the tip firmly in the attractive regime; the tip is at a sufficient distance (>100nm) that the only forces that can be detected are attractive forces which are usually due to van der Waals interactions, or, in certain specific cases, other electrostatic forces such as covalent or hydrogen bond interactions or magnetic forces (Giessibl 2003).

The AFM is most often operated in Contact Mode. In this mode, there are two sub-divisions: constant force mode and constant height mode. In constant height mode, the cantilever scans the surface at the same height, regardless of changes in topography of the sample; this results in increased force in certain areas as the cantilever is deflected. In this mode a deflection map is created; rather than generating the topography of a sample, a deflection map demonstrates changes in topography. Flat areas of the sample will appear neutral, while deflections up and down will appear as bright and dark bands. This allows for fine features of a sample to be more clearly seen. In constant force mode, a feedback system (as described above) is used to maintain a setpoint force and the cantilever adjusts its height above the sample in order to maintain this force as the sample is scanned. In this case, the adjustments in piezo height are used to generate the topographical image. Further fine details of images can be obtained from the error signal which is measured by the feedback system; this vertical deflection map is created from the absolute deflections of the cantilever as it scans the surface, independent of the adjustments in piezo height. Some disadvantages to contact mode are the strong adhesion and lateral forces between the tip and sample (Zhong 1993), which can cause significant indentation on a softer sample, giving an artificial image of the surface topography, and potentially damaging the sample. Another important thing to

consider is the tip geometry; the sharper the tip, the more fine details can be observed, but greater damage will also be done to softer samples (Radmacher 2002).

To combat some of these disadvantages, Intermittent Contact Mode was developed (Zhong 1993). By oscillating the cantilever at its resonant frequency just above the surface of the sample, far less damage is done to both the tip and sample. Additionally, lateral forces are not as prevalent due to the decreased time of contact between tip and sample (Colton, Baselt et al. 1997). In this mode, as the tip reaches the surface of the sample, repulsive forces damp the oscillations, reducing the amplitude. If the AFM feedback circuit is set to maintain constant amplitude, the topography of the sample may be determined. In Non-Contact Mode, the tip is oscillated further above the surface of the sample, such that no direct contact ever occurs. Often, imaging is done in this mode with the feedback loop set to maintain a constant frequency of oscillation, allowing deflections of the cantilever in response to attractive long-range forces (Giessibl 1995; Giessibl 2003). Changes may be detected in the frequency, amplitude (due to damping), and phase of the oscillation. The phase change is detected in a shift between the driving frequency of the oscillation and that which is measured by the feedback system. These changes can provide many different kinds of information about the properties of the sample surface which can include, but are not limited to, chemical interactions (Noy 1995), and electrical (Fujihira 1999), mechanical (Radmacher, Cleveland et al. 1994), or thermal (Majumdar 1999) interactions.

2.1.4 Force Curves

The AFM has been shown to be a useful tool for imaging with nanometre precision both biological and non-biological samples. One of its other key attractions however, is its ability to apply a highly controlled force to a single location over a cell, for example. Instead of scanning the surface, after calibration to determine the spring constant, the cantilever may be approached to a surface to apply a highly localized and precise mechanical force. In addition, a “force curve” can also be measured if desired (Weisenhorn 1989; Butt 2005). Force curves are more accurately known as force-displacement curves. These curves demonstrate the applied force on the sample as the AFM tip approaches and retracts from the

sample (Fig. 2.4A). On a stiff sample, such as glass, the deflection of the cantilever (d(z)) is directly proportional to the height of the piezo above the sample, resulting in a linear relationship between piezo extension and cantilever deflection. On a soft substrate such as a cell, there is an indentation into the sample (Tao, Lindsay et al. 1992; Weisenhorn 1993; Radmacher, Fritz et al. 1995), which lowers the deflection measurement relative to that which would have been measured on a stiff sample with the piezo at the same height. Thus, the deflection corresponds to the height of the piezo (z) reduced by the indentation depth (δ). This is normalized by a value of z_0, which corresponds to the piezo height when the tip is just in contact with the sample surface.

$$d(z) = (z - z_0) - \delta \quad [11]$$

Using equation [11], it is possible to convert the force-distance curves into force-indentation curves. The force-indentation curves can be fit to the Hertz model to determine Young's Modulus of elasticity of the sample. This model was developed in the late nineteenth century from continuum mechanics, and extended by Sneddon (Hertz 1882; Sneddon 1965). The Hertz-Sneddon model is applicable for the indentation of an infinitely extended elastic surface by a simple shape (Fig 2.4B). Two of the shapes most often used are conical indenters and spherical or paraboloid indenters. The equations of force applied for each of these indenters are:

$$F_{cone} = \frac{2}{\pi}\frac{E}{(1-\upsilon^2)}\delta^2 \tan\alpha \quad [12]$$

$$F_{paraboloid} = \frac{4}{3}\frac{E}{(1-\upsilon^2)}\delta^{3/2}\sqrt{R} \quad [13]$$

Here, E is Young's Modulus of the sample being indented, v is the Poisson ratio, δ is the indentation depth as described above, α is the half opening angle of the conical indenter, and R is radius of curvature for a paraboloid, or the radius for a spherical indenter. The Poisson ratio, which describes the degree to which expansion occurs in a sample orthogonally from the direction a compressive force is applied, has a value of 0.5 for materials which are considered incompressible; that is, compression immediately leads to expansion elsewhere. Some exceptions to this value occur in softer materials such as rubber where the Poisson

ratio is smaller than 0.5; generally the values used for cells are in the range of 0.3-0.5, though the true value is unknown (Treloar 1975; Radmacher 1997).

To create the force-indentation curves, and thus to extract the Young's Modulus, it is necessary to determine the contact point z_0. On a stiff sample this can be easily determined as the force curve experiences a rapid change in slope at this point and z_0 can be found by inspection of the first and second derivatives of the force curve. On softer samples, this method does not always provide an accurate value for z_0. A method developed by Rotsch *et al.* (Rotsch, Jacobson et al. 1999), and used in these experiments, takes this into account. Here, two points along the force curve (known values of z and d) are used to fit with the Hertz model, extracting both z_0 and E. Once a reasonable contact point is known, the force-displacement curves are easily converted to force-indentation curves using Eq. [11].

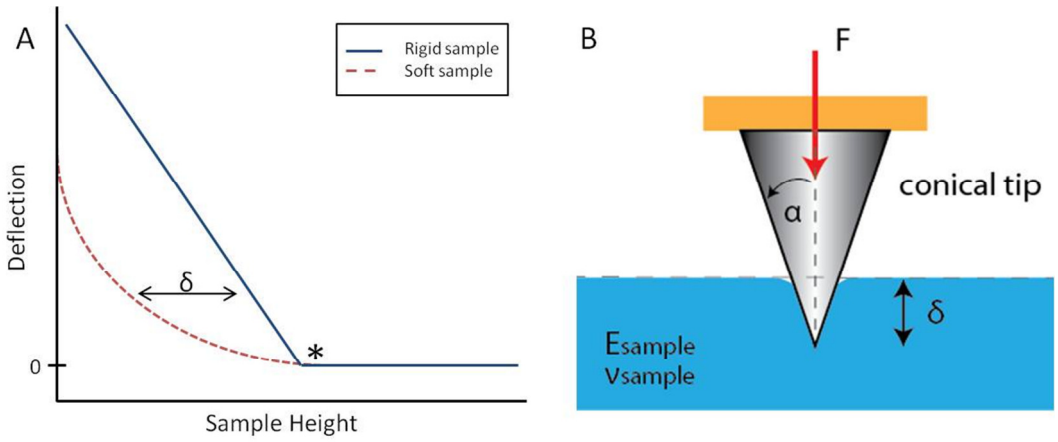

Figure 2.4 Force Curves and the Sneddon Model. Force curves taken on a rigid sample are much different from those on a soft sample (**A**). The point of contact (*) is easy to see on a rigid sample as there is an abrupt change in slope; on a soft sample however, this same point of contact is much more difficult to determine. The indentation depth (δ) is the difference between the deflections measured on a rigid vs. a soft sample. This corresponds to the indentation depth in (**B**) which demonstrates the Sneddon model for conical indentation of an elastic sample as described in Eq. [12].

2.1.5 Validity of AFM Force Techniques for use on Cells

While the Hertz model has been shown to be effective in measuring the elasticity via force curves taken with the AFM (Butt 2005), there are a few important considerations which must be noted. AFM tips used in the majority of experiments are pyramidal in shape, not a

cone or sphere as required by the Hertz model. It has been shown that a slight change in geometrical values is a sufficient correction: the opening angle α of 35° is equivalent to a conical angle of 38.3° (Radmacher 2002). It has also been determined that for large indentations, the conical equation matches the data very well, while for shallow indentations, smaller than the radius of curvature, the spherical equation matches (Radmacher, Fritz et al. 1995). It is also important to note that cells are neither purely elastic, nor homogeneous in nature, nor infinitely extended as assumed by the Hertz model (Radmacher 2002; Butt 2005). Further, for force curves which are measured on very thin substrates (less than 500nm), a typical indentation depth of 100-200nm is not sufficiently far from the underlying surface to prevent the AFM from detecting the rigid surface beneath. Elasticity measurements taken in these regions are likely to be abnormally high; the apparent Young's Modulus is being affected by the underlying surface (Radmacher 2002).

The speed at which the AFM tip is approached to the surface (loading rate) must also be taken into account. At higher speeds (in excess of ~25μm/s), the viscous properties of the cell become much more important, and will change the apparent elasticity measured (Butt 2005). As well, with a varying loading rate, the energy landscape of the tip-sample interaction changes.

There exists another type of imaging mode which consists of taking a force curve at each point over a surface generating an elasticity map. Known as "force-volume imaging", this technique demonstrates the change in Young's modulus across the surface instead of revealing the topography of the sample. There is some debate over the validity of this so-called "force-volume" imaging as it takes a significant amount of time to scan the entire area of interest on the surface of a cell- upwards of 20 minutes (Rotsch, Jacobson et al. 1999). In this length of time, much can change in the dynamics of a living cell, meaning the initial part of the image may not accurately represent the same cell as at the end of the image acquisition. Also, the Young's Modulus of a cell is not isotropic in depth, as it depends significantly on the organization of cellular components such as the cytoskeleton and the nucleus. This means that the value measured will depend on numerous factors, including the amount and rate of the force applied, the indentation depth of the tip, and tip geometry (Darling, Wilusz et al. 2010).

It is clear that the AFM is an extremely powerful tool for use in measuring the local mechanical properties of biological samples. The AFM has been used with great success in providing accurate, high resolution images of biological samples and helping to demonstrate chemical interactions occurring between biological samples. Perhaps more useful however, is its use as a tool for applying locally controlled forces to biological samples in order to investigate their mechanical response, as will be discussed in this thesis. Traditional applications of an AFM where the various modes are employed to generate topographical images of both hard and soft materials, have many factors which must be taken into account in order to accurately interpret the results. It is clear that the methods presented in this thesis reveal a reliable technique not often exploited in AFM experiments on biological samples. This technique becomes even more powerful when it is used in tandem with high-powered optical microscopy techniques such as Confocal Microscopy.

2.2 Confocal Microscopy

The confocal microscope is a variation on wide-field fluorescence microscopes which have been used primarily to image deep within biological samples at high resolution. In light microscopes, white light is used to image samples through differences in the index of refraction, variance in transmitted light, phase contrast, and many other techniques. Fluorescence microscopes in contrast, detect emitted light from the sample at specific frequencies. This light is often produced through the excitation of fluorophores by the use of lasers or UV lamps, causing the emission of photons of a specific wavelength (see section 2.2.2).

The concept of a confocal microscope was first patented in 1957 by Marvin Minsky of Artificial Intelligence fame (Murphy 2001). In the years following, many people worked together to develop a working model. The first scanning confocal microscope was built in the early 1970s, and the first images of cells originating from this device were published in 1973 (Davidovits 1972; Davidovits and Egger 1973). Advancements in computer and laser technology were quickly adapted for use in these microscopes, and the first commercially

available confocal microscopes were available in the late 1980s (Amos, White et al. 1987; White, Amos et al. 1987).

2.2.1 Schematic of a Confocal Microscope

The confocal microscope is unique in its ability to optically section an image volume, acquiring light from only one plane of the sample at a time, and thus eliminating the majority of out-of-focus light. In traditional forms of optical microscopy, when the objective is focused in one location to image a sample, the light that is used for imaging or excitation equally illuminates throughout the entire sample volume (Murphy 2001). With wide-field fluorescence and light microscopes, nearly all reflected or emitted light is collected in during imaging, resulting in a great deal of so called out-of-focus light, or, light obtained from parts of the sample which are not in focus. Conversely, the confocal microscope makes use of apertures (also known as pinholes) to eliminate out-of-focus light (described below). Confocal microscopes are designed such that the illumination, the sample, and the light detection system are all in focus with each other; that is "confocal". This is done such that all light emitted from above and below the image focal plane is blocked by the pinhole; only light originating from the focal plane will pass through the aperture (Fig 2.5A). A secondary pinhole may be used for focusing the illumination light.

Additionally, confocal microscopes image each point of an image plane sequentially, instead of simultaneously, reducing the time of exposure at each point and the amount of light that is needed for high quality imaging, and consequently reducing the amount of photobleaching. In most cases, a typical 'raster scanning' method is used; the point of light travels along each x-line in an x-y plane, quickly returning to the beginning of each line before imaging recommences. Other scanning mechanisms also exist (see section 2.2.3). Confocal microscopy has also been used in tandem with other forms of microscopy, especially with the AFM (see Chapter 1 for a full discussion), as for the experiments described in this thesis. This allows for high resolution imaging with the simultaneous application of local forces.

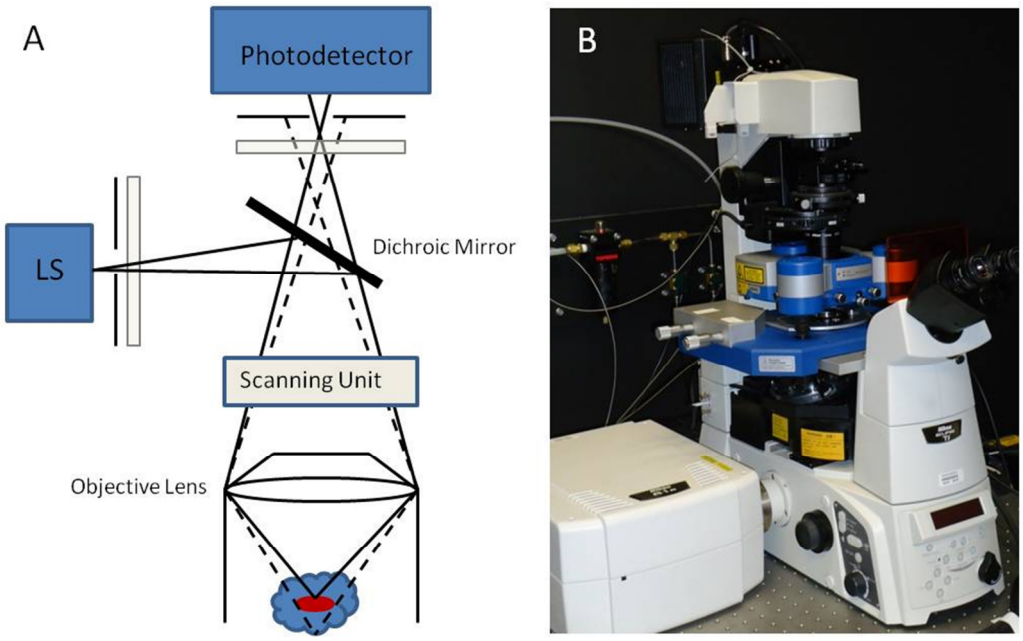

Figure 2.5: Schematics of Laser Scanning Confocal Microscope. In (**A**), the significance of the pinholes is demonstrated. Light is emitted from the light source (LS), usually a laser, passes through a filter to select for the desired wavelength, and encounters the dichroic mirror. This reflects the excitation wavelength down through the objective into the sample. Both the emitted light that is in focus (solid lines) and out of focus (dashed lines) travels back upwards through the objective, and passes through the dichroic mirror and a further selection filter. At this point, only the in focus light passes through the pinhole to reach the photodetector; the out of focus light is stopped. In (**B**) is seen our set up of a Nikon Inverted TiE optical microscope which is connected to a Nikon A1R resonant scanning confocal microscope. Also apparent is our AFM (in blue), a Nanowizard II from JPK Instruments.

2.2.2 Fluorescence Imaging and Photobleaching

Fluorescence describes the emission of light at a particular wavelength by a substance after having absorbed light or other type of electromagnetic radiation of a different wavelength, which is generally shorter than that which is emitted and therefore of higher energy. Fluorescence is based on the principle that upon absorption of a photon of wavelength λ, an electron is excited from its ground state (S_0) to an excited level (S_1); the difference between these energy levels is equal to the energy of the photon (E_p). This is described by the following formula, where h is Planck's constant and c is the speed of light:

$$E_p = \frac{hc}{\lambda} \quad [14]$$

After excitation, this electron must decay back to its ground state, though it may pass through a huge variety of different energy levels before achieving the ground state. The electron may relax, losing some of its energy from thermal radiation and vibrational energy, but most of the time, the majority of its energy is lost through emission of a second photon whose wavelength corresponds to the energy difference that remains between the excited and ground state (as in Eq. [14]). This is shown diagrammatically in Figure 2.6. Fluorescence imaging is achieved by exciting fluorophores in the sample using lasers (as in laser scanning confocal microscopy) or mercury and UV lamps (as in fluorescence microscopes).

It is possible for electrons to undergo a process called intersystem crossing while in the excited state, which changes its nature from an excited singlet state to an excited triplet state. The triplet state, while more stable energetically, is also more chemically reactive. Thus, over time, as more electrons pass through this pathway, the likelihood of chemical reactions occurring which permanently damage the fluorophore increases. This will dim the amount of fluorescence emission over time, a process known as photobleaching (Murphy 2001).

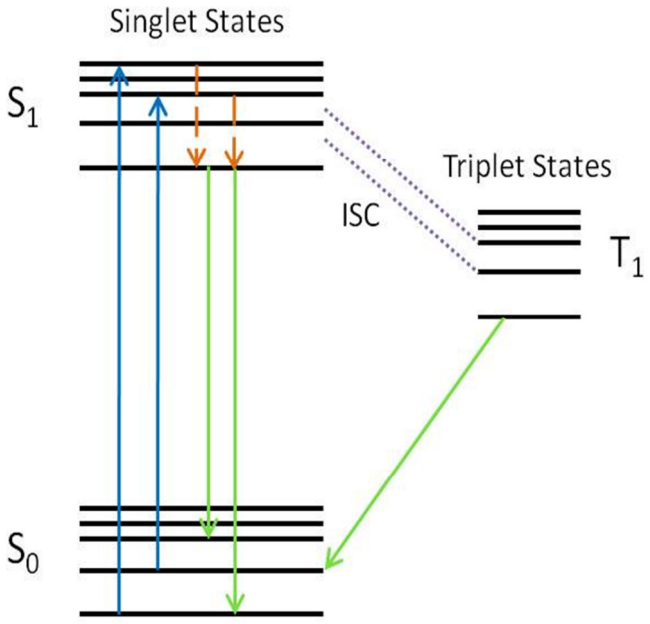

Figure 2.6: Fluorescence and Photobleaching Diagram. Electrons are excited from their ground state (S_0) to an excited state (S_1). Once there, relaxation occurs, resulting in energy loss through vibrations and heat. Photons of a new wavelength are then emitted as the electron falls back to the ground state. Prior to emission, electrons may also go through conversion to the more stable triplet state. In photobleaching, over-stimulation extends the lifetime of the excited state, promoting transitions to the triplet state where, due to its increased stability, chemical reactions may occur which extinguish the fluorophore. Alternatively, photons exhibit delayed fluorescence, which is known as phosphorescence.

Ideally, the degree of photobleaching is minimized, especially for long-term imaging, as it lowers the quality of the image acquired. However, this phenomenon has also been exploited in a number of useful techniques, such as Fluorescence Recovery After

Photobleaching (FRAP) (Axelrod, Ravdin et al. 1976; Soumpasis 1983), and Fluorescence Loss in Photobleaching (FLIP) (Cole, Smith et al. 1996; Nehls, Snapp et al. 2000; Phair and Misteli 2001). FRAP involves watching the recovery of fluorescence in an area that has been bleached, while FLIP investigates the loss of fluorescence throughout a cell as a small area is repeatedly bleached. Both of these techniques have been extensively used to investigate protein dynamics within a cell (Axelrod, Ravdin et al. 1976; Cole, Smith et al. 1996; Swaminathan, Hoang et al. 1997; Dayel, Hom et al. 1999; Nehls, Snapp et al. 2000; Lippincott-Schwartz, Snapp et al. 2001; Phair and Misteli 2001; Lippincott-Schwartz, Altan-Bonnet et al. 2003; Lippincott-Schwartz and Patterson 2003). Specifically, it is possible to extract information about the diffusion constant of a protein (tagged with a fluorophore) within a cell. If this constant is found to be lower or higher than expected, this can in turn provide information as to the nature of the motion. If the protein is being actively transported through the cell, the motion will be faster than through pure diffusion. If it is in complex with other proteins, it will be slowed either by being more massive or through collisions with other cellular components such as the cytoskeleton (Lippincott-Schwartz, Altan-Bonnet et al. 2003). Similarly, the mobile fraction of a protein distributed throughout the cell may be determined by measuring the levels of fluorescence in various areas of the cell (Lippincott-Schwartz and Patterson 2003).

In the experiments presented in this thesis, photobleaching will be used to selectively blank out sections of actin stress fibres by overstimulation with a laser in specified areas. These results will be discussed in detail in Chapter 5.

2.2.3 Advantages to Confocal Microscopy

The confocal microscope offers many advantages over other types of optical microscopes. Transmission electron microscopes, while offering nanometre resolution, are not useful for live biological imaging or imaging in native biological environments, as they require extensive sample preparation, including fixation. Conventional light and fluorescence microscopes allow us to image living cells in their native environment; however the fine details of structures cannot be resolved past the diffraction limit. The limit of diffraction

defines a radius at which two points of illumination are resolvable for a given microscope objective (Eq. [15]) (Spring 2009).

$$d = \frac{0.61\lambda}{n \sin\theta} \quad [15]$$

Here, d is the distance at which two points are resolvable, λ is the wavelength of the light used to image with, n is the refractive index of the objective, and θ is half the angle at which light beams converge from the objective to image the source. The denominator of this equation, $n \sin\theta$, is also known as the Numeral Aperture (NA) of the lens. A typical value for the NA of a lens ranges from 1.0-1.4, depending on whether the lens is used in air (n= 1.00), in water (n=1.33), or oil (n= 1.51). As a typical light source used is 400-500nm in wavelength, this means that the diffraction limit is approximately 200nm for a conventional microscope, which is much larger than the distance between most structures within a cell.

The origin of the factor of 0.61 in Eq. [15] comes from the Rayleigh criterion which states that for two Airy disks to be resolvable, the first minimum of one adjacent point-spread function must coincide with the peak of the other point-spread function (Spring 2009). The advantage of using a confocal microscope is that, due to the unique pinhole design, the Airy disks are much thinner, and the distance required to resolve them is smaller. This means that the resolution equation becomes closer to Eq. [16] for lateral resolution (d_{lat}). While the resolution is still highly dependent on the wavelength and numerical aperture, and there is still a physical limit (diffraction), the same degree of contrast can be achieved with a confocal microscopy at a smaller separation distance with comparable wavelength and lenses as in wide-field fluorescence microscopy.

$$d_{lat} = \frac{0.41\lambda}{NA} \quad [16]$$

Similarly, the axial resolution (along the z-axis) of a confocal microscope is improved over that of a wide-field fluorescence microscope. This is due to the tightening of the Airy disks in the axial direction as described above. Here, the axial resolution (d_{axial}) is dependent on the refractive index of the specimen medium (n_{med}), the wavelength (λ), and the square of the numerical aperture (NA).

$$d_{axial} = \frac{1.4\lambda \cdot n_{med}}{NA^2} \quad [17]$$

While this improvement in axial resolution is not dramatic on its own, Confocal microscopy is primarily distinguished by its ability to perform optical sectioning, whereby light is gathered for an image from only one plane of a sample volume at a time (Murphy 2001). This technique significantly improves axial resolution compared to wide-field fluorescence microscopy as light is only collected from one plane at time and the out-of-focus light above and below this plane are eliminated by the pinhole apparatus.

2.2.4 Variations and Improvements to Confocal Microscopy

One of the first confocal microscopes built was the spinning-disk microscope (Egger 1967). Perhaps not as popular as conventional confocal microscopy, it nevertheless is useful for rapid imaging processes. The 'spinning-disk' in question is a Nipkow disk which contains a pattern of pinholes. The sample is thus "raster-scanned" by spinning the disk; multiple points are imaged simultaneously as light passes through each pinhole, but these pinholes are rapidly moved away from where they originally were (Ichihara 1996). This greatly increases the rate at which images can be obtained (up to 1000 frames/sec) and also reduces the light exposure, which reduces the level of photobleaching. This is particularly useful for tissues that are easily damaged and for observing fast dynamics at video rate (Nakano 2002).

Recently, traditional laser-scanning confocal microscopes have been adapted to image at video rate as well; this has become known as imaging in Resonant Mode (Sanderson and Parker 2003; Borlinghaus 2006). Instead of using servo controlled galvanometer mirrors to raster scan the surface (Galvano mode), the mirrors are mounted on piezo scanning galvanometers. These vibrate at a fixed frequency, moving the mirror in a rotational sinusoid (Larson 2010). This increases the image acquisition rate (of full frame images, 512x512 pixels) from about 4 frames/sec for typical Galvano mode to upwards of 30 frames/sec in Resonant Mode (Larson 2010). There is some loss in resolution in this mode, due mainly to a decrease in the signal to noise ratio. This decrease is inevitable due to a

decrease in imaging time at each pixel, resulting in a lower amount of actual signal intensity collected; however, this can be accommodated for with some loss in frame rate.

2.3 Cell Techniques

2.3.1 Green Fluorescent Protein

The Green Fluorescent Protein (GFP) was originally isolated from the jellyfish, *Aequorea victoria* in 1991 (Prasher, Eckenrode et al. 1992). In this jellyfish, GFP is largely responsible for the green lining on the inside of the otherwise translucent jellyfish. Fluorescence in jellyfish is produced from an energy transfer following the binding of calcium to a secondary bioluminescent protein, aequorin, which produces blue light (Prasher 1995; Misteli and Spector 1997). Because of its unique, independent manner of light generation, the structure and nature of GFP was quickly characterized and it was discovered that GFP may also be activated directly by an external ultra-violet (UV) light source (Chalfie, Tu et al. 1994; Prasher 1995). Characterization of the crystal structure and sequence of GFP led to the generation of numerous unique genetic modifications which further enhanced the usefulness of GFP for its use in molecular biology. Some of these include a modification which brightens the green signal emitted from GFP, known as enhanced GFP (EGFP) (Cormack, Valdivia et al. 1996), and modifications which shift the fluorescence from green light to any number of other wavelengths including blue, red, and yellow (especially those which coincide with readily available laser wavelengths) (Heim and Tsien 1996). There were also modifications to 'humanize' the genetic material so that it is easily expressed in human cell lines (Zolotukhin, Potter et al. 1996). Humanization, in this case, involved replacing numerous codons in the original jellyfish DNA with codons which are more commonly found in human DNA. Codons are sets of three nucleotide base pairs which code for amino acids; however, a single amino acid may have multiple codons whose sequence prompts the formation of the same amino acid. Thus, the humanized codons result in the same amino acids as are found in jellyfish.

The discovery of GFP and the development of its applications led to the bestowing of the 2008 Nobel Prize in Chemistry to Osamu Shimomura, Martin Chalfie, and Roger Y. Tsien. The prize was awarded for three key areas: Its initial discovery as an independent emitter of green light in jellyfish, the increased understanding of the method of fluorescence and subsequent modifications to the protein such that it emits different colours, and its value as a visible genetic tag for use in directly visualizing the localization and dynamics of proteins within biological systems (Nobelprize.org 2008). This technique of genetic tagging is well-known in molecular biology. It involves the development of fusion (or, chimeric) proteins which has the GFP directly attached to each protein of interest. The mechanism by which this occurs is more clearly outlined in the following section.

2.3.2 Transfection Techniques

Now a well characterized technique (Watt, Sawicki et al. 1993; Felgner, Tsai et al. 1995; Bonetta 2005; Glover, Lipps et al. 2005), transfection is the process by which foreign genetic material is introduced to a eukaryotic cell. While it is remarkably easy to genetically modify cells and cause them to express proteins of interest once DNA has been introduced to a cell, the biggest hurdle is how to get the DNA through the cell membrane while maintaining cell integrity. Initially, transfection was performed using a chemical perforation technique; cells became temporarily permeable following incubation with calcium phosphate ions (Bonetta 2005). It was quickly established that viruses could also be used to introduce genetic material; by replacing their own DNA with the DNA of interest, the virus uses all of the mechanisms already in place to inject the DNA directly into the cell (Graham and van der Eb 1973; Graham and van der Eb 1973). In the last forty years, numerous other techniques have been developed: using carrier molecules, such as liposome-based methods, positively-charged organic molecules, and other nanoparticles, or sonication and electroporation, which directly induce holes into the cell membrane (Potter 2001; Bonetta 2005; Han, Ghosh et al. 2007).

In our experiments, a liposomal technique was used. Plasmid DNA containing the protein of interest among other genes (Figure 2.7) was amplified within *E. coli* cells. Bacteria are used for this amplification as they easily replicate plasmid DNA as well as their own

DNA, and multiply at a very fast rate. After amplification, the DNA is isolated, quantified, and used for transfection. The liposome-based technique involves incubating the plasmid DNA with a solution of cationic lipids which accumulate around the negatively charged DNA, forming complexes of lipid/DNA (Lin, Slack et al. 2000). These liposomes are then placed in a dish with the cells of interest and, through endocytosis, the DNA enters the cytoplasm of the cell.

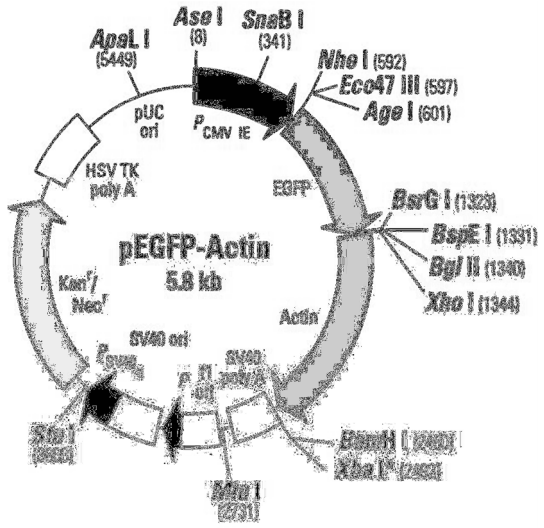

Figure 2.7: Actin-eGFP plasmid. This Clontech plasmid, received with gratitude from G. Charras (Charras, Hu et al. 2006), contains a number of genes of interest. Primarily, there is genetic material for EGFP, fused with that of actin (dark grey arrows). Also important is the Kanamycin/Neomycin resistance gene (light grey arrow) which allows for selection of *E. coli* cells that contain plasmids. The bolded abbreviations around the outside indicate restriction digest sites where the plasmid can be cleaved and added to or inserted into a larger section of DNA. Various origins of replication (black arrow sections) ensure that the proper genes are transcribed in the right situations (i.e. actin-EGFP within mammalian cells, kanamycin resistance in *E. coli*.) There is also a section which allows for selection by antibiotics to create a stable transfection. Image and information taken from the pEGFP-Actin Vector information sheet (clontech.com 2002).

Generally, transfections are considered transient, as the DNA or RNA is not incorporated into the genome of the cell of interest. This means that the expression of the protein of interest disappears with time as the cell destroys the foreign DNA or it is diluted following mitosis. It is possible to develop a cell line which is stably transfected however. This is done by selecting for cells which retain antibiotic resistance (or some other selectable gene) which is coded for within the plasmid DNA (see a visual representation of the genes of this plasmid in Fig. 2.7). Cells which express the antibiotic resistance will have incorporated the plasmid DNA into their genome. By using this selection pressure, a stable line of cells expressing the transfected fusion protein can be created (Glover, Lipps et al. 2005). The combination of cloning technology, where chimeric proteins of GFP fused to a protein of interest are produced, with simple methods of transient transfection have revolutionized the

field of cell biology, allowing cellular structures and the dynamics of sub-cellular components to be viewed quickly, and easily

2.4 Mechanical Models of the Cell

In the last two decades, the large influx of experimentation in the field of cellular mechanics has led to a plethora of models which attempt to explain the mechanical structure of the cell and its response to force (Lim, Zhou et al. 2006; Hoffman and Crocker 2009). However, there is a lack of consensus in the models that have emerged which attempt to explain all the observed phenomena. This discrepancy is due mainly to the variety of techniques, type and amount of force applied, and cell types and environments which have been investigated (Lim, Zhou et al. 2006). Additionally, depending on the model used, mechanical parameters such as stiffness were often reported to be orders of magnitude different from each other (Hoffman and Crocker 2009). In general, models that have been used fall into three main categories: the cell is either treated as a continuum, composed of discrete, solid, structures, or a mixture of both (Lim, Zhou et al. 2006; Hoffman and Crocker 2009).

Continuum models have generally had great success in describing the response of the whole cell to a force, especially in micropipette aspiration experiments, in which an entire cell is drawn up into the tube of a micropipette using a pressure differential (Lim, Zhou et al. 2006). In general, continuum models treat cells as being comprised of materials that possess continuum properties, such as Newtonian liquids, or viscoelastic solids. A material is considered to be continuous if the properties of the material as a whole apply to each subdivision, independent of the number of divisions. There are many variations within continuum models, though they are generally divided into two categories: liquid-drop models and solid models (Lim, Zhou et al. 2006). In the liquid models, cells are described as being comprised of a cortical shell under tension and some form of liquid interior; while in the solid model, cells are treated as being one type of material throughout the volume of the cell. Biphasic models also exist in which the cell switches between liquid and solid states, depending on signals from the environment. In the Gel-Sol Hypothesis, Janmey *et al.*

(Janmey, Hvidt et al. 1990; Janmey, Euteneuer et al. 1991) propose that the mechanical properties of cells are based on the constant dynamic polymerization and depolymerization of the actin (in particular) cytoskeleton. At rest, cells exhibit an elastic nature consistent with a highly cross-linked cytoskeleton composed of long filaments of actin and other filamentous biopolymers. This is known as the Gel (solid) state. However, in order to move, divide, or perform phagocytosis, a cell must become much more 'liquid', known as the Sol state. This occurs by the reversible depolymerization and dissolution of the cross-linking within the cytoskeleton. Extending this, under any situation of stress or strain, a cell will undergo remodelling of its cytoskeleton to become more flexible. While the continuum models have predicted accurately the mechanical deformation of cells in some cases, their main failure is the inability to account for the complexities of structure and interaction that exist within a cell and the dynamical changes in forces within a cell which occur in mechanotransduction (Lim, Zhou et al. 2006; Hoffman and Crocker 2009).

Models composed of discrete micro or nano-structural elements have generally been employed to take this complex structural nature of the cell into account. These models rely primarily on the cytoskeleton as being the main structural component of the cell and model the response of this polymer network to force. One of the most popular of these discrete network models, first applied to cellular systems by Ingber *et al.* (Ingber, Dike et al. 1994; Ingber 1997), is that of Tensegrity. Tensegrity is an architectural concept coined by R. Buckminster Fuller in 1961 (Fuller 1961) as a contraction of the term ‘tensional integrity’. Tensegrity is based on the principle that it is possible to build a mechanically stable structure in which there are compression resistant struts connected in a state of constant tension, independent of gravity. This is in contrast to the more standard method of force distribution in architecture using continuous compression and shear forces which would collapse without the constant force of gravity. This model naturally incorporates a state of 'pre-stress' into its components. Applied to a cell, the tensegrity model states that the actin cytoskeleton is under a constant tension (pre-stress) even when no force is applied to the cell. Balancing this, the microtubules and focal adhesions act as the compression resistant structures giving shape to the cell. Though this model succeeds in explaining many aspects of cellular mechanics, such as the retraction of severed actin stress fibres (Colombelli, Besser et al. 2009), it is a macroscopic model and does not take into account thermal fluctuations nor does it fully

explain mechanical properties in the region of the nucleus (Hoffman and Crocker 2009). As well, the mathematical basis for tensegrity has not been well developed. This has led to an easily accessible 'picture-based' model which, though theoretically attractive, does little to provide quantifiable predictions. This is likely due to the fact that tensegrity uses a grossly oversimplified treatment of the cytoskeleton, with discrete, relatively static elements; this is contrary to reality, where the cytoskeleton is highly cross-linked and dynamically rearranging in an active manner (Even-Ram, Doyle et al. 2007).

Though perhaps more accurate in general than continuum models, discrete models are still significant simplifications on the complexity of a living cell. There have been models proposed which combine elements of both continuum and discrete models. One such involves a dynamic cytoskeleton whose remodelling is largely dependent on the unfolding of cross-links rather than their unbinding (DiDonna 2007; Hoffman 2007). As in the Gel-Sol Model, this is based on a dynamically remodelling cytoskeleton, but is also valid only with an incorporated pre-stress, consistent with a tensegrity model. This model is interesting because, depending on the type of stress applied to the system, different responses are observed, which has clearly been shown to occur experimentally within cells (Hoffman and Crocker 2009).

Another popular model is based on the theory of Soft Glassy Rheology (SGR) which has classically been used to describe soft glassy materials such as liquid emulsions, colloids, pastes, slurries, and gels. Soft glassy materials are defined by a set of common characteristics (Mandadapu, Govindjee et al. 2008) which include being very soft (mechanical moduli in the range of Pa to kPa) and having material properties which are temperature and stress dependent, as well as evolving with time. Soft glassy materials are composed of numerous discrete elements which are unable to move with enough freedom to equilibrate thermodynamically, but are still undergoing constant rearrangements. Applied to a cell, this would indicate that the cell is composed of many discrete elements (which is true) and is bound together through numerous interactions (often postulated as attractive and repulsive bond interactions, and other 'energy traps') between neighbouring elements. Fabry *et al* developed a model which showed that cells exhibited properties that were consistent with SGR (Fabry, Maksym et al. 2001). In this model, stress relaxation within the cell is mediated

by a redistribution of its molecular components in an energy-dependant manner (Sollich 1998). It has been postulated that these energy-dependant processes include ATP-driven actin polymerization and myosin activity. One of the key features of this theory is that fluctuations in energy are constantly occurring, and thus are considered non-equilibrium conditions. For cells to be consistent with the SGR description, these adjustments must be small, implying that the cell is at a state that is very close to equilibrium (Mandadapu, Govindjee et al. 2008). However, considering that cells are living, dynamic systems full of energy-driven processes, they are likely very far from equilibrium. There is an ongoing debate on the applicability of describing cells as soft-glassy materials.

2.5 Importance of Studying Cellular Mechanics

The response of cells to force can largely be categorized into two divisions. First, the cell generates a mechanical response which is usually characterized by a deformation of the primary architectural elements within the cell, such as the cytoskeleton (Janmey and Weitz 2004; Kasza, Rowat et al. 2007). Secondly, a biological response is apparent which can be seen as a change in the levels of expression of genes (Chen, Mrksich et al. 1997), or in other biological processes (Geiger and Bershadsky 2002; Brooks, Lelkes et al. 2004; Chien 2007). This directly indicates the importance of understanding mechanotransduction when one begins to look at the depth and breadth of the influence force has on these biological processes. As early as the embryonic stage, cells experience force in the body, dictating developmental pathways. Indeed, changes in structural integrity, organization, and the mechanical environment have been shown to play a significant role in regulating growth (Chen, Mrksich et al. 1997; Georges, Miller et al. 2006), stem cell differentiation (McBeath, Pirone et al. 2004; Engler, Sen et al. 2006; Engler, Carag-Krieger et al. 2008), cell migration (Masuda and Fujiwara 1993; Lo, Wang et al. 2000), apoptosis (Schwartz and Ginsberg 2002; Jaalouk and Lammerding 2009), and even regulating disease states of cells such as in cancer (Ingber 2003; Paszek, Zahir et al. 2005; Hahn and Schwartz 2008). As a further example, consider the effect of the parasite which causes malaria in humans. This parasite attacks red blood cells, causing significant changes in its structure and molecular biology (Cooke, Mohandas et al. 2001; Bannister and Mitchell 2003). Red blood cells deform significantly as

they pass through tiny capillaries, exchanging oxygen with the surrounding tissues. The mechanical changes to the cells affected by malaria lead to a stiffening of the red blood cell membrane (Glenister, Coppel et al. 2002; Suresh, Spatz et al. 2005; Lim, Zhou et al. 2006); the cells are no longer able to deform as before, which leads to impaired blood flow, and can result in coma or death (Lim, Zhou et al. 2006).

To properly understand the influence mechanical force has on a cell's biological response, and perhaps more importantly, to learn to manipulate them to control differentiation or isolate diseased cells, a thorough understanding of the mechanical response is necessary. The primary questions then become, how does force propagate from the external environment throughout the cell? How can a mechanical signal in a specific location effect a specific biochemical response within the cell? It is clear that determining the exact pathway of mechanotransduction, which has yet to be elucidated, would be a significant achievement, and would likely lead to far more accurate models of the mechanical nature of the cell. As the cytoskeleton (especially that of actin) has been shown to play a major role in the initial mechanical response to force (Fletcher and Mullins 2010), understanding the connections between an applied force and the specific response of the individual cytoskeletal elements and its connection to the environment appears to be a logical starting point.

For these reasons, we chose to investigate the specific response of the actin cytoskeleton to a locally applied force over time. The time frame that was chosen however is significantly shorter than in most previous experiments mentioned in Chapter 1. This is because the initial, fast dynamic response of the cytoskeleton to force has, to the best of our knowledge, yet to be qualitatively or quantitatively determined. These experiments have been made possible due to recent advances in microscopy techniques, such as the resonant mode of confocal microscopy which allows us to image at very fast rates, and AFM which allows us to apply a highly controlled, local force to the surface of a cell. This, in tandem with the use of fluorescent tags to image specific structures within a living cell, has allowed us to image directly, in real time, the fast dynamics of a cellular response to a force applied by the AFM. By determining the effect of this applied force on a specific subset of cells (adherent 3T3 fibroblast cells which contain visible actin-EGFP stress fibres) under differing conditions (i.e. with anti-cytoskeletal drugs) we will be able to demonstrate the role that

specific components of the cytoskeleton play in the response to force. We will also demonstrate that the nature of this response is constantly evolving, and is not isotropic in nature. Further, the use of photobleaching will allow us to demonstrate the nature of strain dynamics along actin stress fibres in response to an applied force. To the best of our knowledge, no investigations directly quantifying the level of strain through the actin stress fibres have ever been achieved. We believe that the strain dynamics observed directly implicate the up-regulation of myosin II and actomyosin contractility within actin stress fibres in response to applied force. These results present a significant contribution towards the field of cellular mechanics, and help to elucidate the as yet undetermined pathway of mechanotransduction.

2.6 References

Amos, W. B., J. G. White, et al. (1987). "Use of confocal imaging in the study of biological structures." Appl Opt **26**(16): 3239-43.

Axelrod, D., P. Ravdin, et al. (1976). "Lateral motion of fluorescently labeled acetylcholine receptors in membranes of developing muscle fibers." Proc Natl Acad Sci U S A **73**(12): 4594-8.

Bannister, L. and G. Mitchell (2003). "The ins, outs and roundabouts of malaria." Trends Parasitol **19**(5): 209-13.

Baro, A. M., R. Miranda, et al. (1985). "Determination of surface topography of biological specimens at high resolution by scanning tunnelling microscopy." Nature **315**(6016): 253-4.

Barr, M. (2002). Closed Loop Control. Embedded Systems Programming**:** 55-56.

Barris, B., U. Knipping, et al. (1988). "Images of DNA fragments in an aqueous environment by scanning tunneling microscopy." Biopolymers **27**(10): 1691-6.

Binnig, G., K. H. Frank, et al. (1985). "Tunneling spectroscopy and inverse photoemission: Image and field states." Phys Rev Lett **55**(9): 991-994.

Binnig, G., H. Rohrer, Ch. Gerber, E. Weibel (1982). "Surface Studies by Scanning Tunneling Microscopy." Phys Rev Lett **49**(1): 57-61.

Binnig, G., C. F. Quate, et al. (1986). "Atomic force microscope." Phys Rev Lett **56**(9): 930-933.

Bonaccurso, E. and H. J. Butt (2005). "Microdrops on atomic force microscope cantilevers: evaporation of water and spring constant calibration." J Phys Chem B **109**(1): 253-63.

Bonetta, L. (2005). "The Inside Scoop- Evaluating Gene Delivery Methods." Nat Methods **2**(11): 875-883.

Borlinghaus, R. T. (2006). "MRT letter: high speed scanning has the potential to increase fluorescence yield and to reduce photobleaching." Microsc Res Tech **69**(9): 689-92.

Brooks, A. R., P. I. Lelkes, et al. (2004). "Gene expression profiling of vascular endothelial cells exposed to fluid mechanical forces: relevance for focal susceptibility to atherosclerosis." Endothelium **11**(1): 45-57.

Butt, H.-J., B. Cappella, M. Kappl (2005). "Force measurements with the atomic force microscope: Technique, interpretation and applications." Surf Sci Rep **59**: 1-152.
Chalfie, M., Y. Tu, et al. (1994). "Green fluorescent protein as a marker for gene expression." Science **263**(5148): 802-5.
Charras, G. T., C. K. Hu, et al. (2006). "Reassembly of contractile actin cortex in cell blebs." J Cell Biol **175**(3): 477-90.
Chen, C. S., M. Mrksich, et al. (1997). "Geometric control of cell life and death." Science **276**(5317): 1425-8.
Chien, S. (2007). "Mechanotransduction and endothelial cell homeostasis: the wisdom of the cell." Am J Physiol Heart Circ Physiol **292**(3): H1209-24.
Cleveland, J. P., S. Manne, D. Bocek, P.K. Hansma (1993). "A nondestructive method for determining the spring constant of cantilevers for scanning force microscopy." Rev. Sci. Instrum. **64**.
Cole, N. B., C. L. Smith, et al. (1996). "Diffusional mobility of Golgi proteins in membranes of living cells." Science **273**(5276): 797-801.
Colombelli, J., A. Besser, et al. (2009). "Mechanosensing in actin stress fibers revealed by a close correlation between force and protein localization." J Cell Sci **122**(Pt 10): 1665-79.
Cooke, B. M., N. Mohandas, et al. (2001). "The malaria-infected red blood cell: structural and functional changes." Adv Parasitol **50**: 1-86.
Cormack, B. P., R. H. Valdivia, et al. (1996). "FACS-optimized mutants of the green fluorescent protein (GFP)." Gene **173**(1 Spec No): 33-8.
Curie, J., P. Curie (1880). "Development par pression de l'électricité polarisé dans les crystaux hemidries et fares inclinés " Comp Rend. **91**: 294-297.
Darling, E. M., R. E. Wilusz, et al. (2010). "Spatial mapping of the biomechanical properties of the pericellular matrix of articular cartilage measured in situ via atomic force microscopy." Biophys J **98**(12): 2848-56.
Davidovits, P. and M. D. Egger (1973). "Photomicrography of corneal endothelial cells in vivo." Nature **244**(5415): 366-7.
Davidovits, P., Egger, M.D. (1972). Scanning Optical Microscope. United States. **3643015**.
Dayel, M. J., E. F. Hom, et al. (1999). "Diffusion of green fluorescent protein in the aqueous-phase lumen of endoplasmic reticulum." Biophys J **76**(5): 2843-51.
DiDonna, B. A., A.J. Levine (2007). "Unfolding cross-linkers as rheology regulators in F-actin networks." Phys Rev E Stat. Nonlinear Soft Matter Phys **75**.
Drake, B., C. B. Prater, et al. (1989). "Imaging crystals, polymers, and processes in water with the atomic force microscope." Science **243**(4898): 1586-9.
Egger, M. D., M. Petran (1967). "New reflected light microscope for viewing unstained brain and ganglion cells." Science **157**: 305-307.
Engler, A. J., C. Carag-Krieger, et al. (2008). "Embryonic cardiomyocytes beat best on a matrix with heart-like elasticity: scar-like rigidity inhibits beating." J Cell Sci **121**(Pt 22): 3794-802.
Engler, A. J., S. Sen, et al. (2006). "Matrix elasticity directs stem cell lineage specification." Cell **126**(4): 677-89.
Fabry, B., G. N. Maksym, et al. (2001). "Scaling the microrheology of living cells." Phys Rev Lett **87**(14): 148102.
Felgner, P. L., Y. J. Tsai, et al. (1995). "Improved cationic lipid formulations for in vivo gene therapy." Ann N Y Acad Sci **772**: 126-39.

Fletcher, D. A. and R. D. Mullins (2010). "Cell mechanics and the cytoskeleton." Nature **463**(7280): 485-92.
Fujihira, M. (1999). "Kelvin Probe Force Microscopy of Molecular Surfaces." Annu Rev Mater Sci **29**: 353-380.
Fuller, B. (1961). "Tensegrity." Portfolio Artnews Annual **4**: 112-127.
Geiger, B. and A. Bershadsky (2002). "Exploring the neighborhood: adhesion-coupled cell mechanosensors." Cell **110**(2): 139-42.
Georges, P. C., W. J. Miller, et al. (2006). "Matrices with compliance comparable to that of brain tissue select neuronal over glial growth in mixed cortical cultures." Biophys J **90**(8): 3012-8.
Gibson, C. T., B.L. Weeks, J.R.I. Lee, C. Abell, T. Rayment (2001). "A nondestructive technique for determining the spring constant of atomic force microscope cantilevers." Rev. Sci. Instrum. **72**.
Gibson, C. T., B. L. Weeks, et al. (2003). "Calibration of AFM cantilever spring constants." Ultramicroscopy **97**(1-4): 113-8.
Giessibl, F. J. (1995). "Atomic resolution of the silicon (111)-(7x7) surface by atomic force microscopy." Science **267**(5194): 68-71.
Giessibl, F. J. (2003). "Advances in Atomic Force Microscopy." Rev. Mod. Phys. **75**: 949-983.
Glenister, F. K., R. L. Coppel, et al. (2002). "Contribution of parasite proteins to altered mechanical properties of malaria-infected red blood cells." Blood **99**(3): 1060-3.
Glover, D. J., H. J. Lipps, et al. (2005). "Towards safe, non-viral therapeutic gene expression in humans." Nat Rev Genet **6**(4): 299-310.
Golovko, D. S., T. Haschke, et al. (2007). "Nondestructive and noncontact method for determining the spring constant of rectangular cantilevers." Rev Sci Instrum **78**(4): 043705.
Graham, F. L. and A. J. van der Eb (1973). "A new technique for the assay of infectivity of human adenovirus 5 DNA." Virology **52**(2): 456-67.
Graham, F. L. and A. J. van der Eb (1973). "Transformation of rat cells by DNA of human adenovirus 5." Virology **54**(2): 536-9.
Hahn, C. and M. A. Schwartz (2008). "The role of cellular adaptation to mechanical forces in atherosclerosis." Arterioscler Thromb Vasc Biol **28**(12): 2101-7.
Han, G., P. Ghosh, et al. (2007). "Multi-functional gold nanoparticles for drug delivery." Adv Exp Med Biol **620**: 48-56.
Hansma, P. K., V. B. Elings, et al. (1988). "Scanning tunneling microscopy and atomic force microscopy: application to biology and technology." Science **242**(4876): 209-16.
Heim, R. and R. Y. Tsien (1996). "Engineering green fluorescent protein for improved brightness, longer wavelengths and fluorescence resonance energy transfer." Curr Biol **6**(2): 178-82.
Hertz, H. (1882). "Uber die Beruhrung fester elastischer Korper." J Reine Angew. Mathematik **92**: 156-171.
Hoffman, B. D. and J. C. Crocker (2009). "Cell mechanics: dissecting the physical responses of cells to force." Annu Rev Biomed Eng **11**: 259-88.
Hoffman, B. D., G. Massiera, J.C. Crocker (2007). "Fragility and mechanosensing in a thermalized cytoskeleton model with forced protein unfolding." Phys Rev E **76**.
Hutter, J. L., J. Bechhoefer (1993). "Calibration of atomic force microscope tips." Rev. Sci. Instrum. **64**(7): 1868-1873.

Ichihara, A., T. Tanaami, K. Isozaki, Y. Sugiyama, Y. Kosugi, K. Mikuriya, M. Abe, I. Uemura (1996). "High-speed confocal fluorescence microscopy using a Nipkow scanner with microlenses- For 3D imaging of fluorescent molecules in real-time." Bioimages **4**: 57-62.

Ingber, D. E. (1997). "Tensegrity: the architectural basis of cellular mechanotransduction." Annu Rev Physiol **59**: 575-99.

Ingber, D. E. (2003). "Mechanobiology and diseases of mechanotransduction." Ann Med **35**(8): 564-77.

Ingber, D. E., L. Dike, et al. (1994). "Cellular tensegrity: exploring how mechanical changes in the cytoskeleton regulate cell growth, migration, and tissue pattern during morphogenesis." Int Rev Cytol **150**: 173-224.

Jaalouk, D. E. and J. Lammerding (2009). "Mechanotransduction gone awry." Nat Rev Mol Cell Biol **10**(1): 63-73.

Janmey, P. A., U. Euteneuer, et al. (1991). "Viscoelastic properties of vimentin compared with other filamentous biopolymer networks." J Cell Biol **113**(1): 155-60.

Janmey, P. A., S. Hvidt, et al. (1990). "Resemblance of actin-binding protein/actin gels to covalently crosslinked networks." Nature **345**(6270): 89-92.

Janmey, P. A. and D. A. Weitz (2004). "Dealing with mechanics: mechanisms of force transduction in cells." Trends Biochem Sci **29**(7): 364-70.

Kasza, K. E., A. C. Rowat, et al. (2007). "The cell as a material." Curr Opin Cell Biol **19**(1): 101-7.

Larson, J. M., S.A. Schwartz, M.W. Davidson (2010). Resonant Scanning in Laser Confocal Microscopy. Microscopy U (online), Nikon Instruments, Inc.

Lévy, R., M. Maaloum (2002). "Measuring the spring constant of atomic force microscope cantilevers: thermal fluctuations and other methods." Nanotechnology **13**: 33-37.

Lim, C. T., E. H. Zhou, et al. (2006). "Mechanical models for living cells--a review." J Biomech **39**(2): 195-216.

Lin, A. J., N. L. Slack, et al. (2000). "Structure and structure-function studies of lipid/plasmid DNA complexes." J Drug Target **8**(1): 13-27.

Lippincott-Schwartz, J., N. Altan-Bonnet, et al. (2003). "Photobleaching and photoactivation: following protein dynamics in living cells." Nat Cell Biol **Suppl**: S7-14.

Lippincott-Schwartz, J. and G. H. Patterson (2003). "Development and use of fluorescent protein markers in living cells." Science **300**(5616): 87-91.

Lippincott-Schwartz, J., E. Snapp, et al. (2001). "Studying protein dynamics in living cells." Nat Rev Mol Cell Biol **2**(6): 444-56.

Lo, C. M., H. B. Wang, et al. (2000). "Cell movement is guided by the rigidity of the substrate." Biophys J **79**(1): 144-52.

Ltd., A. I. (2002). Piezoelectric Ceramics: Principles and Applications, APC International, Ltd.

Majumdar, A. (1999). "Scanning Thermal Microscopy." Annu Rev Mater Sci **29**: 505-585.

Mandadapu, K. K., S. Govindjee, et al. (2008). "On the cytoskeleton and soft glassy rheology." J Biomech **41**(7): 1467-78.

Masuda, M. and K. Fujiwara (1993). "Morphological responses of single endothelial cells exposed to physiological levels of fluid shear stress." Front Med Biol Eng **5**(2): 79-87.

McBeath, R., D. M. Pirone, et al. (2004). "Cell shape, cytoskeletal tension, and RhoA regulate stem cell lineage commitment." Dev Cell **6**(4): 483-95.
Merkel, R., P. Nassoy, et al. (1999). "Energy landscapes of receptor-ligand bonds explored with dynamic force spectroscopy." Nature **397**(6714): 50-3.
Meyer, G. a. N. M. A. (1990). "Optical-beam-deflection atomic force microscopy: The NaCl (001) Surface." Appl Phys Lett **56**: 2100.
Misteli, T. and D. L. Spector (1997). "Applications of the green fluorescent protein in cell biology and biotechnology." Nat Biotechnol **15**(10): 961-4.
Murphy, D. M. (2001). Confocal Laser Scanning Microscopy. Fundamentals of Light Microscopy and Electronic Imaging, Wiley-Liss.
Nakano, A. (2002). "Spinning-disk Confocal Microscopy- A Cutting Edge Tool for Imaging of Membrane Traffic." Cell Struct Func **27**: 349-355.
Nehls, S., E. L. Snapp, et al. (2000). "Dynamics and retention of misfolded proteins in native ER membranes." Nat Cell Biol **2**(5): 288-95.
Nobelprize.org. (2008). "The Nobel Prize in Chemistry 2008- Press Release." Retrieved 3 Jun 2011.
Noy, A., C.D. Frisbie, L.F. Rozsnyai, M.S. Wrighton, C.M. Lieber (1995). "Chemical Force Microscopy: Exploiting Chemically-Modified Tips To Quantify Adhesion, Friction, and Functional Group Distributions in Molecular Assemblies." J Am Chem Sco **117**(30): 7943-7951.
Paszek, M. J., N. Zahir, et al. (2005). "Tensional homeostasis and the malignant phenotype." Cancer Cell **8**(3): 241-54.
Phair, R. D. and T. Misteli (2001). "Kinetic modelling approaches to in vivo imaging." Nat Rev Mol Cell Biol **2**(12): 898-907.
Potter, H. (2001). "Transfection by electroporation." Curr Protoc Immunol **Chapter 10**: Unit 10 15.
Prasher, D. C. (1995). "Using GFP to see the light." Trends Genet **11**(8): 320-3.
Prasher, D. C., V. K. Eckenrode, et al. (1992). "Primary structure of the Aequorea victoria green-fluorescent protein." Gene **111**(2): 229-33.
Radmacher, M. (1997). "Measuring the elastic properties of biological samples with the AFM." IEEE Eng Med Biol Mag **16**(2): 47-57.
Radmacher, M. (2002). Measuring the Elastic Properties of Living cells by the Atomic Force Microscope. Atomic Force Microscopy in Cell Biology. B. P. Jena, J.K.H. Horber. San Diego, Elsevier Science (USA).
Radmacher, M., J. P. Cleveland, et al. (1994). "Mapping interaction forces with the atomic force microscope." Biophys J **66**(6): 2159-65.
Radmacher, M., M. Fritz, et al. (1995). "Imaging soft samples with the atomic force microscope: gelatin in water and propanol." Biophys J **69**(1): 264-70.
Radmacher, M., R. W. Tillamnn, et al. (1992). "From molecules to cells: imaging soft samples with the atomic force microscope." Science **257**(5078): 1900-5.
Reza Moheimani, S. O., Y.K. Yong (2008). "Simultaneous Sensing and Actuation with a Piezoelectric Tube Scanner." Rev Sci Instrum **79**: 073702.
Rotsch, C., K. Jacobson, et al. (1999). "Dimensional and mechanical dynamics of active and stable edges in motile fibroblasts investigated by using atomic force microscopy." Proc Natl Acad Sci U S A **96**(3): 921-6.
Sader, J. E., I. Larson, P. Mulvaney, L.R. White (1995). "Method for the Calibration of Atomic Force Microscopy Cantilevers." Rev. Sci. Instrum. **66**: 3789-3798.

Sader, J. E., I. Larson, P. Mulvaney, L.R. White (1995). "Parallel beam approximation for V-shaped atomic force microscope cantilevers." Rev. Sci. Instrum. **66**.

Sanderson, M. J. and I. Parker (2003). "Video-rate confocal microscopy." Methods Enzymol **360**: 447-81.

Schwartz, M. A. and M. H. Ginsberg (2002). "Networks and crosstalk: integrin signalling spreads." Nat Cell Biol **4**(4): E65-8.

Smith, D. P., A. Bryant, et al. (1987). "Images of a lipid bilayer at molecular resolution by scanning tunneling microscopy." Proc Natl Acad Sci U S A **84**(4): 969-72.

Sneddon, I. N. (1965). "The relation between load and penetration in the axisymmetric Boussinesq problem for a punch of arbitrary profile." Int. J. Eng. Sci. **3**: 47-57.

Sollich, P. (1998). "Rheological constitutive equation for a model of soft glassy materials." Phys Rev E **58**: 738-759.

Soumpasis, D. M. (1983). "Theoretical analysis of fluorescence photobleaching recovery experiments." Biophys J **41**(1): 95-7.

Spring, K. R., T.J. Fellers, M.W. Davidson (2009). Resolution and Contrast in Confocal Microscopy. Theory of Confocal Microscopy, Olympus Corporation.

Suresh, S., J. Spatz, et al. (2005). "Connections between single-cell biomechanics and human disease states: gastrointestinal cancer and malaria." Acta Biomater **1**(1): 15-30.

Swaminathan, R., C. P. Hoang, et al. (1997). "Photobleaching recovery and anisotropy decay of green fluorescent protein GFP-S65T in solution and cells: cytoplasmic viscosity probed by green fluorescent protein translational and rotational diffusion." Biophys J **72**(4): 1900-7.

Tao, N. J., S. M. Lindsay, et al. (1992). "Measuring the microelastic properties of biological material." Biophys J **63**(4): 1165-9.

Taylor, G. W., J.J. Gagnepain, T.R. Meeker, T. Nakamura, and L.A. Shuvalov, Ed. (1985). Piezoelectricity, 4 ed. New York, Gordon and Breach Science Publishers.

Treloar, L. R. (1975). The Physics of Rubber Elasticity. Oxford, Clarendon Press.

Watt, P. C., M. P. Sawicki, et al. (1993). "A review of gene transfer techniques." Am J Surg **165**(3): 350-4.

Weisenhorn, A. L., M. Khorsandi, S. Kasas, V. Gotozos, M.R. Celio, H.J. Butt (1993). "Deformation and height anomaly of sof surfaces sudied with the AFM " Nanotechnology **4**: 106-113.

Weisenhorn, A. L., P.K. Hansma, T.R. Albrecht, C.F. Quate (1989). "Forces in atomic force microscopy in air and water." Appl Phys Lett **54**: 2651-2653.

White, J. G., W. B. Amos, et al. (1987). "An evaluation of confocal versus conventional imaging of biological structures by fluorescence light microscopy." J Cell Biol **105**(1): 41-8.

Zhong, Q., D. Inniss, K. Kjoller, V.B. Elings (1993). "Fractured polymer/silica fiber surface studied by tapping mode atomic force microscopy." Surf Sci Lett **290**: L688-L692.

Zolotukhin, S., M. Potter, et al. (1996). "A "humanized" green fluorescent protein cDNA adapted for high-level expression in mammalian cells." J Virol **70**(7): 4646-54.

Zougagh, M. and A. Rios (2009). "Micro-electromechanical sensors in the analytical field." Analyst **134**(7): 1274-90.

Chapter Three:

Experimental Procedures and Analysis

3.1 Cell Culture

3.1.1 Mammalian Cell Culture

NIH3T3 Fibroblast cells were cultured in Dulbecco's Modified Eagle Medium (DMEM), supplemented with 10% heat inactivated Fetal Bovine Serum (FBS), 100 IU/mL penicillin, and 100 lg/mL streptomycin (all from Hyclone). Cells were grown on 100-mm tissue culture dishes (Corning) at 37°C and 5% CO_2. Before 100% confluency was reached, cells were passaged. Briefly, passaging cells follows these steps: Cells are rinsed using a solution of phosphate-buffered saline (PBS; tablets from Fisher Scientific), detached from the dish in which they have been cultured using a solution of trypsin-EDTA (Hyclone), isolated via centrifugation, and resuspended in fresh DMEM. Cells were seeded at the desired concentration on 35-mm glass-bottomed dishes (Mat Tek) for experiments. Long-term storage of cells involved suspension of cells in a solution of FBS supplemented with 10% dimethylsulfoxide (DMSO; Sigma), a cryoprotectant; cells were placed in a -80°C freezer in a "Mr. Frosty" container (Nalgene) which maintains a slow freezing rate of 1°C per hour. After one day, the temperature has dropped enough to be transferred to long term storage in liquid nitrogen at -176°C until needed.

3.1.2 Bacterial Cell Culture

Agar plates were prepared from a ratio of 25g Luria-Bertani medium (LB broth): 15g Agar in 1L dH_2O (both from BD DifCo). Kanamycin (Sigma) was added to a final concentration of 50µg/mL before setting occurred. DH5α *Escherichia coli* (*E. coli*) cells, which had been previously transformed with the plasmid of interest, were taken from storage at -80°C (where they are preserved in a solution of 50% glycerol: dH_2O) and streaked onto agar plates. These plates were grown overnight, upside-down, in an incubator at 37°C. The following day, individual colonies were picked and 3mL cultures of LB broth, supplemented with 50µg/mL kanamycin, were inoculated with these colonies. *E. coli* were cultured again overnight in a shaking incubator at 37°C and 250rpm. Kanamycin was added at all steps to ensure selection for transformed bacteria; the plasmid encoding each gene of interest also includes resistance to kanamycin. After growing overnight, the *E. coli* was isolated by

centrifugation and the pellet resuspended in buffer; the cells are then ready to be used in DNA isolation procedures.

3.2 Transfection

3.2.1 DNA Isolation and Quantification

Plasmid DNA was isolated from DH5α cells according to manufacturer's specifications using the Qiagen Spin MiniPrep Kit. Briefly, cells were lysed and the lysates applied to the Qiagen columns where DNA was absorbed onto the silica gel membrane during centrifugation. After washing, pure DNA was eluted from the column into a microcentrifuge tube.

Plasmid DNA was quantified using a UV spectrophotometer. The absorbance was read at a wavelength of 260nm, which corresponds to the peak absorbance of DNA.

$$A_{260} = \epsilon \cdot c \cdot l \quad [1]$$

Using the Beer-Lambert Law [1] with a molar absorptivity (ε) of 50 L $mol^{-1}cm^{-1}$ (which corresponds to double-stranded DNA and can be confirmed experimentally), and a known path length, the concentration of DNA in each sample was determined, and thus the volume corresponding to 1µg of DNA, which is needed for transfection. The purity of DNA is estimated based on the ratio of absorbance at 260nm and 280nm. A ratio of A_{260}/A_{280}= 1.8-2.0 is considered to be 'pure' (Glasel 1995); the absorbance contribution of proteins (measured at 280nm) and other aromatic compounds such as phenol (measured at 280nm) is low enough in this condition that they do not add significantly to the determined concentration of DNA. Also, as RNAse is added initially to the resuspension buffer, it is expected that any available RNA will have been largely degraded and thus will not contribute to the concentration value either.

3.2.2 Plasmids and Transfection

The Zyxin-mRFP plasmid was a kind gift of Anna Huttenlocher (Bhatt, Kaverina et al. 2002). The Actin-EGFP plasmid and the plasmid containing the PH domain of PLC-δ conjugated to EGFP were kind gifts of Dr. G.T. Charras and have been described previously (Charras, Hu et al. 2006; Hemsley, Hernandez et al. 2011).

Transfections were performed using a liposome method. For each dish of cells used for experiments, 50µL of solution was prepared consisting of 46µL DMEM and 4 µL Lipofectamine 2000 reagent (Invitrogen). A 50µL solution was also prepared of 1µg plasmid DNA in DMEM; these solutions were combined following a five minute equilibration period. If a double transfection, in which multiple plasmids containing different sets of DNA are introduced to the cell simultaneously, was being performed, each DNA suspension required its own solution of Lipofectamine. After incubation at room temperature for 25 minutes, 100µL of each solution was added directly to a dish of cells containing fresh DMEM. Cells were imaged two days following transfection.

3.3 Staining Procedure

In some cases, fibroblast cells were preserved and imaged by immunofluorescence. To add fluorescent tags, cells were submitted to the following protocol. Details of the chemical composition of all buffers are as follows. Fixative buffer: 2% Sucrose and 3.5% Paraformaldehyde (Fisher Scientific) in PBS buffer. Permeabilization buffer: 20mM HEPES (4-(2-hydroxyethyl)-1-piperazineethanesulfonic acid; Fisher Scientific), 300mM Sucrose, 50mM NaCl, 3mM $MgCl_2$, dissolved in 198mL distilled water; 1mL of 10% Sodium Azide (NaN_3; Fisher Scientific) and 1mL of Triton X-100 (Fisher Scientific) are dissolved into this (final concentration of 0.5%). Wash buffer: 20mL FBS (Hyclone) and 2mL of 10% Sodium Azide are dissolved in 400mL of PBS buffer.

First, cells were fixed by incubating with warmed (to 37°C) fixative buffer for 2 minutes. The paraformaldehyde in this buffer effectively cross-links all proteins and organelles within the cell, fixing them in place and killing the cell (Smit, Meijer et al. 1974). Cells were then permeabilized with warmed permeabilization buffer for 2 minutes; the Triton

X-100 in this buffer solubilises the lipid membranes, allowing dyes to enter the cell in subsequent steps. Cells were rinsed and then incubated with warmed wash buffer for 15 minutes.

Cells were then stained for actin using the following procedure. A 200µL solution containing 2µL Phalloidin AlexaFluor-488 (Invitrogen) in wash buffer was added to the cells; these were then incubated in the dark for 20 minutes. A second incubation for 15 minutes with wash buffer followed.

Cells were then stained for tubulin via immunofluorescence. All following steps were performed on ice. A 200µL solution of 1µL monoclonal mouse α-tubulin primary antibody (Abcam) in cold wash buffer was prepared, and, after rinsing with cold PBS buffer, the cells were incubated with the antibody solution for 15 minutes in the dark. Cells were rinsed with cold wash buffer, then incubated for an additional 15 minutes in the dark with a 200µL solution containing 4µL of rabbit anti-mouse secondary antibody conjugated to AlexaFluor 546 (Invitrogen) in cold wash buffer. After rinsing, a third incubation for 15 minutes with cold wash buffer followed. The nuclei were then stained using a 200µL solution of 0.4µL DAPI (Invitrogen) in cold PBS. Cells were incubated with this dye for 10 minutes in the dark, still on ice.

Cells were then ready to be mounted. After rinsing with cold PBS, 50µL of DABCO anti-fade reagent (Sigma) was added to the centre of the dish. A glass coverslip was gently lowered to the surface of the cells, minimizing the formation of bubbles. Excess liquid was blotted away from the edges of the dish and the coverslip was sealed in place using clear nail polish. Cells were stored in a fridge at 4°C until ready to be imaged (within one week of staining).

3.4 Drug Treatments

Cells were treated with nocodazole (Sigma) dissolved in DMSO (Fisher Scientific) at a final concentration of 10µM. Nocodazole was added to the cells by serial dilution; 3µL of a 1000X stock solution was added to 500µL of media which had been removed from the dish

of cells. This solution was carefully added to the dish of cells which was mounted on the microscope stage (held at 37°C) drop-wise, attempting to allow for even distribution of the drug. Cells were incubated in this manner for approximately 15 minutes before experiments were performed. Cells that were stained or used for force curve analysis were treated similarly, but incubation was performed for 1 hour, and done in an incubator at 37°C and 5% CO_2 instead of on the microscope stage.

Cells were treated with Y27632 (Sigma) dissolved in water at a final concentration of 10μM. This drug was added directly to the dish from a stock 1000X solution, but swirled to ensure even mixing of the drug in the dish. Cells were incubated for 30 minutes prior to experimentation in an incubator at 37°C and 5% CO_2.

3.5 AFM and Confocal Microscopy

All images of living and fixed cells were acquired on a Nikon TiE A1-R (Nikon) high-speed laser scanning confocal microscope with a 60X/NA1.2 water immersion lens. A NanoWizard II AFM (JPK Instruments) was mounted on the stage of the inverted confocal microscope. Simultaneous AFM-LSCM experiments were performed following the same general protocol in each case. An attached, well spread, interphase cell that was adequately expressing the plasmid of interest (i.e. clear actin stress fibres visible) was selected and 4D imaging was initiated. Image volumes of the cell of interest were acquired every 20 seconds for 5 minutes. After 60 seconds of imaging with no applied force, the AFM tip was brought into contact with the cell over the centre of the nucleus, as this is the highest and stiffest area of the cell. A constant force varying from 1nN, 5nN, 10nN, or 20nN was applied for the following 4 minutes. Experiments were also performed at 0nN as a control which did not involve contact with the AFM tip. All experiments without photobleaching were performed in resonant mode.

In some cases, cells were transfected with the PH domain of PLC-δ-EGFP, which illuminates the cell membrane. Experiments identical to those performed with the actin-EGFP transfection were performed in order to determine the indentation depth of the AFM tip over time with cells treated with 10μM nocodazole and no drug treatment. For these

experiments, the nucleus was also stained in order to properly position the AFM tip over the nucleus. This was done by adding 1µL of the live-cell dye Hoechst 33342 (Invitrogen) for every millilitre of media in the dish which contains the cells. The dishes were swirled gently to mix and incubated for 5 minutes. Then, the media was replaced with fresh, warm media and allowed to equilibrate for at least 30 minutes before experimentation.

In other cases, cells were photobleached before experimentation. By selectively bleaching areas along actin stress fibres, it was possible to determine changes in length of the bright and dark segments, allowing for analysis of the strain dynamics along actin stress fibres. These cells were subjected to the following protocol. The height of each cell was initially determined and thus the distance between each image plane in the image volume. Regions of interest were defined using a grid spaced at 5µm; horizontal or vertical lines of width 1.5µm were defined such that the maximal number of Actin fibres was crossed in a given cell as perpendicularly as possible. Photobleaching was performed on these regions of interest with a 488nm laser at a scan rate of 32 frames/second through the entire volume of the cell. This was accomplished by raising the microscope stage an interval approximately equal to the distance between each image plane following 1 minute of bleaching (two scans of 30 seconds each). Ten cycles were performed, bleaching 10 planes to account for the entire cell volume. Following bleaching, the z-boundaries were redefined to account for drift. Experiments were then performed as described above, though in this case, galvano mode was used instead of resonant mode to increase resolution.

The cantilevers used in experimentation were of two types: Veeco MSCT probes, and NanoWorld PNP-TR probes. Both probe types have silicon nitride (SiN_4) cantilevers, back-coated with either chromium-gold (PNP-TR) or titanium-gold (MSCT). The tips on all cantilevers were pyramidal in shape; with an opening angle of 35°. In all cases, the spring constant value was determined by the thermal resonance method (as described in Chapter 2) prior to experimentation; k varied (0.07±0.03 N/m) as multiple cantilever sizes were used to expand the force range available.

3.6 Image Analysis

Images were analyzed with ImageJ (http://rsb.info.nih.gov/ij/) and also the MTrackJ plugin (http://www.imagescience.org/meijering/software/mtrackj/). Images of fixed and stained cells are maximum intensity Z-projections of all slices and were adjusted to maximize the fluorophore signal; no other enhancements were applied to the images. All images of live cells containing actin-EGFP are maximum intensity Z-projections of the confocal planes which contained actin stress fibres (generally not exceeding 2-5μm at the base of the cell).

Cells used to track lateral stress fibre displacement were analyzed in the following manner. After adjustments to enhance brightness and contrast, points along actin fibres (separated by ≤ 5μm; less than the persistence length of F-actin (Arai, Yasuda et al. 1999; Brangwynne, Koenderink et al. 2007; van Mameren, Vermeulen et al. 2009)) were tracked using MTrackJ over time (Figure 3.1). Stress fibre displacement relative to time 0 (when AFM cantilever was approached) was measured at these points as a function of time and averaged over all points for all fibres. In some cases, kymographs (plots of image intensity vs. time) were generated using ImageJ to re-slice an image along a line drawn perpendicularly to the actin stress fibres or focal adhesions sites. Kymographs allow for clear visualization of the movement of a particular image feature as a function of time. Cells treated with nocodazole were analyzed in a similar manner.

Cells treated with Y27632 had no visible actin stress fibres. They nevertheless appear green as G-actin is still visible throughout the cell. For these cells, maximum intensity Z-projections were taken through the entire cell volume for each time point. After adjustments for brightness and contrast, the diameter of the cell was determined using a plot of intensity vs. distance along a line drawn through the centre of the rounded cell body. Expansion was determined relative to the diameter at 0 seconds.

To determine the indentation depth of the AFM tip during force application, the two image channels (green; cell membrane and blue; nucleus) of PLC-δ-EGFP transfected cells were merged into one stack. Instead of Z-projections, these stacks were projected orthogonally (XZ and YZ) along the plane of maximal tip indentation for each time point.

The cell height under the tip for all time points was determined by tracing an intensity plot profile along all images.

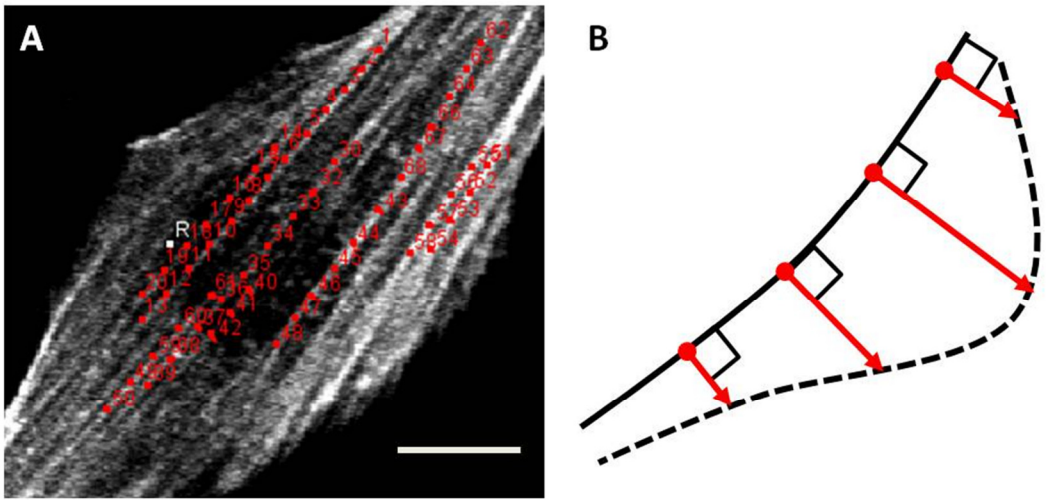

Figure 3.1: Tracking of Points along Stress fibres using MTrackJ. Points spaced less than 5µm apart were tracked along every visible stress fibre of each cell; an example of this distribution is shown in (**A**) (scale bar 15µm). The perpendicular displacement of each point along actin stress fibres relative to its initial position (Time 0sec; when force was applied) was calculated using the spatial coordinates at each time point. A schematic of this is shown in (**B**).

Images subjected to photobleaching were analyzed in the following way. As before, maximum intensity Z-projections were taken of only those confocal planes which contained actin stress fibres (2-5 of 12). Intensity plot profiles were taken along stress fibres containing bleached areas and thus it was possible to determine the width of each bleached and unbleached segment over time, allowing for strain calculations (see Chapter 5). MTrackJ was used to determine the (x,y) coordinates of each segment which were used in generating the colour maps to demonstrate the strain distribution and its changes over time.

3.6.1 Effective Resolution

The tracking method employed in the analysis of images contained within this thesis was a manual process. While point tracking software exists, the nature of our images made it difficult to use any automatic trackers because of the complexity of the intensity patterns. However, a similar 'detection system' is used in both the manual tracking used here and

automatic tracking programs. In each case, the point which is detected (in our case, by eye) is the brightest area of an intensity distribution; for example, the centre of an actin stress fibre. The diffraction limit discussed in Chapter 2 is used to describe the complete resolution of two point sources. However, these point sources are in fact distributions. When tracking the movement of the brightest section of a distribution, it is not necessary for full resolution between the initial and final locations of the brightest spot. This increases the effective resolution of our system, to the extent that it may surpass the diffraction limit. In actuality, the minimal distance which can be resolved is limited by the size of the pixels in the image.

3.7 References

Arai, Y., R. Yasuda, et al. (1999). "Tying a molecular knot with optical tweezers." Nature **399**(6735): 446-8.

Bhatt, A., I. Kaverina, et al. (2002). "Regulation of focal complex composition and disassembly by the calcium-dependent protease calpain." J Cell Sci **115**(Pt 17): 3415-25.

Brangwynne, C. P., G. H. Koenderink, et al. (2007). "Bending dynamics of fluctuating biopolymers probed by automated high-resolution filament tracking." Biophys J **93**(1): 346-59.

Charras, G. T., C. K. Hu, et al. (2006). "Reassembly of contractile actin cortex in cell blebs." J Cell Biol **175**(3): 477-90.

Glasel, J. A. (1995). "Validity of nucleic acid purities monitored by 260nm/280nm absorbance ratios." Biotechniques **18**(1): 62-3.

Hemsley, A. L., D. Hernandez, et al. (2011). "Precisely delivered nanomechanical forces induce blebbing in undifferentiated mouse embryonic stem cells." Cell Health and Cytoskeleton **3**: 23-34.

Smit, J. W., C. J. Meijer, et al. (1974). "Paraformaldehyde fixation in immunofluorescence and immunoelectron microscopy. Preservation of tissue and cell surface membrane antigens." J Immunol Methods **6**(1-2): 93-8.

Stauffer, T. P., S. Ahn, et al. (1998). "Receptor-induced transient reduction in plasma membrane PtdIns(4,5)P2 concentration monitored in living cells." Curr Biol **8**(6): 343-6.

van Mameren, J., K. C. Vermeulen, et al. (2009). "Leveraging single protein polymers to measure flexural rigidity." J Phys Chem B **113**(12): 3837-44.

Chapter Four:

Displacement of Actin Stress Fibres in Response to Locally Applied Force

4.1 Nanoscale Movement of Actin Stress Fibres in Response to a Locally Applied Force

In our first study, we demonstrate the response of actin stress fibres to locally applied forces over short time scales. Simultaneous AFM and LSCM experiments were performed on 3T3 fibroblast cells transiently expressing actin-EGFP (Figure 4.1A). It was found that the majority of stress fibres in our cells tended to form along the bottom of the cell, under the nucleus and parallel to the substrate (Figure 4.1B). Force was then applied to the cell by an AFM tip positioned over the nucleus.

To enhance the visibility of any response that occurred, a maximum intensity projection was created from those confocal planes which contained well defined stress fibres. In this type of image, the brightest pixel at each pixel location through the image volume is selected, amalgamating multiple confocal planes into a single 2D image; this was used for analysis at each time point (Figure 4.1D. Stress fibre movement was then quantified by tracking multiple points along each stress fibre in the cell as a function of time. If a stress fibre moved, deformed, or otherwise displaced from its initial position in the maximum intensity projection, a displacement vector was mapped from one of the initial tracking points to a new point on the fibre at the next time step normal to initial fibre position (as described in Chapter 3, and Figure 4.1C). This method allowed us to quantify lateral displacements of the stress fibres relative to their initial position. However, this methodology precluded us from tracking stretching or retraction along stress fibres that did not result in any lateral movement relative to the initial fibre position. It was also impossible to determine whether slight displacement occurred in the axial (Z) direction using this technique; however, the limits of resolution in the axial direction dictate that, at this scale, axial displacement would be undetectable.

Kymographs were produced to demonstrate qualitatively the characteristics of movement that occurred along stress fibres (Figure 4.1D). These plots demonstrate changes in intensity along a region of interest over time. In the kymographs of Figure 4.1D, it can be seen that, should perpendicular movement of stress fibres occur, a non-zero slope of intensity over time is apparent. On average, the amount of stress fibre movement was proportional to

the amount of force applied and occurred within 20 seconds of force application (Figure 4.2). A plot of the average total displacement on all stress fibres at each time point reveals that a force dependant displacement of stress fibres is apparent after 20 seconds of force application and that displacement increases over time for all forces. Control cells which were not exposed to any force also displayed stress fibre displacements which can be attributed to natural remodelling dynamics. It should be noted, however, that, in any given cell, there were always stress fibres that did not display any visible movement (horizontal lines in kymographs of Figure 4.1D). A second control was employed in which cells were fixed with paraformaldehyde prior to imaging to examine any effects of microscope drift and tracking errors. As paraformaldehyde works as a cross-linking chemical within cells, stress fibre movement is not expected to occur. As can be seen in Figure 4.2, there is a small amount of drift in the tracking but it is well below the measured response of cells exposed to 0-20 nN of force, indicating this does not contribute significantly to the measured response.

Spatial maps of the magnitude of stress fibre displacement demonstrate that the spatial distribution of stress fibre movement was not isotropic (Figure 4.3). In other words, the cell and actin stress fibres did not simply bulge out in a circular deformation profile around the tip contact point. In fact, stress fibre displacements were localized and tended to evolve with time; the stress fibres which did move exhibited one of two types of displacement: a slight lateral bulge in direct response to the AFM cantilever, generally within 5-10 μm of the tip location, or retraction at cell edges distant from the AFM cantilever (as observed in the displacement maps, Figure 4.3). Displacements taking place near the point of contact were a direct physical response to force and occurred within the first 60 seconds of force application. However, retraction dynamics, in which distal edges or extensions of the cell moved towards the centre of the cell, generally occurred much later (60-240 seconds) after force application and imply that the mechanical stimulus also results in biochemical remodelling of the F-actin cytoskeleton. These later retraction dynamics are responsible for what appears to be a continuously increasing average displacement of points along stress fibres at later time points (Figure 4.2).

Since all of the actin stress fibres lie on a plane which passes under the nucleus (see Figure 4.1B), we can conclude that there was no direct contact between the indenting tip and

the fibres, and thus there cannot possibly be a direct displacement due to the tip indentation. However, in nearly all cases, the nucleus was observed to expand or translocate in response to this force. This suggests that the slight displacement of stress fibres in the vicinity of the nucleus is likely due to this nuclear deformation.

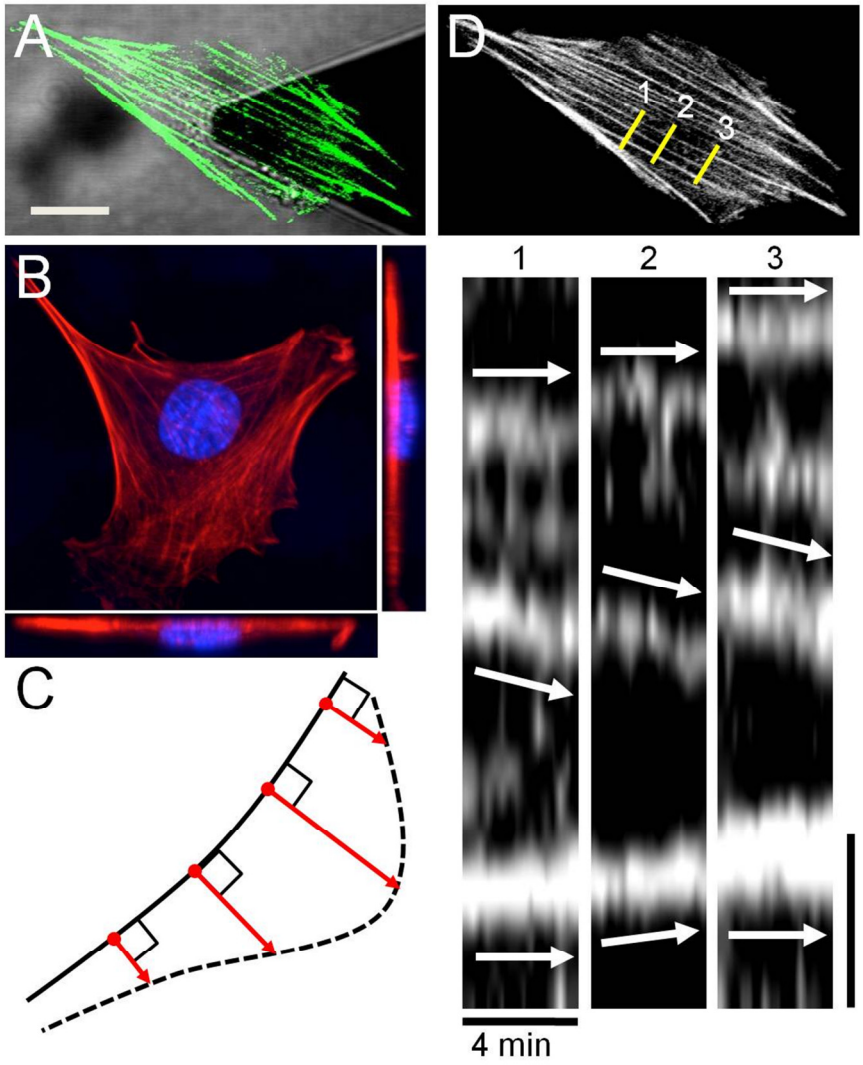

Figure 4.1: Stress fibre localization, deformation, and the tracked response to local forces. An NIH3T3 cell expressing actin-EGFP (**A**) under the AFM tip (black triangle) which is centered over the nucleus (scale bar = 15 µm, applies to **B**, and **D**). A fixed cell stained for actin (red) and DNA (blue) (**B**) reveals that stress fibres tend to localize underneath the nucleus and parallel to the substrates as can be seen in the ZX and ZY projections. Stress fibre tracking (**C**) was achieved by mapping perpendicular displacement vectors (red) from an initial point on the fibre at time zero (solid line) to a new point on the same fibre at the next time step (dotted line) normal to initial fibre position. Kymographs (**D**) reveal that not all stress fibres deform or move in response to force (vertical scale bar = 2 µm). In this case, kymographs are produced in three positions (numbered) perpendicular to three actin stress fibres. The middle stress fibre deforms over time (downward arrow) but the two surrounding stress fibres do not deform significantly (horizontal arrows).

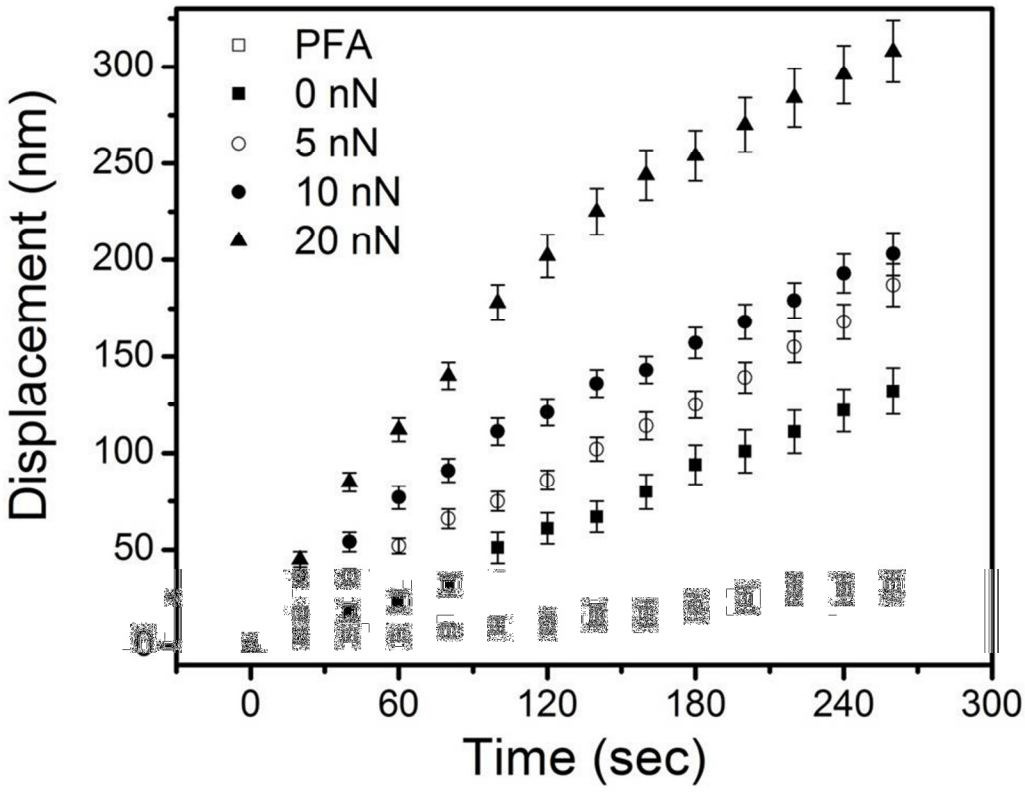

Figure 4.2: Average displacement of actin stress fibres for all cells examined over time in response to locally applied forces. The amount of stress fibre movement is proportional to the applied force and begins to occur within 20 seconds. Displacement occurring in cells exposed to 0 nN force represents normal remodelling dynamics of actin stress fibres. A further control was performed with cells fixed with paraformaldehyde. Any displacement in this control can be attributed to microscope drift or error within the tracking method. All values are average ± S.E.M.; n = 10 cells for 5-20 nN, n = 5 cells for 0nN, n = 3 cells for the PFA control.

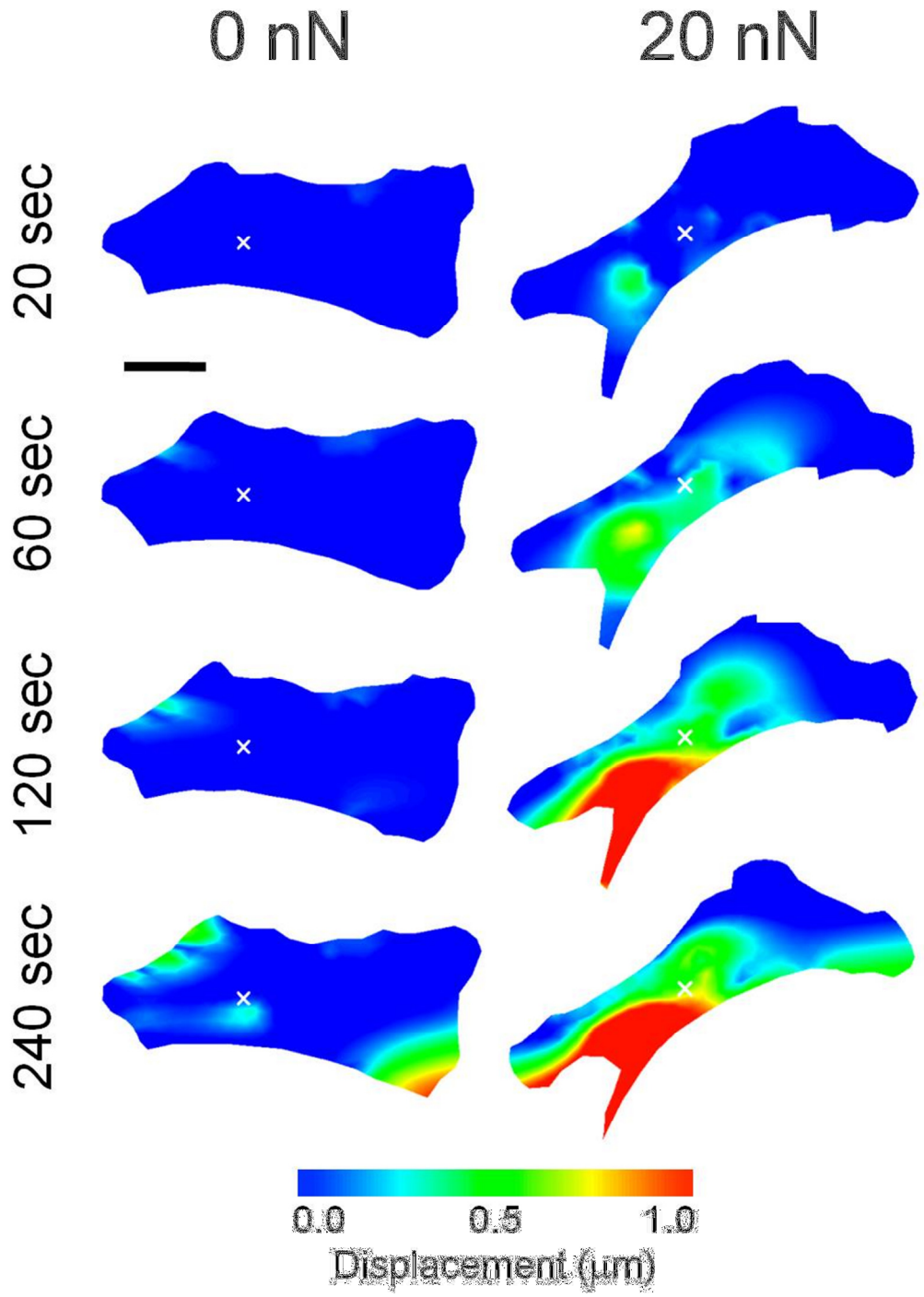

Figure 4.3: Spatial maps of stress fibre displacement for representative NIH3T3 cells experiencing 0 nN or 20 nN of applied force. The displacement vectors for two cells were plotted as spatial maps relative to the initial position (scale bar = 15 µm, applies to all). It is clear that far more displacement occurs in response to 20 nN than to 0 nN. These maps also reveal a qualitative nature to the observed displacements. Displacement of actin stress fibres generally takes place immediately (within 20 seconds) and near to the point of force application (the contact point of the AFM cantilever is marked with an 'x'). At later times retraction sometimes takes place at distant cell edges (red areas at 120 and 240 seconds after the application of 20nN).

Extending our analysis further, we calculated the percentage of all tracked points having a non-zero displacement at every time point in all experimental and control cells, normalized with the values for fixed cells (Figure 4.4). The error bars in Figure 4.4 correspond to the percentage of points which move in the PFA control. While fixed cells are not expected to experience any movement in response to force, a gradual increase in points moving is visible in our measurements. This value is much lower than all responses of living cells to force, as expected, and can be taken as a representation of the error in the tracking process. This error has a cumulative effect, which explains why the error bars increase over time. These larger error bars also make it more difficult to assess the validity of whether a plateau is reached at all forces; however, a trend is nevertheless visible.

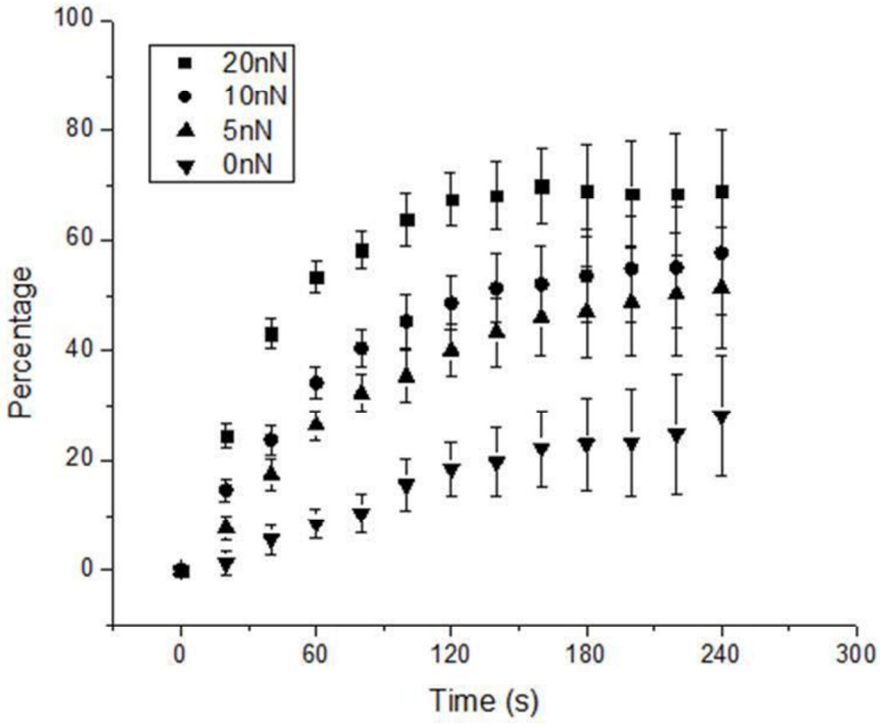

Figure 4.4: Percentage of tracked points moved over time in response to local forces. This plot contains the percentage of points for every cell at all forces which display a non-zero displacement as a function of time. The data was normalized by subtracting the percentage of points which moved in the PFA control, and, as this represents any error in the measurement, the values corresponding to the PFA control are represented as the error bars on each point. At early times (<120 seconds) this is dominated by a direct displacement of stress fibres in response to the AFM cantilever. However, at later times (>120 seconds) these stress fibres stop moving and the downstream effect of mechanical stimulation begins to take over; namely, the force induced retraction and remodelling of stress fibres at distant sites from the contact point. As in Figure 2, n = 10 cells for 5-20 nN, n = 5 cells for 0nN; 40-70 points are tracked on each cell. Values ± Percentage of Points moved in PFA control.

It can be seen that after ~120 seconds of force application, the percentage of moving points reaches an approximate plateau at each applied force. When compared to the data for the average displacement as a function of time we can clearly see that although the average displacement continues to increase after ~120 seconds for all forces, the number of points moving along a stress fibre has become relatively constant. This suggests that the number of stress fibres undergoing some sort of movement steeply increases within the first 120 seconds of force application and after this point very few new stress fibres begin to move. Therefore, the direct response of actin stress fibres to force is greatest within 20-120 seconds of contact with the AFM tip. However at later times, remodelling still occurs; this suggests an indirect response due to other processes, likely biological in nature, which have been signalled to occur from the direct application of force.

4.2 Effect of Anti-Cytoskeletal Drugs on Nanoscale Stress Fibre Movement

Deformation of stress fibres far from the point of contact (~30-50 μm) following force application, and the lack of any observed large scale isotropic deformation, suggests that further components of the cell are involved in transmission of the mechanical stimulus. To investigate the contribution of different components of the cytoskeleton (actin and tubulin), two different anti-cytoskeletal drugs were employed: nocodazole, to eliminate microtubules, and a ROCK inhibitor, Y27632, whose downstream effect is to inhibit acto-myosin contractility and actin stress fibre formation (Narumiya, Ishizaki et al. 2000; Fukata, Amano et al. 2001). As can be seen in Figure 4.5, both of these treatments are effective at altering cytoskeleton morphology and reducing cell elasticity (Young's Modulus, E).

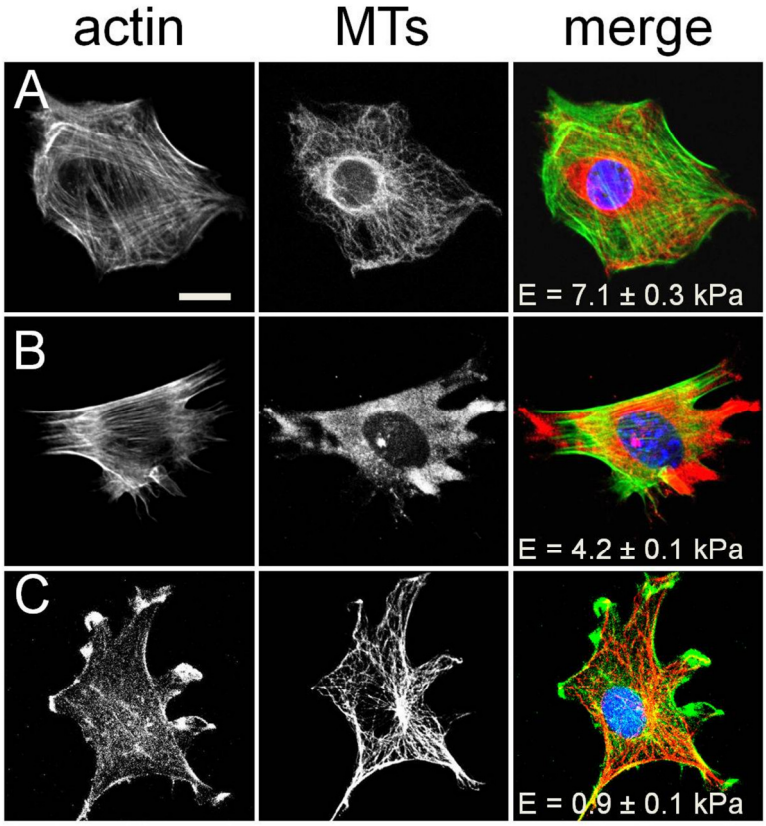

Figure 4.5: Changes in morphology and elasticity following treatment with anti-cytoskeletal drugs. Fixed NIH3T3 cells were stained for actin (first column; green in third column), tubulin (second column, red in third column), and DNA (blue) (scale bar = 15 µm, applies to all). Cells were untreated (**A**) or treated with 10 µM nocodazole (**B**) or 10 µM Y27632 (**C**). Treatment with nocodazole specifically eliminates the microtubule network structure, while treatment with Y27632 largely eliminates actin stress fibres. The elasticity of similarly treated cells as measured over the nucleus are also reported; treatment with nocodazole and Y27632 reduces the Young's Modulus from ~ 7 kPa to ~4 kPa and ~1 kPa respectively (values are the average ± S.E.M., n = 10-12 cells; 5-6 force curves per cell).

4.2.1 Nocodazole Experiments

Cells were treated with 10 µM nocodazole to depolymerize the microtubule network. A distinct morphological change was apparent in the majority of cells within 10-15 minutes of drug treatment. Cells that were chosen for study however, remained attached and maintained distinct actin stress fibres, though were generally visibly smaller in size. This allowed our previously described stress fibre tracking method to be employed. The Young's modulus of cells treated similarly with nocodazole was calculated to be almost half that of

cells without drug treatment (~4 kPa vs. ~7 kPa respectively; see Figure 4.5), indicating that microtubules play a significant role in contributing to the mechanical stiffness of these cells. Cells pre-treated with 10 μM nocodazole were submitted to an identical force experiment with the AFM at 20 nN. As demonstrated and described in section 4.1, an application of a 20 nN force without drug treatment results in a significant stress fibre displacement observed over time (Figure 4.6). Following treatment with 10 μM nocodazole, an application of a 20 nN force has a significantly reduced effect and is comparable to the displacement observed for the controls at 0 nN force, with and without nocodazole treatment (Figure 4.6); this has been attributed to normal baseline remodelling.

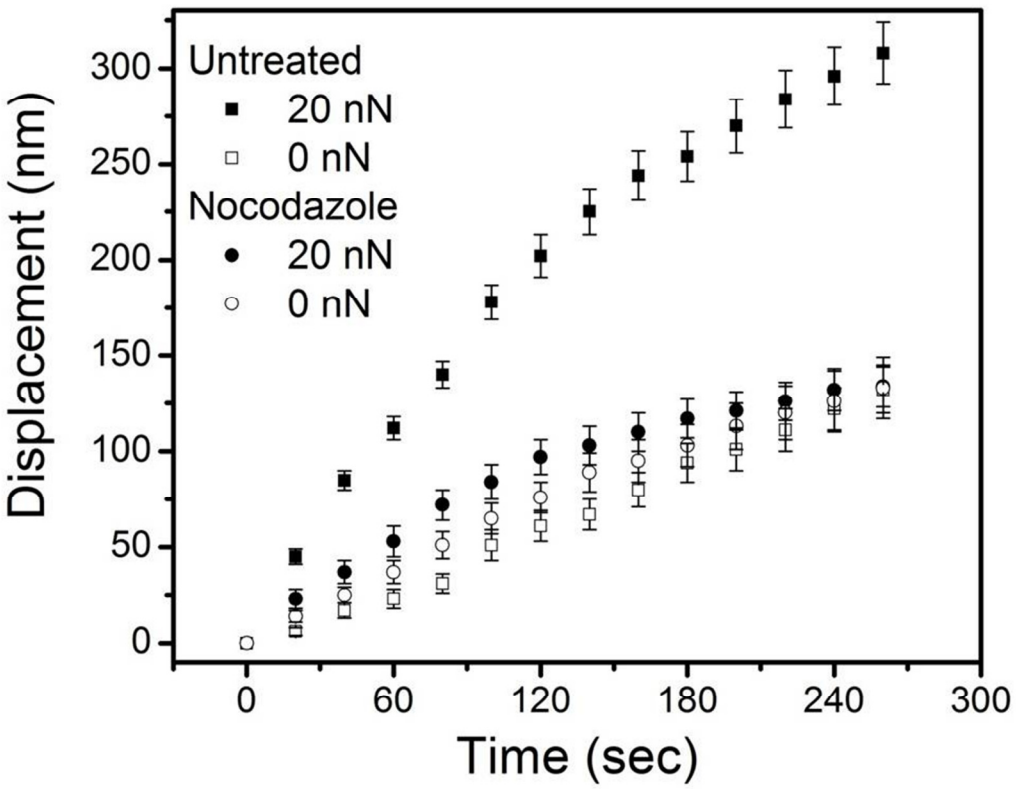

Figure 4.6: Effect of nocodazole pre-treatment on the average displacement of stress fibres over time at 0 nN and 20 nN force. Cells were pre-treated with 10 μM nocodazole and either left un-stimulated or exposed to a 20nN force. The data for a cell experiencing a 0 or 20 nN applied force, without treatment with nocodazole, is re-plotted from Figure 4.2. Following treatment with nocodazole, cells experiencing a 20nN force only exhibit a minor increase in displacement when compared to cells experiencing no force, with or without nocodazole pre-treatment. This implicates the importance of an intact microtubule cytoskeleton for the transmission of force through the cell. All values are average ± S.E.M.; n = 4, nocodazole treated cells.

It is clear that, although the cells are softer and therefore more deformable, no significant displacement of the actin stress fibres was observed over controls, and no isotropic deformation takes place. Since the microtubule network has been eliminated in these cells, the results suggest that microtubules play an important role in the transmission of force through the cell which is consistent with results obtained previously (Pelling, Veraitch et al. 2009). It is worth noting, that the minimal displacement that does occur is apparent within 20 seconds following force application, as in the previous measurements. To visually demonstrate this difference, stress fibre displacement maps were generated for cells treated with nocodazole at both 0 nN and 20 nN (Figure 4.7). Cells treated with nocodazole display no significant visual difference (compared to untreated cells) when exposed to 20 nN force. However, remodelling dynamics continue to occur at cell edges at long time scales.

There was some concern as to whether the morphological changes that occur with nocodazole treatment are responsible for the change in stress fibre dynamics, whether by increased cell and stress fibre contact due to a change in tip indentation depth or a change in the maximal force applied. To confirm that the indentation depth of the AFM tip on nocodazole treated cells and non-treated cells, as well as the cell heights were comparable, a series of experiments were performed with cells transfected for PLC-δ-EGFP. This protein is localized to the cell membrane, and thus provides an outline of the cell and a direct visualization of the indentation depth. To confirm that force was applied over the nucleus, DNA was also stained using the dye Hoescht 33342. It can be seen in Figure 4.8E that there is no significant difference (p value > 0.85) between the heights of treated and non-treated cells, both before and after indentation. Further, cross-sectional views of the cells at the point of indentation (marked with a line in Fig.4.8 A, C) demonstrate that the AFM tip does not contact the surface of the dish, even after 4 minutes under 20 nN force, for both treated and non-treated cells (Figure 4.8 B, D). Indeed, there is ~7 µm remaining between the tip and the base of the cell; we can thus confirm that there is no direct contact between the AFM tip and the stress fibres which, as it has been shown previously in this thesis, lie within 2-3 µm of the surface, under the nucleus. While we suspect that some stress fibre displacement is due to nuclear deformations as previously mentioned, it is clear that deformations occurring far from the point of contact remain valid results and are not artefacts of our measurement technique.

4.2.2 ROCK Inhibitor Experiments

The second drug that was used was the commonly employed Rho Kinase inhibitor, Y27632. The Rho pathway is integral to the formation of actin stress fibres and their contraction during cell expansion and motility (Fukata, Amano et al. 2001). Inhibition of ROCK eliminates the cell's ability to form intact actin stress fibres. As cells were transfected with actin-EGFP, regardless of the state of actin (whether it be F-actin or G-actin), cells remain visible with the confocal microscope. Treatment with 10 μM of Y27632 for 30 minutes results in a highly rounded morphology and a Young's modulus of ~1 kPa, seven times smaller than that of native cells (see Figure 4.5). Although there are no intact stress fibres, there remains a visible response of the cell to the application of 20 nN of force. In this case, the diameter of the rounded cell body was measured as a function of time. A distinct isotropic bulging around the nucleus (as seen in Figure 4.9) is apparent immediately following force application, resulting in a diameter increase of approximately 20%. The cell then returned close to its initial dimensions after removal of the force. Interestingly, retraction of cell edges in response to force was not observed. This implies that cell edge retraction is not possible without stress fibres, and is consistent with inhibition of ROCK, as there is no contraction mechanism available to provide the necessary tension.

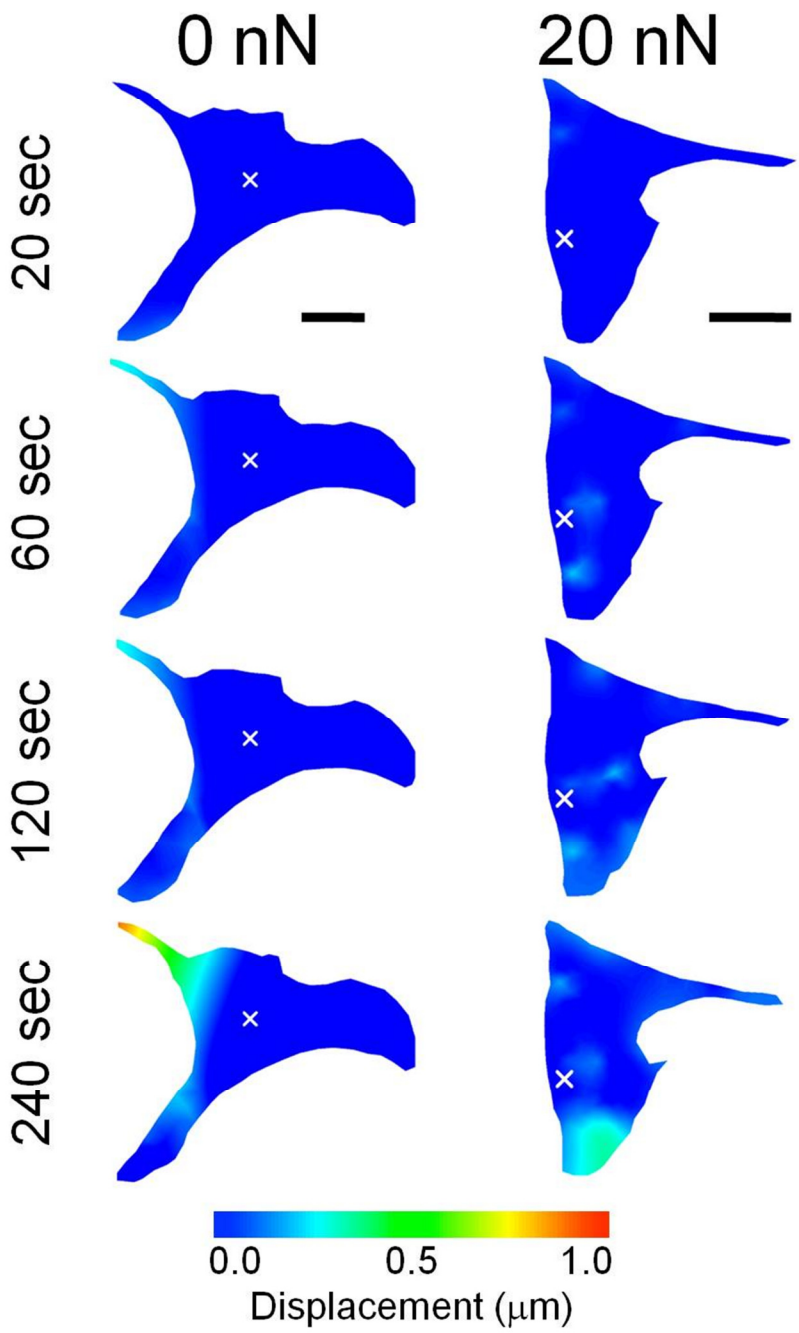

Figure 4.7: Spatial maps of displacement over time for representative NIH3T3 cells after treatment with 10 μM nocodazole at 0 nN and 20 nN force. Spatial maps of displacement for representative cells were constructed by plotting the displacement vectors over time relative to the initial position (scale bar = 25 μm for 0 nN and 15 μm for 20 nN). It is clear that the stress fibre displacements that occur in response to 20 nN without drug treatment are largely eliminated following treatment with nocodazole, as the spatial map for 20 nN greatly resembles that of 0 nN. As before, the displacement that does occur is apparent as both a slight response near to the point of force (as marked by an 'x'), and as a retraction along the edges of the cell. Moreover, although the cells are much softer (Figure 1.3) after nocodazole treatment no isotropic deformation is observed near the point of contact. Note: the displacement scale bar is identical to Figure 4.3.

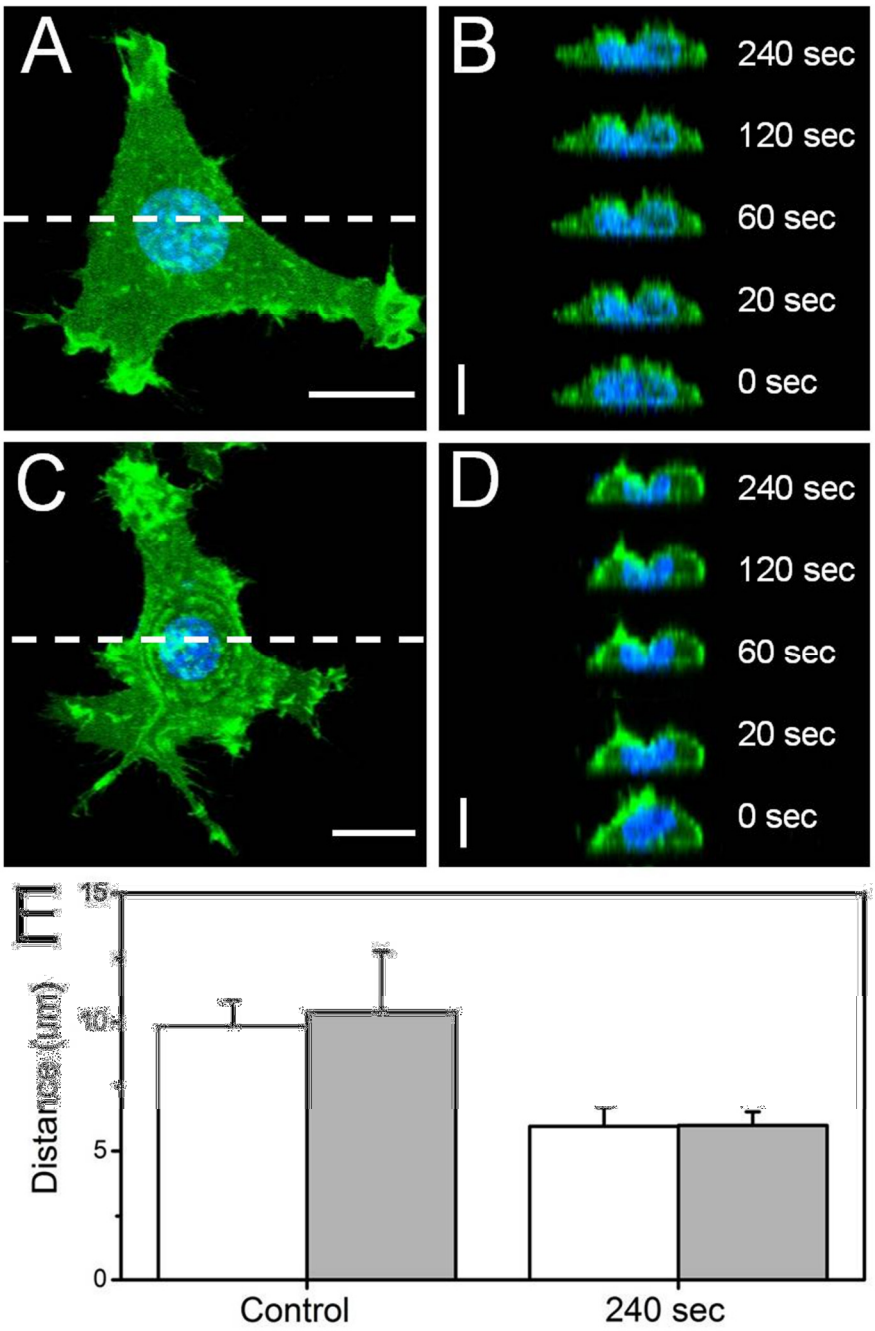

Figure 4.8: Indentation depth of AFM tip in PLC-δ-EGFP transfected NIH3T3 cells. Maximum intensity Z-projections of non-treated (**A**) and nocodazole treated (**C**) cells transfected for PLC-δ-EGFP (green) and stained for DNA with Hoescht 33342 dye (blue). The horizontal line indicates the plane in which cross-sectional views are shown in (**B**; non-treated cell) and (**D**; nocodazole treated cell). Here, the indentation of the AFM tip can be seen over time. There is no significant difference in cell height under the AFM tip either before or after 4 minutes of an applied 20nN force, when treated with 10 µM nocodazole (p value >0.85). Horizontal and vertical scale bars = 15 µm; n= 5 cells in each measurement.

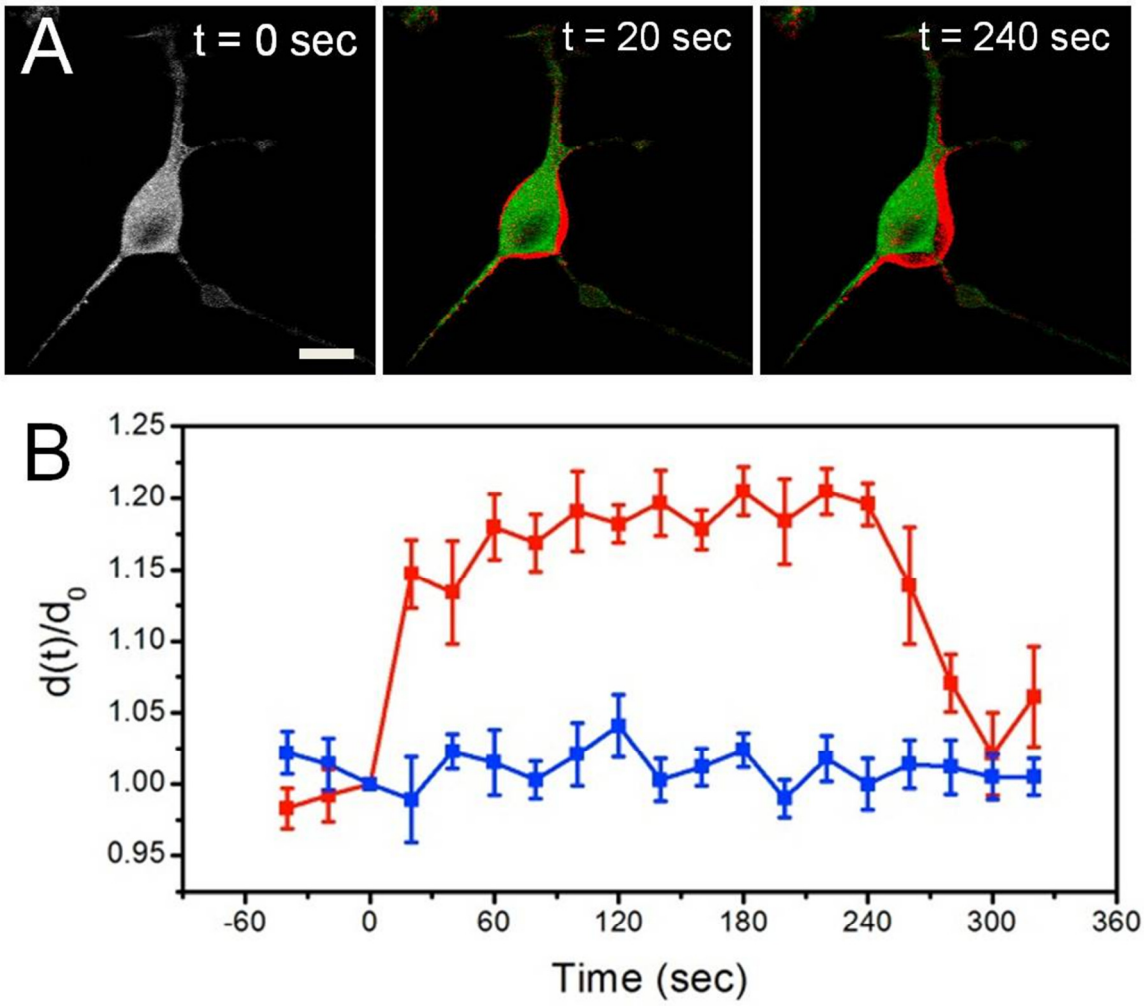

Figure 4.9: Effect of 10 µM Y27632 on the response of NIH3T3 cells to local forces. NIH3T3 cells were treated with 10 µM Y27632 and mechanically stimulated. An applied force of 20 nN caused an isotropic expansion around the nucleus within 20 seconds of force application (**A,** scale bar = 15 µm). The images at t = 20 and 240 seconds are overlays of the original cell shape (green) and the difference image (red) between the cell shape at 0 and 20 or 0 and 240 seconds. The diameter of each cell (d(t)) was measured before and after force application and the average expansion relative to time zero is reported over time in **B**. There is a significant expansion in response to 20 nN force (red) that is not apparent at 0 nN (blue). After removal of force (t=240s) the cell regains its former dimensions. Error bars are ± S.E.M.; n= 4 for both 0 and 20 nN.

4.3 References

Fukata, Y., M. Amano, et al. (2001). "Rho-Rho-kinase pathway in smooth muscle contraction and cytoskeletal reorganization of non-muscle cells." Trends Pharmacol Sci **22**(1): 32-9.

Narumiya, S., T. Ishizaki, et al. (2000). "Use and properties of ROCK-specific inhibitor Y-27632." Methods Enzymol **325**: 273-84.

Pelling, A. E., F. S. Veraitch, et al. (2009). "Mechanical dynamics of single cells during early apoptosis." Cell Motil Cytoskeleton **66**(7): 409-22..

Chapter Five:

Strain Dynamics in Actin Stress Fibres in Response to Locally Applied Force

5.1 Correlated Movement of Stress Fibres and Focal Adhesions

Our results from the previous study indicate that one of the primary long-term responses of the cell is for the edges to retract following the application of force over the nucleus (see Figure 4.3). In order to further investigate the mechanism resulting in our observations of force stimulated stress fibre displacement at cell edges, we generated cells transiently expressing actin-EGFP and zyxin-mRFP (Rottner, Krause et al. 2001). Zyxin has been proposed as a 'tension sensing' protein, recruiting to FA complexes as they form along actin stress fibres and anchoring cells to the substrate (Lele, Pendse et al. 2006; Colombelli, Besser et al. 2009). Moreover, it has been shown that there is a strong correlation between zyxin localization and stress fibre anchor and stress points (Rottner, Krause et al. 2001).

These doubly transfected cells allowed us to examine the remodelling and/or movement of focal adhesion (FA) sites which are mechanically and biochemically linked to actin stress fibres. AFM-LSCM experiments were again carried out with the application of a 20nN stimulus on these cells. In general, it was observed that FA sites did not move if the stress fibres remained stationary or simply deformed. However, stress fibres which displayed a large displacement resulted in a correlated movement of FA sites. As can be seen in the kymographs in Figure 5.1, the FAs associated with non-moving stress fibres remain stationary and those associated with moving stress fibres appear to slide along the surface in tandem with the stress fibre. These results indicate that the movement of actin fibres that retract following force application is correlated with the movement of Zyxin rich FA sites. In light of previous work and the results presented here, this suggests that the mechanical stimulus applied to the cells results in FA remodelling at later time points, leading to stress fibre movement far from the point of contact. Moreover, the zyxin-mRFP signal was not observed to diminish over time on moving stress fibres, which suggests that the tension within the stress fibre remains throughout the displacement.

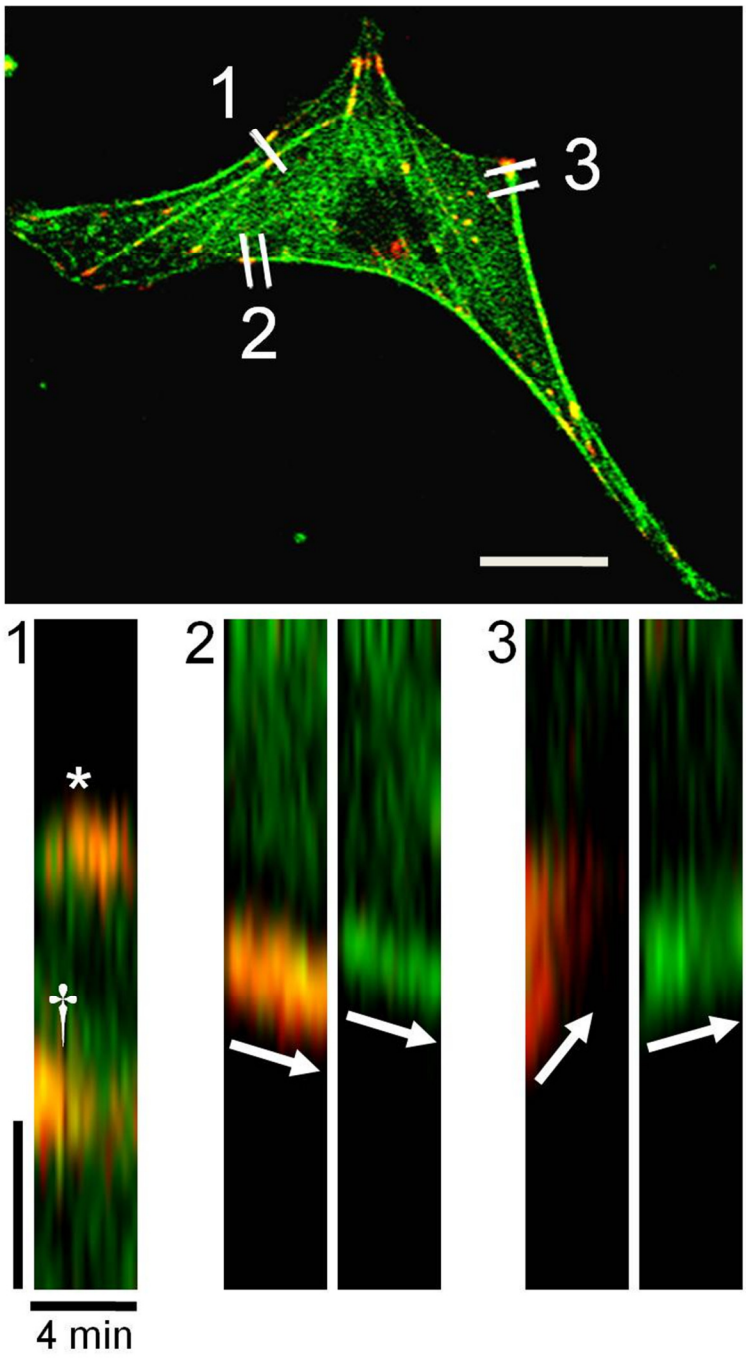

Figure 5.1: Correlated movement of focal adhesions with stress fibres in response to a locally applied force. An NIH3T3 cell expressing both actin-GFP and zyxin-mRFP (scale bar = 24 µm). Kymographs were generated for three separate locations on the cell (vertical scale bar = 2 µm). It can be seen in **1** that these fibres are sliding along their length (but not displacing laterally) which results in the movement of one FA into the image at ~120 seconds (*) and another FA out of the image at ~60 seconds (†) after force application. In **2** and **3,** a correlated downward lateral displacement of stress fibres and FAs are observed (upward and downward arrows). In **3**, the stress fibre begins to retract downward after force application which results in the movement of an associated FA out of the kymograph.

5.2 Strain Dynamics in Actin Stress Fibres

5.2.1 Photobleaching Analysis

In the experiments reported so far, we have succeeded in quantifying the lateral displacement of actin stress fibres in response to locally applied forces, as well as correlating these movements with focal adhesion displacement, and indicating the dependence of the displacement on the presence of microtubules within the cell. The correlated movement of zyxin with actin stress fibres indicates the maintenance of tension within the stress fibre; however, our previous experiments measuring lateral displacements did not provide us with a manner in which this could be experimentally confirmed. We have developed a method which allows us to measure the strain along the length of an actin stress fibre using the photobleaching capabilities of the confocal microscope.

Fibroblast cells which were transfected for actin-EGFP (and, in some cases, also zyxin-mRFP) were photobleached in a regular pattern of lines 1.5µm in width, 5µm apart, such that the maximal number of stress fibres were crossed in a perpendicular fashion (Figure 5.2D). This effectively rendered the actin fibres into visibly segmented lines (Figure 5.2C). As in previous experiments, image stacks were taken every 20 seconds (or every 30 seconds for those cells which had been doubly transfected) over the course of 5 minutes; after one minute, the AFM tip was approached and a force of either 0nN or 20nN applied. An intensity profile along the length of each segmented line was drawn for each time point; the data obtained from this were analysed with a Python script (see Appendix A) which allowed us to determine the strain for each bright segment and bleached segment along each stress fibre relative to time zero (when the AFM tip was approached).

The details of the analysis are as follows. The data was first smoothed using a running average with a small window (10 points) to eliminate some sources of noise, improving the fit. In order to find the peaks and lows (so called bright and dark regions of the segmented lines, respectively), a threshold was applied to the data. Instead of a fixed value however, the data was smoothed with a wider window (adjustable value; 20-40) and a shift value to lower the curve below that of the actual data (adjustable value; 5-15). These adjustable values were selected manually in increments of 5 in order to best fit the data. This method of thresholding was used as some segments of the line had very high intensity peaks

while others had much lower intensity peaks; a fixed value would not have allowed for the detection of both sets of peaks. Following thresholding, the peaks were defined as the mid-point of any set of intensity points which lay above the threshold (single data points were ignored as noise); the lows were the mid-points of the data which lay below the threshold. Each individual peak was then fit to a double Heaviside function (Eq. [1]), approximated as a sigmoidal curve (Figure 5.2E). The particular expression used to fit the data (Eq. [2]) had four parameters to fit: amplitude (A), peak location (x_0), full width at half maximum (w), shift (Δ). The fit was optimized by a least squares formula between that of the original intensity values and the fit formula. Initial guess parameters were defined as the difference between the maximum and minimum intensity value of a peak (A), the mid-point of the peak (x_0), a value of two for the full width at half maximum, and the minimum intensity value as the shift. The value of -10 is a factor (2k in Eq. [1]) dictating steepness which was set to optimize results.

$$H(x) \approx \frac{1}{1 + e^{-2kx}} \quad [1]$$

$$g(x) = A\left[\left\{\frac{1}{1 + e^{-10\left((x-x_0)+\frac{1}{2}w\right)}}\right\} - \left\{\frac{1}{1 + e^{-10\left((x-x_0)-\frac{1}{2}w\right)}}\right\}\right] + \Delta \quad [2]$$

Equation [2] was used to obtain the exact full widths (w) at half maximum of the peaks and, by extrapolation, the widths of the lows. The strain, $\varepsilon(t)$, along the stress fibre was thus determined relative to the zero time point using the following formula (Eq. [3]). It can be seen that, should there be a negative strain value, this indicates compression of a stress fibre segment, while a positive strain value indicates expansion.

$$\varepsilon(t) = \frac{w(t) - w_0}{w(t)} \quad [3]$$

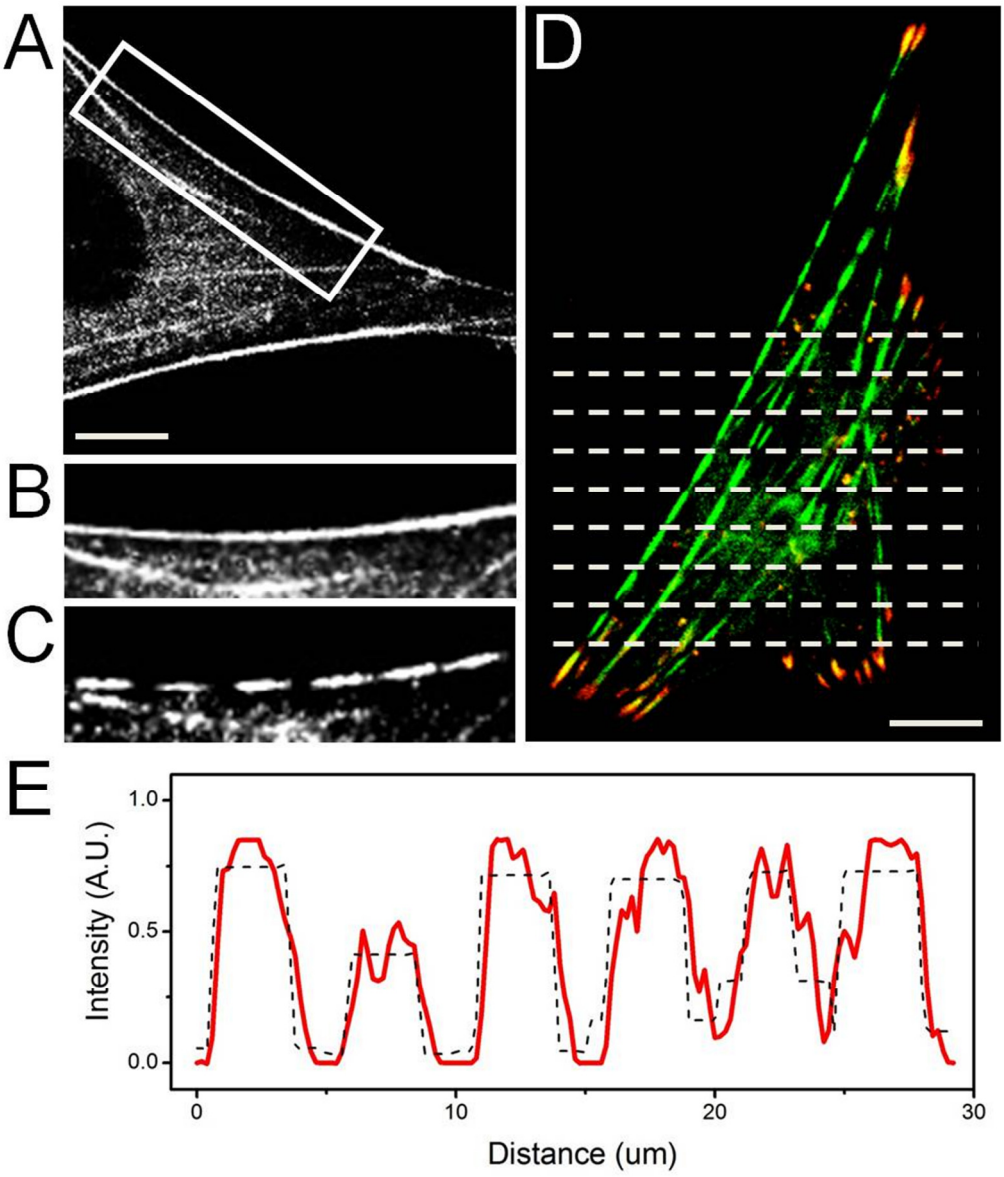

Figure 5.2: Photobleaching of Stress Fibres. An NIH3T3 cell expressing actin-EGFP (**A**; scale bar 15µm) is shown with its stress fibres before (**B**) and after (**C**) photobleaching, resulting in a regular pattern of dark and bright areas. A particular cell expressing both actin-EGFP and zyxin-mRFP was selected to demonstrate the regular pattern of bleaching that was applied to the cell (**D**; scale bar 15µm). The areas to be photobleached, known as regions of interest (ROI), were defined: 1µm in width, spaced at a distance of 5µm (dashed lines). The dashed lines are intentionally left off in the upper region of the cell to demonstrate the resulting bleaching of the GFP contained in stress fibres (note: there has been no physical alteration to the underlying stress fibre). Intensity profiles were created along the length of each stress fibre (**E**, red line). We developed a simple script (described in the text, Appendix A) to analyze this intensity pattern which fit the data to a series of summed Heaviside functions (dashed black line). This script was very successful in fitting the peaks, outputting the width in each case so that strain dynamics could be investigated; anomalies were removed by visual inspection.

This script was ~95% successful in determining the widths of peaks in the data, though in some cases, due to noise in the data, particular peaks were not successfully fit to the curve. In all cases, a plot of the curve of fit and the underlying data was outputed and visibly inspected for anomalies in the fit and for unsuccessful peak fit. Each of these values was removed from the analysis. Additionally, the initial and final peaks were not included in the strain values as the intensity profile began halfway through the peak and the width determined is not an accurate value.

To ensure that any changes in width that are measured is due to local expansion and contraction and not recovery after photobleaching (as in FRAP, see section 2.2.2) or a delayed bleaching effect due to the laser during confocal imaging, the fluorescence intensity of 10 individual photobleached and unbleached areas, as well as their averages, was plotted as a function of time (Figure 5.3A). These points were selected over segments of stress fibres that had been photobleached or remained unbleached in a particular cell, adjusting for any movement that may have occurred. There is no clear downward slope in the average intensity of unbleached areas which would indicate bleaching, nor an upward slope in the average intensity of bleached regions which would indicate FRAP. This was confirmed by performing a T-Test on the initial and final intensity values for both bleached and non-bleached areas; there was no significant difference in intensity in either case (p value > 0.1 for bleached areas and 0.3 for non-bleached areas). The lack of recovery following photobleaching indicates that new actin-EGFP monomers which are fluorescing are not incorporated into the stress fibres at a significant level over the time course of our experiment.

These results are consistent with values of actin turnover found in the literature; most recently Campbell *et al.* (Campbell and Knight 2007) demonstrate only 30% recovery within 240 seconds. Other experiments have reported even slower rates of recovery within stress fibres, with a half-time recovery of about 10 minutes, and full recovery occurring after 30-35 minutes, which is long compared to the length of our experiment (Kreis, Geiger et al. 1982; McGrath, Hartwig et al. 1998; McGrath, Tardy et al. 1998). The quick recovery that is observed in these earlier experiments (Kreis, Geiger et al. 1982) is largely attributed to diffusion of G-actin within the inter-fibre space, as the region upon which FRAP is

performed is not localized enough to specify only stress fibres. As we measured only the intensity recovery over actin stress fibres, it is logical to assume that we would not observe this quick, diffusion based recovery. Longer term recovery has been attributed to new fluorescent G-actin monomers incorporating into the stress fibres, which is generally accepted to be much slower than in single filaments and the inter-fibre space (Kreis, Geiger et al. 1982; McGrath, Tardy et al. 1998; Campbell and Knight 2007).

5.2.2 Strain Dynamics Analysis

Our results show a highly variable local strain dynamic over time in all actin stress fibres. Values of strain were highly heterogeneous in both magnitude and sign along all fibres as well as throughout the cell. Additionally, zones which appeared to be experiencing negative strain could easily switch to positive strain within a minute or two, indicating the variability in time as well. These dynamics were observed for cells under an applied 20nN force (Figure 5.4) and for control cells under 0nN force. Figure 5.4 demonstrates a colour map of local strain values over the course of four minutes (time quoted is relative to the point of force application); the scale of negative to positive strain varies from blue to red with a value of zero strain focusing near green.

Due to the highly dynamic nature of the strain, it was difficult to compare the potential differences that may exist in cells experiencing 0nN and 20nN force. We hypothesized that, instead of an absolute change in local strain values with the application of force, the variability would increase with an application of force. In order to compare individual fibres of differing lengths, the strain values along each fibre were normalized to a scale from -1 to 1. The average local strain was then determined over the course of each minute of experimentation for cells under 0nN and 20nN force (Figure 5.5A) and for the entire time course of the experiment (240sec; Figure 5.5B). In each case, it was obvious that the average strain fluctuated around a mean of zero, but that the standard deviation (σ) or variance (σ^2) was much higher for cells under 20nN force than at 0nN force, and this was apparent within the first minute of force application. This is summarized in Figure 5.5B; the standard deviation from the mean is plotted as a red line for both 0nN cells and 20nN cells.

There is a clear ~50% increase in variance with the application of force: σ =0.15 for 0nN and σ =0.22 for 20nN.

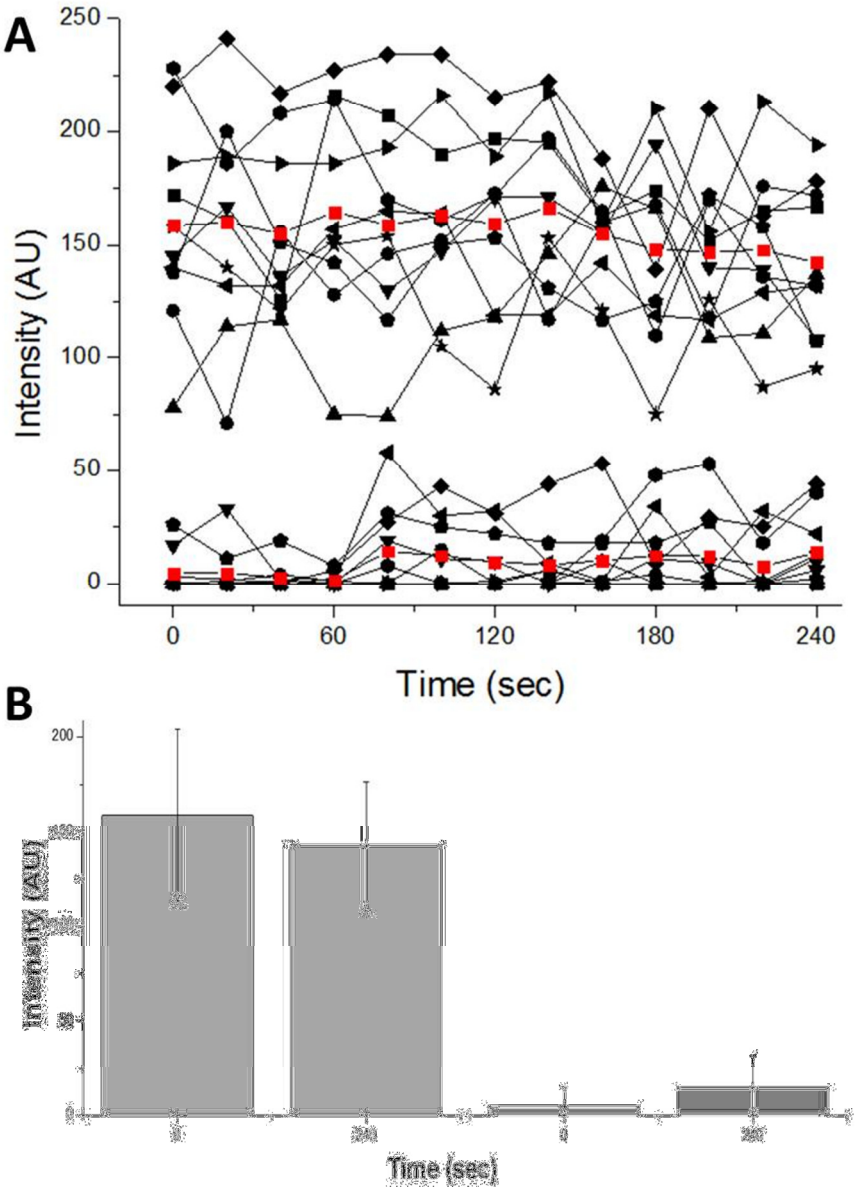

Figure 5.3: Fluorescence intensity over time for photobleached and unbleached areas of actin stress fibres. (A) The intensity of 10 individual points selected over bleached (lower region) and unbleached (upper region) segments of stress fibres in a particular cell are plotted over time. Superimposed is a plot of the average intensity of these 10 points in red for each case. There is no significant trend of either recovery after photobleaching or bleaching in the bright segments. Confirming this, in (**B**), the average intensity (± S.D.) for 0sec and 240sec is plotted for both non-bleached (light grey, left) and bleached regions (dark grey, right). There is no significant difference in intensity values at the beginning and ending of the experiment (p value > 0.3 and 0.1 respectively).

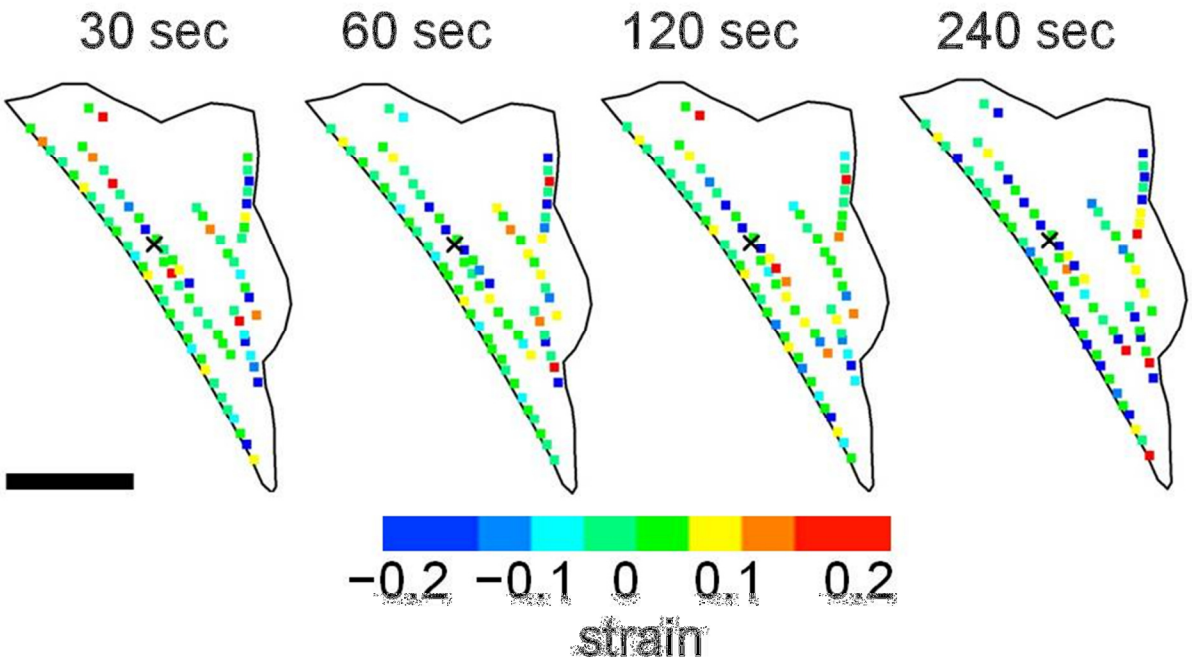

Figure 5.4: Local strain dynamics for a 3T3 fibroblast cell over time under a locally applied force. The strain along actin stress fibres of a particular cell transfected for actin-EGFP was determined as described. A colour-based scale of strain values from -0.2 (blue) to 0.2 (red) demonstrates the dynamics of strain within a cell submitted to 20nN force over the course of four minutes. It is clear that the strain is heterogeneous both in magnitude and sign along individual stress fibres as well as throughout the cell, and changes with time. This was also observed for control cells under 0nN force (not shown). The X marks the location of the AFM tip during force application; scale bar 20µm.

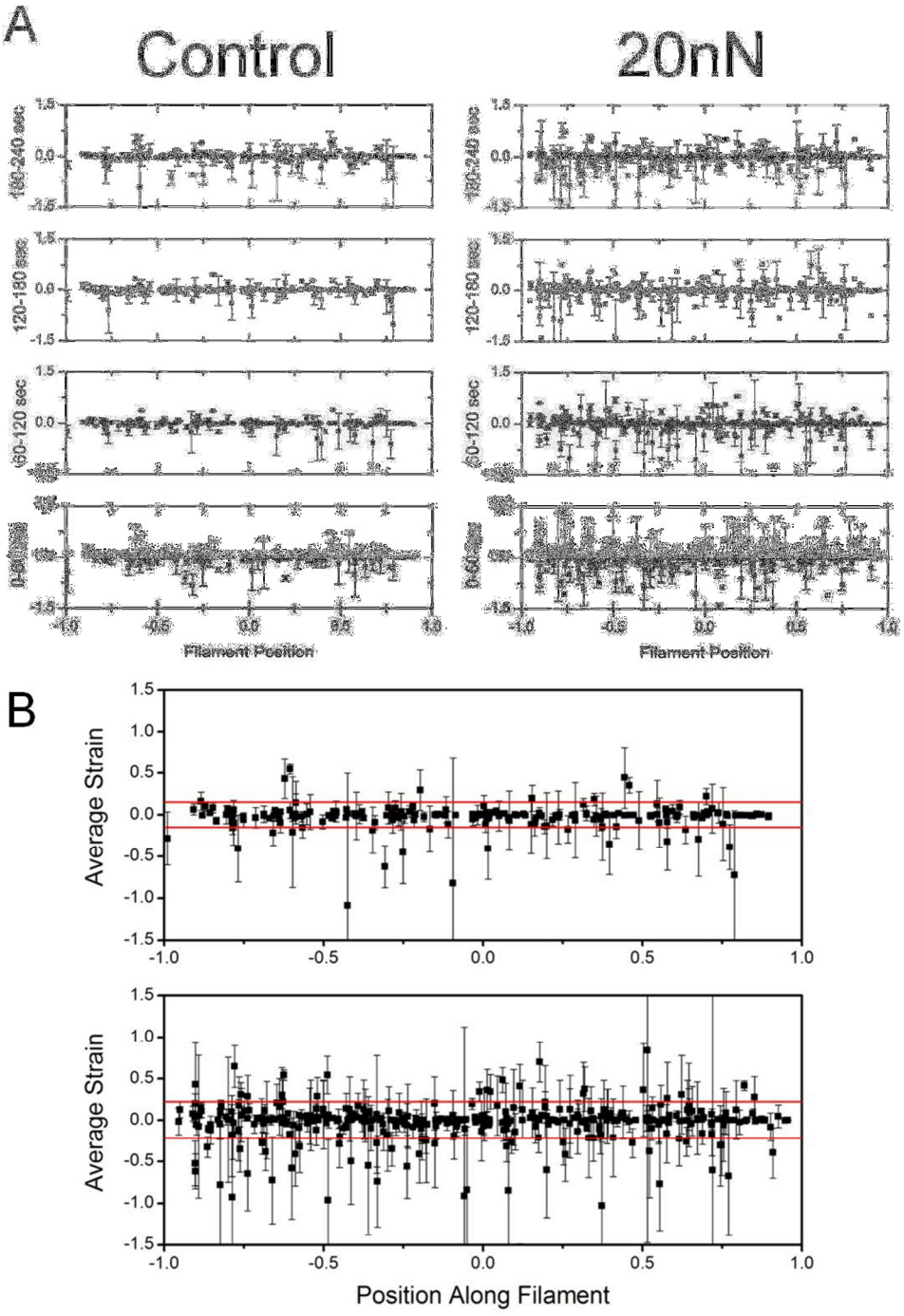

Figure 5.5: Average strain values along normalized actin stress fibres in response to a locally applied force. The strain values of each stress fibre was normalized for position along the fibre and the average strain calculated for each minute of force application at 0nN and 20nN (**A**). Though for both 0nN and 20nN the mean strain average is approximately zero, it can be seen that there is significantly more variance in the average strain values at 20nN for each time interval investigated, and this increase in variance is apparent within the first minute. This is summarized in (**B**) with the average strain values from 0-240sec. The standard deviation from the mean is plotted for both 0nN (top; σ =0.15) and 20nN (bottom; σ =0.22) in red. There is a ~50% increase in the standard deviation for fibres in cells experiencing 20nN force. Individual points are ± standard deviation; n= 8-12.

5.3 Increased Actomysoin Contractility in Response to Locally Applied Force

In a unique study by Peterson *et al.* (Peterson, Rajfur et al. 2004), contraction and expansion along actin stress fibres was measured following the drastic up-regulation of actomyosin contractility by the addition of the drug calyculin A. They demonstrate highly inhomogeneous stretching and compression along stress fibres, which are generally consistent with our results. Their results indicate that contraction is especially apparent along the periphery of the cell and expansion in the middle following treatment with calyculin A; in contrast, we have shown an inhomogeneity in contraction and expansion due to normal fluctuations and an external mechanical stimulus.

As discussed in Chapter 1, actin stress fibres are a highly complex structure containing not only actin, but also large quantities of the actin-binding proteins myosin II, α-actinin, and filamin. The F-actin filaments contained within a stress fibre, rather than spanning the length of the cell, are collected in short bundles (1-2μm) which are linked together end-to-end by α-actinin. In between F-actin filaments are myosin II proteins which are bound to the actin filaments on either end. Myosin II, which is an ATP driven motor protein, 'walks' along F-actin filaments towards their plus-end generating a contractile force. The biochemical pathway which regulates actin stress fibres, myosin kinetics and the creation of the contractile force is known as the Rho pathway (Figure 5.6). This pathway has been well characterized (reviewed in (Fukata, Amano et al. 2001) and there are numerous drugs which have been shown to affect it.

It is tempting to estimate a value for the force that is being transmitted along the actin stress fibre in order to generate this level of strain (0.15 to 0.22). From a straightforward stress/strain (ε) relationship, the force (F) can be estimated from the following equation, where A is the area of applied stress, and E is Young's Modulus.

$$F = A \cdot E \cdot \varepsilon \quad [4]$$

Consider a case where an external force is applied on a single stress fibre, producing a strain in the range of σ = 0.15-0.22. The Young's Modulus and diameter of actin stress fibres have been estimated, to be approximately ~300kPa and ~250nm respectively (Deguchi, Ohashi et

al. 2005). This estimation indicates a required force of 2-3nN along the actin stress fibre is necessary to generate the strain values we have measured. However, since the force applied by the AFM is not being applied directly to the stress fibres themselves, this suggests that the force causing these highly inhomogeneous local strain dynamics indicate a local generation of force, which we suggest is due to actomyosin contractility, indicating that myosin are capable of generating a 2-3nN force. As a single myosin protein has been shown to produce a contractile force on the order of ~2pN (Veigel, Molloy et al. 2003), and there are many copies of myosin within a single stress fibre, this is not an unreasonable assumption. Further, contractile forces along stress fibres have been measured in the range of 0.5-4nN previously (Deguchi, Ohashi et al. 2005; Thoresen, Lenz et al. 2011). The estimations of Young's Modulus used here, as well as the diameter, were taken from measurements of a reconstituted actin system or single isolated stress fibres (not found within a cell) (Deguchi, Ohashi et al. 2005; Thoresen, Lenz et al. 2011). In a living cell however, the extensive cross-linking which exists between stress fibres with actin-binding proteins, other members of the cytoskeleton, and focal adhesion complexes (Even-Ram, Doyle et al. 2007) could drastically change the value of Young's Modulus; indeed estimates have been made of values in upwards of 1GPa (Kojima, Ishijima et al. 1994). If such is the case, in order to produce the strain values measured, the forces generated would have to be on the order of tens or even hundreds of nanonewtons. This indicates the importance of taking cross-linking into consideration.

We suggest that the strain dynamics observed are due to an increase in local actomyosin contractility within stress fibres in response to a mechanical stimulus, rather than a more global response along the length of the entire stress fibre. A study of the Rho pathway, as is summarized in the upper part of Figure 5.6, indicates that this is a plausible argument. In Figure 5.6, the application of force to a cell stimulates the intake of Ca^{2+} via stress activated ion channels (Formigli, Meacci et al. 2007). This results in a calmodulin dependent up-regulation of Myosin Light Chain Kinase (MLCK) which, along with Rho Kinase, constitutively activates the light chain of myosin II via phosphorylation, leading to increased actomyosin contractility (Fukata, Amano et al. 2001). This is effectively the same mechanism as would be activated by treatment with Calyculin A, as done by Peterson *et al.*, as calyculin A inhibits Myosin Light Chain Phosphatase (MLCPase) (Hosoya, Mitsui et al.

1993), which will prevent the dephosphorylation of myosin light chain, forcing myosin II to remain in an active state and resulting in a high increase of stress fibre formation and contraction.

We could predict that, should contraction occur in a highly local manner, a negative value of strain in a photobleached segment should be adjacent to a segment which experiences a positive value of strain, and vice versa (Figure 5.6). However, we did not observe any regular pattern of contraction and expansion along any of the stress fibres analyzed, either at 0nN or 20nN force. Given the highly cross-linked nature of stress fibres with other components of the cytoskeleton and FAs (Even-Ram, Doyle et al. 2007), it is likely that there will be significant variation in the local value of Young's Modulus along the length of actin stress fibres, on the scale of μm-nm. These local mechanical variations are likely to cause regions where strain is far more likely to occur (less force is necessary), resulting in an inhomogeneous strain distribution as we have observed rather than a regular pattern of alternating contraction and expansion. Importantly, the external force which is applied by the AFM is not being directly applied to these stress fibres to cause these observed strain dynamics, rather the force is internally generated by actomyosin contractility. Further, while there exists strain variations even in control cells, a ~50% increase in variance is observed with the application of 20nN force; to the best of our knowledge this is the first direct demonstration of increased actomyosin contractility in response to a locally applied force.

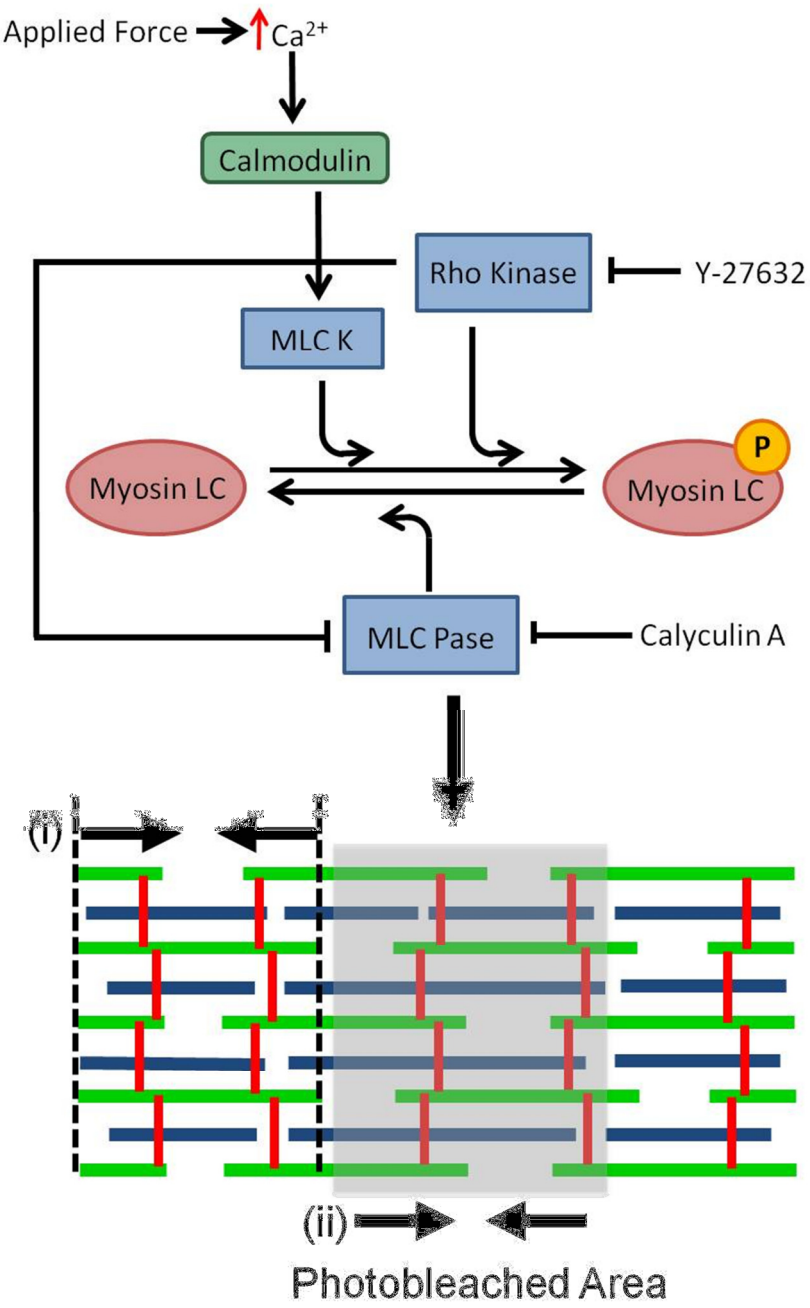

Figure 5.6: Possible mechanotransduction pathway that results in the observed strain dynamics. The rho pathway (shown in the top panel) has been well characterized and is involved directly in the regulation of actomyosin contractility. We suggest that an externally applied force results in an increase in Ca^{2+} ions, which induce a calmodulin dependant activation of myosin light chain kinase (MLCK). This kinase, as well as rho kinase (ROCK), phosphorylate the light chain of myosin II (Myosin LC) activating it and causing increased contraction and stress fibre formation. This would have a similar effect as treatment with calyculin A, which is an inhibitor of myosin light chain phosphatase (MLCPase); this effectively blocks the inactivation of myosin II, constitutively activating contraction throughout the cell. These cascades will lead to possible contraction dynamics within the unbleached (i) and bleached (ii) segments of stress fibres (schematic in lower panel). Due to the highly cross-linked nature of the cytoskeleton, contraction in one segment will not necessarily lead to expansion in the adjacent segment or vice versa.

5.4 References

Campbell, J. J. and M. M. Knight (2007). "An improved confocal FRAP technique for the measurement of long-term actin dynamics in individual stress fibers." Microsc Res Tech **70**(12): 1034-40.

Colombelli, J., A. Besser, et al. (2009). "Mechanosensing in actin stress fibers revealed by a close correlation between force and protein localization." J Cell Sci **122**(Pt 10): 1665-79.

Deguchi, S., T. Ohashi, et al. (2005). "Evaluation of tension in actin bundle of endothelial cells based on preexisting strain and tensile properties measurements." Mol Cell Biomech **2**(3): 125-33.

Even-Ram, S., A. D. Doyle, et al. (2007). "Myosin IIA regulates cell motility and actomyosin-microtubule crosstalk." Nat Cell Biol **9**(3): 299-309.

Formigli, L., E. Meacci, et al. (2007). "Cytoskeleton/stretch-activated ion channel interaction regulates myogenic differentiation of skeletal myoblasts." J Cell Physiol **211**(2): 296-306.

Fukata, Y., M. Amano, et al. (2001). "Rho-Rho-kinase pathway in smooth muscle contraction and cytoskeletal reorganization of non-muscle cells." Trends Pharmacol Sci **22**(1): 32-9.

Hosoya, N., M. Mitsui, et al. (1993). "Changes in the cytoskeletal structure of cultured smooth muscle cells induced by calyculin-A." J Cell Sci **105 (Pt 4)**: 883-90.

Kojima, H., A. Ishijima, et al. (1994). "Direct measurement of stiffness of single actin filaments with and without tropomyosin by in vitro nanomanipulation." Proc Natl Acad Sci U S A **91**(26): 12962-6.

Kreis, T. E., B. Geiger, et al. (1982). "Mobility of microinjected rhodamine actin within living chicken gizzard cells determined by fluorescence photobleaching recovery." Cell **29**(3): 835-45.

Lele, T. P., J. Pendse, et al. (2006). "Mechanical forces alter zyxin unbinding kinetics within focal adhesions of living cells." J Cell Physiol **207**(1): 187-94.

McGrath, J. L., J. H. Hartwig, et al. (1998). "Measuring actin dynamics in endothelial cells." Microsc Res Tech **43**(5): 385-94.

McGrath, J. L., Y. Tardy, et al. (1998). "Simultaneous measurements of actin filament turnover, filament fraction, and monomer diffusion in endothelial cells." Biophys J **75**(4): 2070-8.

Peterson, L. J., Z. Rajfur, et al. (2004). "Simultaneous stretching and contraction of stress fibers in vivo." Mol Biol Cell **15**(7): 3497-508.

Rottner, K., M. Krause, et al. (2001). "Zyxin is not colocalized with vasodilator-stimulated phosphoprotein (VASP) at lamellipodial tips and exhibits different dynamics to vinculin, paxillin, and VASP in focal adhesions." Mol Biol Cell **12**(10): 3103-13.

Thoresen, T., M. Lenz, et al. (2011). "Reconstitution of contractile actomyosin bundles." Biophys J **100**(11): 2698-705.

Veigel, C., J. E. Molloy, et al. (2003). "Load-dependent kinetics of force production by smooth muscle myosin measured with optical tweezers." Nat Cell Biol **5**(11): 980-6.

Chapter Six:

Conclusions

Taken together, our results suggest two distinct responses of the fibroblast cells used in our study to nanoscale forces applied to the nucleus. A short term response (20-60 seconds) in which stress fibres displace within 20 seconds directly in response to force and a long term response (60-240 seconds) in which force initiates FA remodelling and movement of stress fibres far from the point of contact at cell edges. Moreover stress fibre deformation does not occur in an isotropic fashion, but occurs in localized areas or results in the retraction of some stress fibres. The most immediate response of a cell to a mechanical stimulus is a complex structural deformation which requires the integration of several elements of the cytoskeleton.

Firstly, we have shown that this response is dependent on the presence of microtubules within cells. Although cells treated with nocodazole have had their cortical elasticity reduced by ~50% and are therefore theoretically more deformable, no isotropic deformation was observed. However, cells which were chosen for experimentation still possessed an intact actin stress fibre network and were of the same approximate height as non-treated cells; as well, the indentation depths of the AFM tip did not increase significantly for nocodazole treated cells. Despite these similarities, cells lacking an intact microtubule network do not reveal any significant stress fibre displacement as in non-treated cells. However, upon loss of the contractile actin network following treatment with a rho kinase inhibitor, the cell responds very much like an isotropic balloon to an applied point force.

In most cells, some stress fibres were observed to retract in response to an applied load. It should be noted that this only occurs in a few stress fibres in select locations and does not result in a complete retraction of the cell on all edges. The cell in large part remains firmly attached to the substrate via intact FA sites, even for retracting stress fibres. This was further demonstrated by the correlated movements of FA sites with retracting or displacing stress fibres. Our results of experiments with nocodazole lead us to suggest that a force dependant signal is transmitted by the microtubule network to some FA sites, resulting in the retraction of actin fibres, possibly as a response to the sudden increased load localized over the nucleus. Clearly, the structural and mechanical response of a cell to a locally applied force is highly complex but requires the integration of responses of many elements of the cytoarchitecture, including but not limited to, microtubules, FA sites and actin stress fibres.

In addition to lateral displacement of stress fibres and FA remodelling, we have also characterized the apparent strain dynamics that take place along stress fibres with and without an applied force of 20nN. We show that these strain dynamics are heterogeneous along the stress fibre and suggest that the local variance in strain values in magnitude and sign over time is caused by the internal movement of F-actin filaments by myosin. Importantly, the activity of localized myosin mediated contraction increases in response to a mechanical stimulus by as much as 50%. This suggests that we have directly visualized the activity of actomyosin contraction *in vitro* in actin stress fibres of non-muscle cells, and that this contraction is increased with an applied external force. The observed retraction at cell edges in previous experiments is likely caused by this same mechanism of increased actomyosin contractility, which we have shown to be microtubule dependent. Indeed, it has been demonstrated previously that there exists a relationship between the microtubule network and myosin II, especially localized near FAs (Even-Ram, Doyle et al. 2007), which adds further credence to our argument. We also suggest that the presence of cross-linking within the cytoskeleton plays an important role in causing the heterogeneity of the strain results.

Future work will include investigations into further quantifying and elucidating the contribution of myosin II in causing these increased strain dynamics. Experiments are planned in which cells doubly transfected with myosin-GFP and actin-mRFP are examined at higher spatial and temporal resolution; this will also allow us to investigate the possible co-localization and dynamics of actin and myosin in response to force applied by an AFM. A follow-up study involving the use of drugs such as nocodazole and an inhibitor of myosin II is also planned. We hope to develop an intensive model of the cell which is consistent with the strain dynamics observed in this thesis and future work.

The results presented in this thesis are highly intriguing. We have demonstrated for the first time (to the best of our knowledge) that there is increased actomyosin contractility in response to an applied force, which we have linked to the Rho pathway, and suggest that it is also dependent on the microtubule network, especially considering the putative role of cross-linking in strain dynamics of actin stress fibres. It is clear that further work must be done, especially focusing on developing similar assays with increased temporal and spatial

resolution. This will allow us to investigate the origin of heterogeneous strain dynamics and their spatial relationship with actin-cytoskeleton cross-linking. Further, we have quantified the amount of stress fibre displacement in response to local nanonewton forces, and, most importantly, demonstrate that this response is not isotropic in nature, but rather results in a complex and localized response that is dependent on an intact microtubule network, and this response occurs within 20 seconds of mechanical stimulus.

Mechanical stimuli are crucial factors that have been shown to be highly involved in regulating cell biology, however the short term structural response of a cell to mechanical deformation remains relatively poorly understood. In this thesis, we have shown that fibroblast cells possess several clear force dependent responses to mechanical stimulation, resulting in highly localized displacement of and strain dynamics within actin stress fibres. Direct visualization of force-propagation in this study has revealed several critical and complex phenomena that require the integration of the entire cytoskeleton and ultimately govern the long-term downstream response of a cell to mechanical stimuli. This information is highly relevant to the field of cellular biophysics, as a full understanding of the mechanotransduction pathways within cells will lead to better physical models of the cell, and eventually lead to a better understanding of the role mechanical stimuli play in disease, gene regulation, and differentiation of stem cells- fields that lie on the cutting edge of biological research today.

References

Even-Ram, S., A. D. Doyle, et al. (2007). "Myosin IIA regulates cell motility and actomyosin-microtubule crosstalk." Nat Cell Biol **9**(3): 299-309.

Appendix A:

Python Script for Photobleaching Analysis

Composed, with my thanks, by Martin Bertrand

```
################################################################
# Documentation
################################################################

# To run this script in Windows, go to the command prompt in
# the folder where the script is and type:
# python strain_vs_time.py -f file_to_analyze -w window_threshold -s shift
# where file_to_analyze, window_threshold and shift are placeholders
# where you type in appropriate values.

# The script returns two files:
# file_to_analyze.strain_peaks.txt
# file_to_analyze.strain_lows.txt

# You might have to play with window_threshold and shift to get
# the best fit possible. Some of the oddest peaks, i.e. those that
# look like doublets, are not always fitted appropriately. Keep an
# eye open for these. You should always run the script with
# plot_flag=1 for quick visual assessment and to take notes of those
# peaks that are not fitted appropriately. By the way you should be
# able to measure (x,y) coordinates on the plots with the cursor.

################################################################
# Get command line arguments
################################################################
argv = sys.argv[1:]
try:
        opts, args = getopt.getopt(argv,"f:w:s:")
except getopt.GetoptError:
        usage()
        sys.exit(2)

# Defaults (some good starting values)
thresh_window = 25.0
shift = 5.0

for o, val in opts:
        if o == "-f":
                name = val
        if o == "-w":
                # Window length of threshold
                thresh_window = float(val)
        if o == "-s":
                # Threshold shift
                shift = float(val)

############################################################
```

```
# Routines
#################################################################

# Square peak function
#g = lambda x,x0,a,w,shift: a*(1./(1.+np.exp(-10.*(x-x0+(1./2.)*w)))-1./(1.+np.exp(-10.*(x-x0-
(1./2.)*w))))+shift
g = lambda a,x: a[1]*(1./(1.+np.exp(-10.*(x-a[0]+(1./2.)*a[2])))-1./(1.+np.exp(-10.*(x-a[0]-(1./2.)*a[2]))))+a[3]
gerr = lambda a,x,y: g(a,x)-y

# Data Smoothing or running average
def smooth(x, window_len=10, window='hanning'):
    """smooth the data using a window with requested size.

    This method is based on the convolution of a scaled window with the signal.
    The signal is prepared by introducing reflected copies of the signal
    (with the window size) in both ends so that transient parts are minimized
    in the begining and end part of the output signal.

    input:
        x: the input signal
        window_len: the dimension of the smoothing window
        window: the type of window from 'flat', 'hanning', 'hamming', 'bartlett', 'blackman'
            flat window will produce a moving average smoothing.

    output:
        the smoothed signal

    example:

    import numpy as np
    t = np.linspace(-2,2,0.1)
    x = np.sin(t)+np.random.randn(len(t))*0.1
    y = smooth(x)

    see also:

    numpy.hanning, numpy.hamming, numpy.bartlett, numpy.blackman, numpy.convolve
    scipy.signal.lfilter

    TODO: the window parameter could be the window itself if an array instead of a string
    """

    if x.ndim != 1:
        raise ValueError, "smooth only accepts 1 dimension arrays."

    if x.size < window_len:
        raise ValueError, "Input vector needs to be bigger than window size."

    if window_len < 3:
        return x

    if not window in ['flat', 'hanning', 'hamming', 'bartlett', 'blackman']:
        raise ValueError, "Window is one of 'flat', 'hanning', 'hamming', 'bartlett', 'blackman'"

    s=np.r_[2*x[0]-x[window_len:1:-1], x, 2*x[-1]-x[-1:-window_len:-1]]
    #print(len(s))
```

```
    if window == 'flat': #moving average
        w = np.ones(window_len,'d')
    else:
        w = getattr(np, window)(window_len)
    y = np.convolve(w/w.sum(), s, mode='same')
    return y[window_len-1:-window_len+1]

##############################################################
# Main body
##############################################################

# Prepare plot
plot_flag = 1
if plot_flag:
        pl.figure(1)

# Load data file
data = np.loadtxt(name)
npts = data.shape[0]
ncol = data.shape[1]
for j in range(ncol/2):
        x = data[:,2*j]
        intense_org = data[:,2*j+1]

        intense = smooth(intense_org,window_len=10,window='flat')
        thresh = smooth(intense_org,window_len=thresh_window,window='flat')-shift
        thresh[0:5] = 10.0

        if plot_flag:
                pl.plot(x,intense,'-k')
                pl.plot(x,thresh,'-b')
                #pl.plot(x,y,'-b')

        # Build neigborhood array
        cut = np.where(intense < thresh,1,0)
        m = cut[0:-1]*cut[1:]
        z = np.array([0])
        neigh = np.where((np.append(m,z)+np.append(z,m)) > 0,1,0).astype(np.int32)

        # Build list of peaks
        starts = []
        ends = []
        peaks = []
        lows = []
        i = 0
        while i < npts:
                val = neigh[i]
                if val == 0:
                        start = i
                        i += 1
                        while val == 0 and i < npts:
                                val = neigh[i]
                                i += 1
                        if i == npts:
                                end = npts
```

```
                else:
                        end = i
                peaks.append(int((start+end)/2.))
        else:
                start = i
                i += 1
                while val == 1 and i < npts:
                        val = neigh[i]
                        i += 1
                if i == npts:
                        end = npts
                else:
                        end = i
                lows.append(int((start+end)/2.))

npeaks = len(peaks)
nlows = npeaks-1
# Initialize width array
if j == 0:
        width_highs = np.zeros(npeaks)
        width_lows = np.zeros(nlows)
        n0 = npeaks

# Build starts and ends
for i in range(npeaks):
        # For starts
        if i == 0:
                starts.append(0)
        else:
                starts.append(lows[i-1])

        # For ends
        if i == npeaks-1:
                ends.append(npts)
        else:
                ends.append(lows[i])

if npeaks == n0:
        # Fit the peaks
        width_high_j = np.zeros(npeaks)
        mid_high_j = np.zeros(npeaks)
        for i in range(npeaks):
                x_tofit = x[starts[i]:ends[i]]
                y_tofit = intense_org[starts[i]:ends[i]]
                try:
                        baseline = np.min(y_tofit)
                        peakheight = np.max(y_tofit)-baseline
                except:
                        baseline = 0.0
                        peakheight = 100.0
                x0 = x[peaks[i]]
                # Guess values
                p0 = [x0,peakheight,2.,baseline]
                try:
                        #par,cov = optimize.curve_fit(g,x_tofit,y_tofit,p0=p0)
                        par, success = optimize.leastsq(gerr,p0,args=(x_tofit,y_tofit))
```

```
                                        mid_high_j[i] = par[0]
                                        width_high_j[i] = par[2]
                                except:
                                        print "Peak %d did not work" % (i)
                                        width_high_j[i] = 1000.
                                # Plot fit
                                if plot_flag:
                                        pl.figure(1)
                                        #gy = g(x_tofit,par[0],par[1],par[2],par[3])
                                        gy = g(par,x_tofit)
                                        pl.plot(x_tofit,gy,'--r',lw=2.0)
                                print par
                        # Append width_high_j to width_highs
                        width_highs = np.vstack((width_highs,width_high_j))
                        # Build width_low_j
                        width_low_j = ((mid_high_j[1:]-width_high_j[1:]/2.)+(mid_high_j[0:-1]+width_high_j[0:-
1]/2.0))/2.0
                        width_lows = np.vstack((width_lows,width_low_j))

                print "Frame %d analyzed" % (j)
                print x[starts]
                print x[ends[:-1]]
                if plot_flag:
                        pl.show()

# Save data
width_highs = width_highs[1:]
strain_highs = np.array(width_highs)
for i in range(width_highs.shape[0]):
        for j in range(width_highs.shape[1]):
                strain_highs[i,j] = (width_highs[i,j]-width_highs[2,j])/width_highs[i,j]
np.savetxt(name+'.strain_peaks.txt',strain_highs)

width_lows = width_lows[1:]
strain_lows = np.array(width_lows)
for i in range(width_lows.shape[0]):
        for j in range(width_lows.shape[1]):
                strain_lows[i,j] = (width_lows[i,j]-width_lows[2,j])/width_lows[i,j]
np.savetxt(name+'.strain_lows.txt',strain_lows)
```

Appendix B:

Permission to Use JPK Figures

Hi Gerd –

A student of mine is writing her thesis and would like to include a graphic from the JPK manual. Would this be a problem if we cite the source? It's easy enough for her to make it if necessary however.

Cheers, A

Andrew E. Pelling
Canada Research Chair
www.pellinglab.net

Hi Andrew,

Sure, that's no problem! Let me know which graphic is needed and I will try to get it for you.

Cheers
Gerd

Hello,

The figures that I would like to use lie on pages 5 and 6 of the NanoWizard AFM Handbook (v2.2); The ones that depict the different imaging modes of the AFM. I would need to include official documentation in my thesis that I have written permission from JPK to use these figures, though an e-mail should suffice.

Thanks so much for your help!
Louise Guolla
Pelling Lab
